Extension of the SmEdA method by taking into account dissipative materials at medium frequencies

Hadong Hwang

2015ISAL0048

THÈSE DE DOCTORAT

présentée devant
l'Institut National des Sciences Appliquées de Lyon

par
HaDong HWANG

pour obtenir
le GRADE DE DOCTEUR

École doctorale:
Mécanique, énergétique, Génie Civil, Acoustique
Spécialité: Acoustique

Thèse préparée au Laboratoire Vibrations Acoustique

soutenue le 5 juin 2015

EXTENSION DE LA MÉTHODE SmEdA PAR LA PRISE EN COMPTE DES MATÉRIAUX DISSIPATIFS EN MOYENNES FRÉQUENCES

JURY

Jonas BRUNSKOG (Professeur)	ACT, DTU	Rapporteur
Morvan OUISSE (Professeur)	FEMTO-ST, ENSMM	Rapporteur
Jean-Louis GUYADER (Professeur)	LVA, INSA de Lyon	Examinateur
Hervé RIOU (Professeur)	LMT, ENS Cachan	Examinateur
Kerem EGE (Maître de Conférences)	LVA, INSA de Lyon	Directeur de Thèse
Laurent MAXIT (Maître de Conférences, HDR)	LVA, INSA de Lyon	Directeur de Thèse

Année 2015

INSA Direction de la Recherche - Ecoles Doctorales – Quinquennal 2011-2015

SIGLE	ECOLE DOCTORALE	NOM ET COORDONNEES DU RESPONSABLE
CHIMIE	**CHIMIE DE LYON** **http://www.edchimie-lyon.fr** Insa : R. GOURDON	M. Jean Marc LANCELIN Université de Lyon – Collège Doctoral Bât ESCPE 43 bd du 11 novembre 1918 69622 VILLEURBANNE Cedex Tél : 04.72.43 13 95 directeur@edchimie-lyon.fr
E.E.A.	**ELECTRONIQUE, ELECTROTECHNIQUE, AUTOMATIQUE** **http://edeea.ec-lyon.fr** Secrétariat : M.C. HAVGOUDOUKIAN eea@ec-lyon.fr	M. Gérard SCORLETTI Ecole Centrale de Lyon 36 avenue Guy de Collongue 69134 ECULLY Tél : 04.72.18 60 97 Fax : 04 78 43 37 17 Gerard.scorletti@ec-lyon.fr
E2M2	**EVOLUTION, ECOSYSTEME, MICROBIOLOGIE, MODELISATION** **http://e2m2.universite-lyon.fr** Insa : H. CHARLES	Mme Gudrun BORNETTE CNRS UMR 5023 LEHNA Université Claude Bernard Lyon 1 Bât Forel 43 bd du 11 novembre 1918 69622 VILLEURBANNE Cédex Tél : 04.72.43.12.94 e2m2@biomserv.univ-lyon1.fr
EDISS	**INTERDISCIPLINAIRE SCIENCES-SANTE** **http://ww2.ibcp.fr/ediss** Sec : Safia AIT CHALAL Insa : M. LAGARDE	M. Didier REVEL Hôpital Louis Pradel Bâtiment Central 28 Avenue Doyen Lépine 69677 BRON Tél : 04.72.68 49 09 Fax :04 72 35 49 16 Didier.revel@creatis.uni-lyon1.fr
INFOMATHS	**INFORMATIQUE ET MATHEMATIQUES** http://infomaths.univ-lyon1.fr	M. Johannes KELLENDONK Université Claude Bernard Lyon 1 INFOMATHS Bâtiment Braconnier 43 bd du 11 novembre 1918 69622 VILLEURBANNE Cedex Tél : 04.72. 44.82.94 Fax 04 72 43 16 87 infomaths@univ-lyon1.fr
Matériaux	**MATERIAUX DE LYON** Secrétariat : M. LABOUNE PM : 71.70 –Fax : 87.12 Bat. Saint Exupéry Ed.materiaux@insa-lyon.fr	M. Jean-Yves BUFFIERE INSA de Lyon MATEIS Bâtiment Saint Exupéry 7 avenue Jean Capelle 69621 VILLEURBANNE Cédex Tél : 04.72.43 83 18 Fax 04 72 43 85 28 Jean-yves.buffiere@insa-lyon.fr
MEGA	**MECANIQUE, ENERGETIQUE, GENIE CIVIL, ACOUSTIQUE** Secrétariat : M. LABOUNE PM : 71.70 –Fax : 87.12 Bat. Saint Exupéry mega@insa-lyon.fr	M. Philippe BOISSE INSA de Lyon Laboratoire LAMCOS Bâtiment Jacquard 25 bis avenue Jean Capelle 69621 VILLEURBANNE Cedex Tél :04.72.43.71.70 Fax : 04 72 43 72 37 Philippe.boisse@insa-lyon.fr
ScSo	**ScSo*** M. OBADIA Lionel Sec : Viviane POLSINELLI Insa : J.Y. TOUSSAINT	M. OBADIA Lionel Université Lyon 2 86 rue Pasteur 69365 LYON Cedex 07 Tél : 04.78.69.72.76 Fax : 04.37.28.04.48 Lionel.Obadia@univ-lyon2.fr

*ScSo : Histoire, Geographie, Aménagement, Urbanisme, Archéologie, Science politique, Sociologie, Anthropologie

Résumé

Le projet CLIC (City Lightweight Innovative Cab) dans lequel s'inscrit cette thèse de doctorat vise à développer une cabine de camion allégée sans dégrader les performances vibratoires et acoustiques. Pour cela il est nécessaire d'établir dans un premier temps un modèle de prédiction vibroacoustique du système couplé structure/espace intérieur incluant l'influence des matériaux dissipatifs (amortissement ou absorption) dans le domaine des moyennes fréquences. C'est l'objectif de cette thèse. Les méthodes basées sur les éléments finis et les approches statistiques les plus couramment utilisées étant peu adaptées pour ce domaine de fréquence (coût de calcul trop important, méthodes peu flexibles), nous utiliserons le formalisme de la méthode SmEdA (Statistical modal Energy distribution Analysis) qui étend la gamme de fréquences de la SEA (Statistical Energy Analysis) au domaine des moyennes fréquences en levant l'hypothèse d'équipartition de l'énergie modale. L'objectif principal de cette thèse de doctorat est dès lors, d'étendre cette méthode à la prise en compte de l'effet d'amortissement induit par des matériaux dissipatifs. La méthodologie se divise en trois étapes:

1. Les modèles équivalents des matériaux dissipatifs sont établis: (1) un modèle de plaque équivalent pour décrire la plaque amortie par un ou plusieurs patch(s) viscoélastique(s) et (2) un modèle de fluide équivalent pour décrire un matériau poreux agissant dans la cavité.

2. Chaque sous-système amorti est modélisé par éléments finis. Les méthodes MSE (Modal Strain Energy) et MSKE (Modal Strain Kinetic Energy) sont ensuite utilisées pour estimer les facteurs de perte modaux de chaque sous-système.

3. Le calcul SmEdA est effectué sur le système couplé en prenant en compte les facteurs de pertes modaux de chaque sous-système estimés dans la deuxième étape. Le point d'excitation est appliquée à la plaque, en supposant la force stationnaire et large bande.

Afin de valider la méthodologie proposée un cas semi-complexe composé d'une plaque rectangulaire couplée à une cavité parallélépipédique est considéré. Ce système fluide-structure simplifié peut être util-

isé pour étudier l'interaction vibroacoustique entre la structure de la cabine et l'intérieur de l'habitacle (couplages plancher-cabine ou panneau arrière-cabine)

Deux cas d'amortissement sont étudiés pour le système semi-complexe plaque-cavité: (1) un cas où la plaque est amortie avec un (ou plusieurs) patch(s) viscoélastique(s) et (2) un cas où un matériau poreux est placé dans la cavité. Le problème vibroacoustique est pour chaque cas modélisé suivant les trois étapes proposées et analyses dans le formalisme de la méthode SmEdA. Les résultats sont ensuite comparés au cas de référence (sans matériau dissipatif).

La dernière partie de la thèse porte sur la validation expérimentale pour chaque cas test de la méthodologie numérique proposée. Une excitation stationnaire localisée sur la plaque est considérée, et les énergies de chaque sous-système sont mesurées simultanément. La mobilité d'éntrée, la puissance injectée et les énergies des sous-systèmes sont comparées aux prédictions numériques. Enfin les facteurs de pertes modaux des sous-systèmes estimés par les méthodes MSE et MSKE sont comparés aux résultats expérimentaux obtenus par la méthode d'analyse modale à haute résolution (méthode ESPRIT).

Mots clés: analyse vibroacoustique, méthode énergétique, moyennes fréquences, couplage fluide-structure, modèle de plaque équivalent, modèle de fluide équivalent, facteur de perte modal, mesure de l'énergie des sous-système, puissance injectée.

Abstract

The project CLIC (City Lightweight Innovative Cab) aims to develop a lighter-weighted truck that maintains NVH performances of the initial design. This PhD research is then to establish a vibroacoustic prediction model of a complex structure-bounded fluid system (cabin structure coupled to cabin space) including dissipative treatments (damping or absorbing materials) for the mid-frequency domain. Since most commonly used element based and statistical methods are not suitable for this frequency domain, a proper prediction tool, which should be flexible in modeling capabilities and feasible in computational cost, must be implemented. The SmEdA (Statistical modal Energy distribution Analysis) method is considered in this thesis to comply with these requirements. This method extends the frequency range of the classical SEA (Statistical Energy Analysis) to the mid-frequency domain as it circumvents the modal energy equipartition assumption. The main objective of this research is to extend this method for taking account of the damping effect induced by dissipative materials. Development and validation of the methodology are carried out.

1. Dissipative materials are represented by simplified equivalent models: (1) the equivalent single layer model for describing the plate covered with a viscoelastic layer and (2) the equivalent fluid model for describing a porous material into the cavity.

2. Each subsystem including the equivalent models of the dissipative materials is modeled with FEM (Finite Element Model). The FE matrices including the energy dissipation are then computed. The MSE (Modal Strain Energy) and MSKE (Modal Strain Kinetic Energy) methods are used to estimate the modal damping loss factor of each subsystem mode.

3. The SmEdA calculation is performed on a whole system considering the modal damping loss factors estimated in the second step for each subsystem. The power is injected into the plate at a localized point by the stationary white noise force and subsequently, the SmEdA parameters are computed.

To validate the proposed methodology, laboratory test cases of the structure-fluid problem composed of a rectangular plate coupled to a parallelepipedic cavity are considered. Such system simplifies the truck

cabin and can be used to study the vibroacoustic interaction between structure and fluid as floor-cabin space and rear surface-cabin space interactions are of interest. Within the simplified setup, dissipative treatment configurations can be easily manipulated and precise physical parameters are manageable.

Two damped test cases of the plate-cavity system are studied: (1) a system with a viscoelastic damping pad on the plate and (2) a system with a composite fibre in the cavity. The damped test cases are modeled following the three steps and are analyzed in the framework of SmEdA. The results are then compared to the original case with no damping treatment.

The last part of the thesis presents an experimental validation of the numerical computation results on each test case. As a localized stationary force is exerted on the plate, subsystem energies are simultaneously measured. Measured quantities such as input mobility, injected power and subsystem energies are compared to the numerical predictions. The modal damping loss factors of the damped subsystems estimated with MSE and MSKE methods are compared to the experimental results estimated by a high-resolution modal analysis method (ESPRIT method).

Keywords: vibroacoustic analysis, energy method, mid-frequency, structure-fluid system, equivalent single layer model, equivalent fluid model, modal damping loss factor, modal strain and kinetic energy, measurement of subsystem energies, injected power.

Contents

Introduction

City Lightweight Innovative Cab Project

More than 10 % of urban noise is known to stem from the ground freight. Heavy vehicles transporting commercial goods are a significant noise source creating public nuisance in urban areas. Drivers of such vehicles regularly spend several hours a day driving on the road. Inevitably, they are exposed to a high level of broadband noise for a long duration which could lead to the detriment of hearing. There are many other safety and health issues such as crash accidents, back pains, stress, etc. Since passenger comfort and saftey have increasiingly become an important element for all types of vehicles, manufacturers are required to address these issues. In order to respond to such demands and to envisage a high quality vehicle, the project City Lightweight Innovative Cab (the logo shown in Fig. 1) has been initiated.

Figure 1: City Lightweight & Innovative Cab (CLIC) project

This project is set to develop a new generation of an urban truck within the range of transport vehicle products that will have a new cabin design in lighter weight. The project aims at reducing a body mass of the existing truck cabin by minimum 15 % which in turn results in reduction of carbon dioxide (CO2) emission. However, such mass lightening will inevitably lead to a decrease of acoustic performance for a driver's environment in the cabin space. Therefore, the principal objective of the project CLIC is to conserve NVH (Noise Vibration and Harshness) performances of the initial design. This will require a careful mass optimization process as well as comprehensive vibroacoustic knowledge of the truck cabin body-in-white (BIW). Evidently, the vibroacoustic analysis should be carried out for the fully trimmed

body as to the gaining of desirable acoustic performance, which necessitates a proper technique to model and to predict the damping effect. Therefore, this research aims at developing a vibroacoustic prediction method that can describe the dynamic behavior of the structure with/without trim components.

Research Description

This Ph.D research undertakes vibroacoustic analysis of a structure-fluid system (cabin body and cabin space shown in Fig. 2) including the modeling techniques of the damping effect induced by dissipative treatments for the mid-frequency domain. Most commonly used numerical methods, namely the finite element and the statistical energy methods face the limitation in terms of the frequency range of interest to which analyses can be performed. The finite element method is limited to the low-frequency domain while

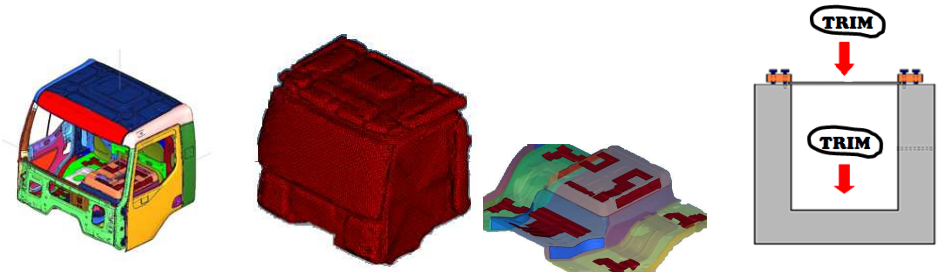

(a) (b) (c) (d)

Figure 2: Structure-fluid system (cabin body surfaces and cabin air space): (a) Truck cabin BIW, (b) Cabin air space (3D solid mesh), (c) Cabin floor with trim components (red and blue patches), (d) Plate-cavity system with trim components

the statistical energy method is only applicable to the high-frequency domain. Consequently, there is the absence of the modeling capabilities that numerical methods can fill out the the mid-frequency gap. The objective of this research, therefore, lies on the development of a vibroacoustic prediction method capable of analyzing a complex mechanical system for the mid-frequency domain. The dynamic analysis shall be carried out on the whole structure, and the localized damping effect induced by vibrational and acoustical damping materials should be taken into account. In order to carry out such tasks, the Statistical modal Energy distribution Analysis method (SmEdA) [60] has been selected in this research. This method has been developed as an extension of the SEA method by resolving the energy equipartition assumption. It can be well adapted to the mid-frequency analysis for heterogeneous systems or local excitations. However, localized dissipative treatments has not been considered in the original formulation in which the constant damping loss factor is generally considered for subsystem resonant modes. The objective of this Ph.D research is then to develop and to validate the methodology for including the effect of dissipative treatments in the SmEdA model.

To validate the proposed methodologies, laboratory test cases of the structure-fluid problem composed of a rectangular plate coupled to a parallelepipedic cavity (Fig. 2d) are considered. Such system simplifies the truck cabin and can be used to study the vibroacoustic interaction between structure and fluid as floor-cabin space and rear surface and cabin space interactions are of interest. Within the simplified setup, dissipative treatment configurations can be easily manipulated and precise physical parameters are manageable.

CHAPTER 1

Research Context and Bibliography

This chapter will present the scientific context of this Ph.D research in three sections:

- Section 1.1 gives an overview of the most popular vibroacoustic modeling techniques used in industry and their limitations. This is followed by the introduction of recently developed numerical techniques for the mid-frequency analysis.
- Section 1.2 presents various modeling techniques of the damping effect induced by dissipative materials, namely viscoelastic and poroelastic.
- Section 1.3 presents vibroacoustic techniques commonly used to predict the response of mechanical structures including dissipative treatments.

1.1 Vibroacoustic modeling techniques for the mid-frequency domain

In the vibroacoustic analysis of complex mechanical structures, analytical solutions may not always be available due to the nature of geometric, material and dynamic complexity. There are various numerical techniques providing approximated solutions using different physical quantities i.e. wave, energy, ray, etc. For structure-bounded fluid systems, the fluid dynamics enclosed by structures and the interaction between vibration field and sound fields are mainly of interest. Practical examples include vehicle cabin spaces, acoustic enclosure of industrial machineries, duct/pipes transporting fluids and loudspeaker enclosures. Computer aided vibroacoustic analyses implementing various numerical methods have become a common

proceeding in the design, analysis and optimization process of today's industrial manufacture. Among many techniques, deterministic and statistical methods have been commonly used for a broad range of engineering applications for many decades.

The Finite Element Method (FEM) [8] is a most commonly used dynamic analysis tool that can be successfully implemented for all types of structures. Within the method, the field variables that are distributed over discrete points in an elastic medium are expressed in terms of degrees of freedom. The vibration field must satisfy the relevant governing wave equation, and the solution is obtained by assuming the interpolation functions that approximates a distribution of the field variables at nodal points [37]. The main drawback is that the method is limited to the low-frequency domain since the use of piecewise polynomial shape functions yields a large number of degrees of freedom with increasing frequency. Although a computation may be performed to any range desired with powerful computer capabilities of recent days, no valid results are expected since the dynamic response becomes sensitive to small perturbations at high frequencies, leading to significant errors as a result of consecutive arithmetic operations accumulated [37].

As for the high-frequency domain, the behavior of a structure may be described in terms of energy and input power rather than waves and harmonic forces of excitations that element-based methods consider. The Statistical Energy Analysis (SEA) [53] gives an ensemble description of vibration of a system under study. The method implements subdivision of the structure of which time and frequency averaged mean-square vibration response is sought for a given frequency band. The excitation is normally assumed to be broad band and stationary since the ensemble energy that flows between subsystems can occur under the assumption of equally distributed vibrational energy among subsystem resonant modes. However, such assumption imposes subsystems to have a sufficiently large number of resonant modes in a given frequency band, limiting its frequency range to the high domain.

Vibroacoustic performance of large scale industrial applications, namely automotive and aerospace, is highly affected by the mid-frequency behavior that can not be addressed by FEM and SEA. For instance, airborne transmission of machine noise is a dominant path in vehicle cabin space at mid to high frequencies [86]. The perception of acoustic comfort inside the vehicle is subject to frequencies above 400 Hz which typically dominated by noise levels above 1 kHz [68]. For achieving desirable NVH performances that differentiates a product its commercial values, the mid-frequency analysis is indeed imperative. Evidently, aforementioned methods are not best suited for the frequency range of interest. Such fundamental gap in modeling capabilities leads to a development of an adequate modeling technique suitable for industrial applications. In following subsections, various mid-frequency modeling techniques developed since late 90's are introduced.

1.1.1 Wave based method

The WBM (Wave Based Method) is a deterministic technique approximating the dynamic field variables of a problem by expansions of globally defined, exact solutions (known as indirect Trefftz approach). It is differentiated from typical element based methods by introducing bounded and unbounded subdomains on a system under study [31] [32]. The problem domain is partitioned into a few large convex subdomains in which field variables are expanded by selecting wave functions that exactly satisfy the governing equation.

The weighting factors of each selected wave function are the degrees of freedom in the solution expansion. A linear system equation is formed by defining boundary conditions using a weighted residual formulation and continuity conditions between subdomains. This can minimize the approximation errors on the subdomain boundaries [33]. Fig. 1.1 illustrates a two dimensional soundfield computed using the WBM method. Compared to the FEM, the method can reach the mid-frequency domain due to its significantly smaller system matrices. It can deal with a broad range of application from two/three dimensional acoustic problems to hybrid vibroacoustic coupled problems.

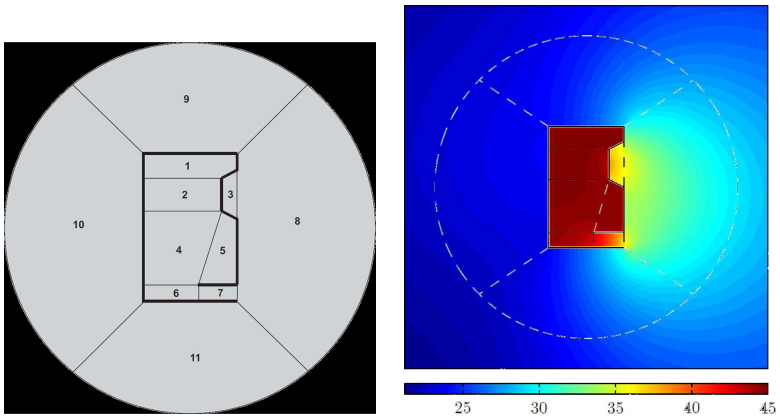

(a) (b)

Figure 1.1: The WBM example 2D exterior acoustics. Computation of a sound field [73]: (a) Subdivision of the problem domain, (b) Sound pressure levels

For an unbounded domain such as acoustic radiation problem, the problem domain is partitioned into two non-overlapping regions with a truncated geometry (normally a circle and a sphere for two/three dimensional problems respectively) [31]. Then the bounded region inside the geometry again breaks down to several convex subdomains, and the unbounded region outside the geometry is treated as a single subdomain. When the system equation is solved, unknown wave function contributions are obtained which needs to be back-substituted into the field variable expansion.

Within FEM approach, the problem domain should be discretized with sufficiently small element size in order to ensure prediction accuracy. A WBM model, on the other hand, requires subdomains whose sizes are independent of frequency. However, the dynamic field variables inside each subdomain are described by a number of wave functions that can increase at high frequencies [33]. Nonetheless, a computational cost of a WBM model is still less than that of FE models since the size of resulting FE system matrices is relatively larger. A major advantage of this approach compared to FEM is that the convergence rate is higher which enables a system analysis of a high frequency domain without computational limitations [33]. In addition, the method can be incorporated other approaches (FE and SEA) in order to further reduce a computational cost.

1.1.2 Hybrid FE-SEA method

The hybrid FE-SEA method combines the proficiency of FEM and SEA techniques so that it can cover a broad audio frequency range for a system under study [78]. The entire structure is analyzed as an ensemble

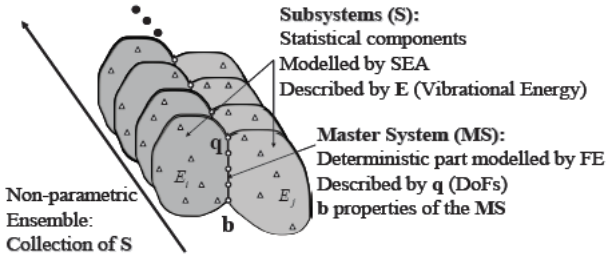

Figure 1.2: Hybrid FE-SEA model description [25]

of deterministic components modeled with FEM and random components modeled with SEA. Properties of the systems vary across the ensemble as seen seen in Fig. 1.2. The subsystem energy exchange of the ensemble average follows the standard SEA equation with addition of the master system to which power is injected.

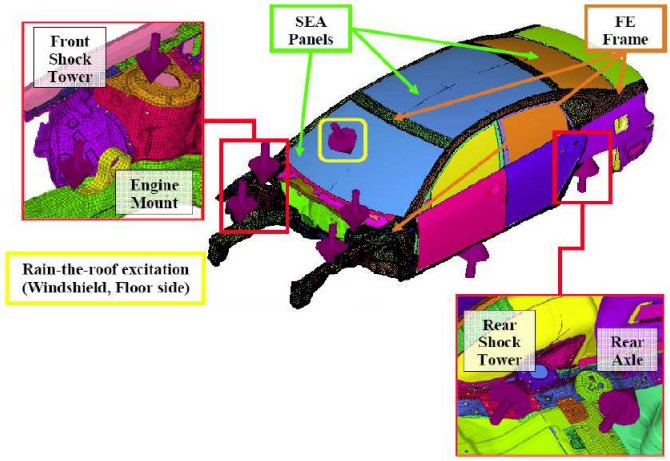

Figure 1.3: Automobile application for Hybrid FE-SEA [23]

The SEA components are described by random physical properties (geometry, density, modulus, etc.) varying throughout the coupled structure and are coupled through the master system whose degree of freedom can be always considered between coupled subsystems. Rather than considering the details of each subsystem parameters, the system resonances and mode shapes are sought according to certain statistical distributions. When the structure is load by dynamic force, the response is a contribution of a direct field defined by the initial wave and a reverberant field defined by boundary reflections. The direct field is a deterministic stiffness matrix evaluated at each coupling junction between SEA subsystems. The reverberant field is assumed to be isotropic that can describe the randomness of subsystem properties [78]. Two fields (FE and SEA components) are then coupled together based on the diffuse field reciprocity relation in which the cross spectrum of the reverberant force is expressed in terms of the ensemble average vibrational energy [25]. Another key assumption of the method underlines that each SEA subsystem should be weakly coupled through the master system.

One of many industrial applications that this method can be applied to is a prediction of an interior noise level of an automotive vehicle for a frequency range well above 200 Hz [33]. As shown in Fig. 1.3, the

partitioning components (chassis, engine support, etc.) can be modeled as FE components, and all other body parts (floors, doors, windows, etc.) are modeled as SEA components. A major advantage of this methodology is that an analysis can be done for a broad frequency range with relatively low computational cost.

1.1.3 Waveguide finite element method

The Waveguide finite element method is an alternative deterministic approach that is highly efficient for structures of waveguide-like properties. The waveguide FEM describes a structure with the propagation of mechanical waves along the geometrical extent assumed to have constant properties. As a structure has a homogeneous uniform geometry, the system equation of motion is formed with the wave propagation along a single axis [33]. The equation of motion consists of a set of coupled ordinary differential equations of which the eigenvalues can be easily determined.

With certain boundary conditions satisfied by a wave solution of the traveling waves, the eigenvalues are calculated as in a two-dimensional domain. In addition, the solutions are determined for a cross section, geometrical coordinate along the waveguide and time dependency and such solution sequences allow different wave types to be easily identified, that is useful for diagnostic purposes and provides a comprehensive understanding on the physics of the system [1].

The Waveguide approach requires a discretization of the cross section of the system only and is benefited from substantial reduction on the number of degrees of freedom for structures whose length is larger than the dimension of the cross section [33]. As a result, a major advantage of the method over the conventional FEM lies on an ability to expand a frequency range of analysis with a drastic reduction of computational cost. Obtained solutions of the wave equations can be used to evaluate the dispersion curve, group velocity and modal density that can be further used in an energy method such as SEA. Its application can include a transmission path study of a built-up system, an effect of damping treatment and a diagnostic analysis of structures like a wind tunnel and railway vehicles. Fig. 1.4 shows the method applied to obtain the pressure field and deformation of a train section under a point force excitation.

1.1.4 Statistical modal energy distribution method

The SmEdA (Statistical modal Energy distribution Method) is a numerical method originally developed to overcome the shortcoming of the classical SEA assumption. The SEA methodology constitutes statistical assumptions on subsystem modal groups to which energy is equally distributed within the frequency band (Δf), known as equipartition of subsystem modal energy. This requires physical properties of the system such as the excitation and vibrational response to be quantified in strict terms: under the weak and direct coupling between subsystems, the excitation is broadband and stationary and the subsystem modal overlap (the average number of modes whose natural frequencies fall within the half-power bandwidth of any one mode at a given excitation frequency) exceeds unity [38]. The system response can be then estimated as average behavior of an ensemble of similar structures and is not sensitive to small structural variations. However, in case of low modal overlap i.e. either low modal density or low damping or both, the SEA

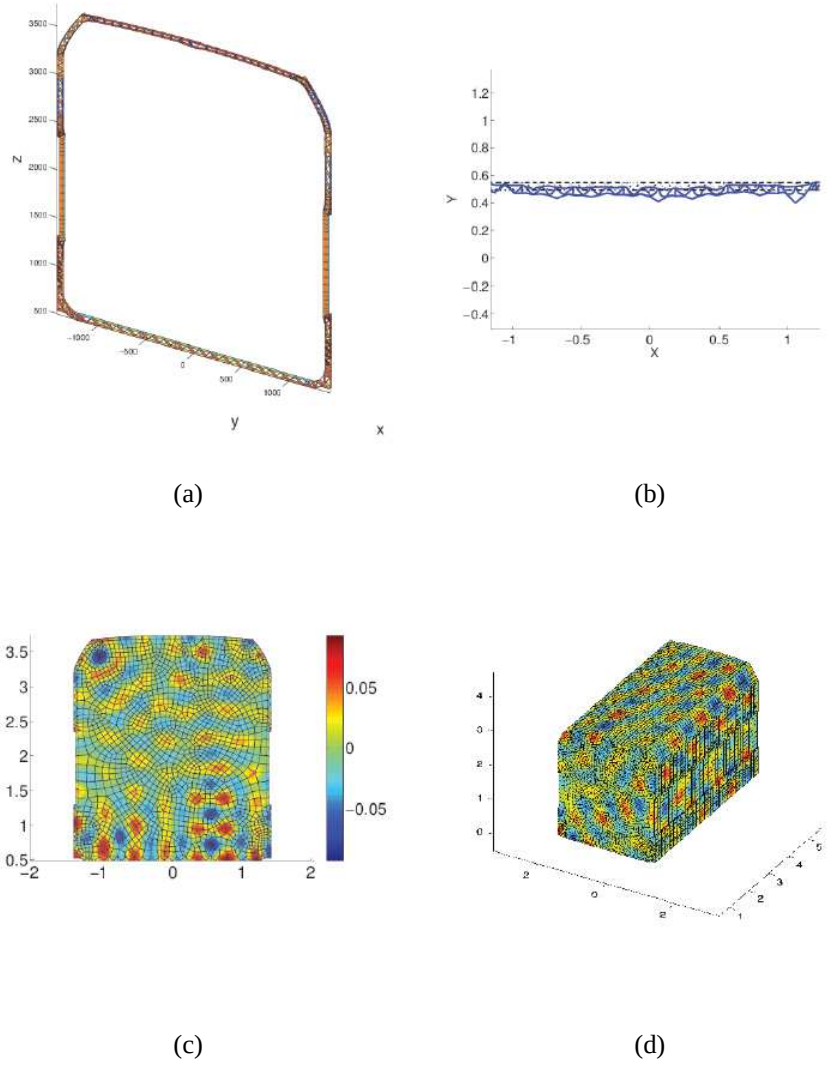

(a) (b)

(c) (d)

Figure 1.4: Waveguide FEM analysis on a train section [33]: (a) Mesh of a train cross section, (b) Deformation of the train floor at 900 Hz, (c) Pressure field of the cross section, (d) Pressure field of section at 700 Hz

prediction yields errors and has shown to overestimate the modal energy of a receiving subsystem except for structures of identical subsystems [91].

The SmEdA can be, in fact, applied to the mid-frequency domain since the SEA limitation of the low modal overlap is resolved, extending its frequency range to the lower domain. Contrary to the SEA, the subsystem coupling is deduced from the knowledge of uncoupled subsystem modes using the Dual Modal Formulation. With modal information of uncoupled subsystems deduced from the FEM, the energy flow can be apprehended to the mode-to-mode level rather than the ensemble energy that dictates the classical SEA theory. By the use of the FEM, the method benefits from the flexibility to model a complex geometry thus feasible for industrial applications. Originally derived for a structure-structure system [58] [60] based on the Dual Modal Formulation by Karnopp [48], the method has been successfully applied to a structure-fluid system as well [80] [81]. Fig. 1.5 shows the distribution of energy inside the TGV Duplex train (structure-fluid system) determined using the method. A recent extension of the method includes

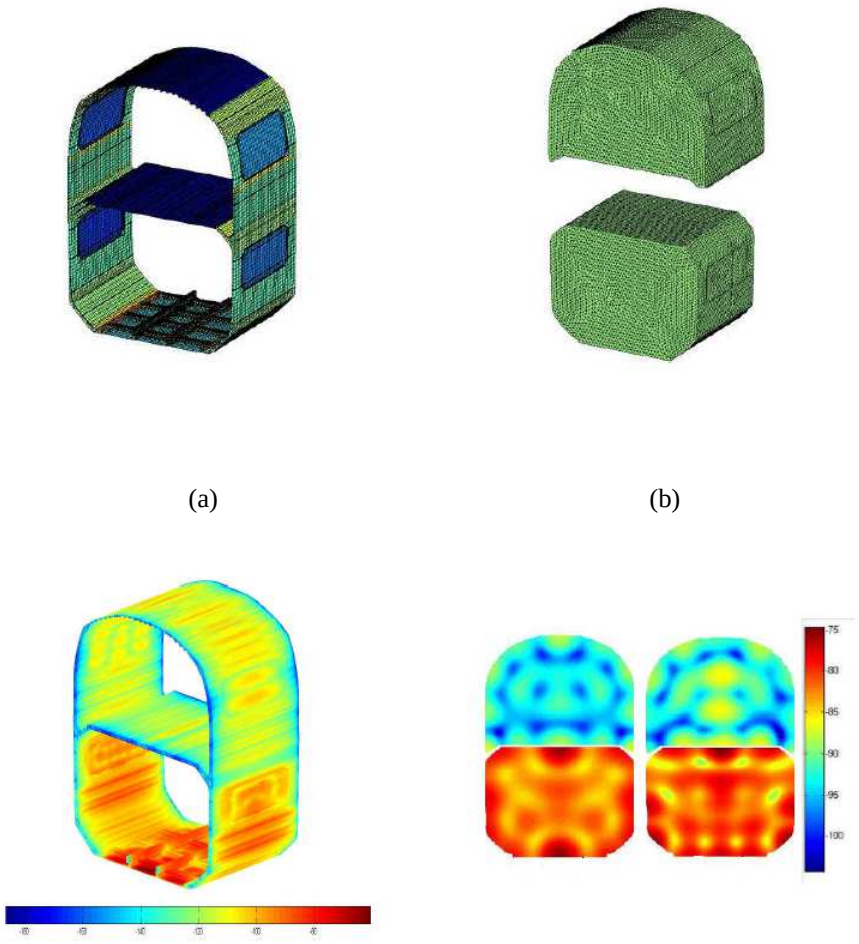

(a) (b)

(c) (d)

Figure 1.5: SmEdA analysis on TGV Duplex [82]: (a) Structure of the train section, (b) Two acoustic volumes, (c) Distribution of energy deformation at 315 Hz, (d) Distribution of total energy in the acoustic cavities at 315 Hz

the energy transmission through nonresonant modes for both structure-structure and structure-fluid systems [79] [59]. For this Ph.D research, the SmEdA approach has been adopted for the mid-frequency analysis. The objective is to extend the method to solve a structure-fluid problem including the damping effect induced by dissipative materials, namely viscoelastic and poroelastic. The method will be further detailed in Chapter 2.

1.2 Modeling of dissipative treatments

1.2.1 Viscoelastic

Noise and vibration reduction techniques for a built-up system are commonly divided into three categories: active, semi-active and passive control methods. The passive control is a predominant method for structure-borne vibration and noise problems since it is more cost-effective and easier to integrate into a complex sound field [67]. Vibratory response and dynamic stress can be effectively dissipated or isolated by adding damping materials to the base structure. The damping refers to the conversion of mechanical energy into heat as the material damping means a material property itself [67]. In order to describe a physical nature of damping, various terms exist i.e. proportional, viscous, hysterestic, etc. to facilitate a mathematical modeling. Nonetheless, the actual mechanism is not fully comprehended in many cases.

Passive damping method (by adding dissipative materials) has been popular in complex engineering applications since the advances in material technology. The use of a viscoelastic material for a system loaded by a broad range of frequency is predominant. Polymeric materials (rubber, plastic, urethanes, epoxies, etc.) are viscoelastic and are widely utilized in many industrial applications. A layer of viscoelastic material is applied to structural elements that are normally a form of beams, rods, plates and shells. Typical approaches consider the dynamic properties of linear viscoelastic materials represented by the complex modulus [67].

The complex modulus approach allows a consideration of environmental factors into a study of viscoealstic material properties. As the material is highly dependent on ambient temperature, loading frequency and humidity, a comprehensive understanding of such effects is crucial in order to facilitate materials in use. Although the theoretical base of many techniques to model viscoelastic materials is complex modulus, much of research undertaken in this area can be divided, based on the layer configuration applied to a base structure. A damping treatment of a viscoelastic layer has three typical designs: (1) a free layer that is a single layer treatment of a viscoelastic material directly applied to the base structure, (2) a constrained layer or sandwich layers that have a constraining skin covering the viscoelastic layer, and (3) tuned damper which is similar to a dynamic absorber that normally targets a single frequency or a narrow frequency band [67]. The first two designs are most commonly used in industries (particularly automotive and aerospace). These are further discussed in following sections.

1.2.1.1 Free layer damping

A single layer of damping material also known as a FLD (Free Layer Damping) is usually glued or laminated to a base structure. As the base structure deflects in a flexural manner, the viscoelastic layer extends and compresses in parallel to the base as seen in Fig. 1.6. The complex modulus approach to describe the viscoelastic characteristics was first introduced by Oberst and Lienard in 1952 [49]. Flexural vibration on a finite beam treated with a single homogeneous viscoelastic layer was analyzed, and its prediction and measurement methods were introduced. Note that the viscoelastic layer was uniformly applied over a full surface area of the base structure in this study. In many practical applications, only a partial treatment

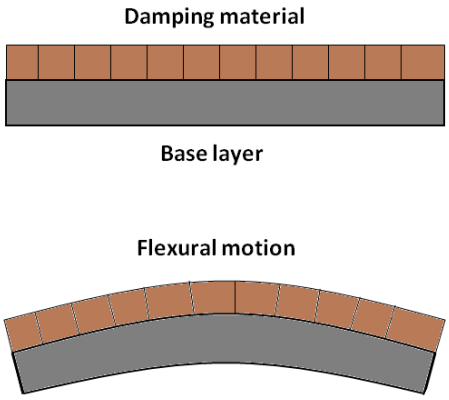

Figure 1.6: Free layer damping

of the material is possible and a total mass of treated structure became an important factor. McQuilin and Kerwin [63] first presented the study of the patch application with a beam having a one-dimensional standing wave. The system damping was evaluated as a function of patch length, viscoelastic material loss factor and constraining-layer boundary conditions. An analytical model was given wherein the damping was evaluated as the product of a fractional surface coverage.

Parthasarathy and Reddy [71] studied a partial coverage of FLD on a rectangular plate. Using the finite element approach, a maximum damping effect was sought with a minimum mass of the material applied based on different layer configurations as well as a thickness. The system loss factor with a partial configuration of FLD depends on modes (resonances and modeshapes) contrary to the full coverage where a damping performance is independent of such factors.

1.2.1.2 Constrained layer damping

A constrained layer damping (CLD) is the FLD formation layered with extra outer skins. Its arrangement normally includes a viscoelastic core with an outer layer that is stiffer than a core material. It can also be a multi-layer configuration depending on applications. Outer layers can be made out of stiff elastic materials as well as thin metals [67]. A constraining layer induces a shear deformation as seen in Fig. 1.7 that dissipates vibratory energy greater than what the FLD formulation does. Since its high cost-effective performance, the CLD formulation has been used in a broad range of industrial applications.

Theoretical expressions of CLD were first developed by Kerwin [49] and were demonstrated on a finite beam fully treated with two-layer damping materials. The complex shear modulus was assigned to the constraining layer where much of dissipation is assumed to take place. This was followed by Mead and Markus [64] who developed a sixth order differential equation expressing the transverse displacement on a sandwich beam. Since then, numerous publications have been made on full and/or partial treatments based on displacement approaches. Different theories were developed to describe beam and plate structures and were predominantly solved by the FEM or the Rayleigh-Ritz's method (trigonometric basis) [64] [89] [76] [45] [2] [54].

The CLD formulation as well as multi-layered plate arrangement can be dealt with a three-dimensional

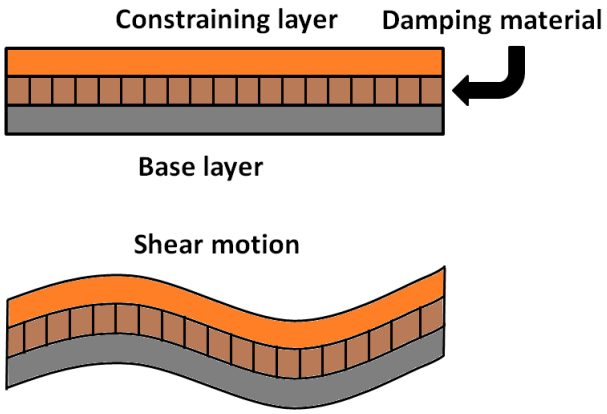

Figure 1.7: Constrained layer damping

FEM. However, such approach easily encounters a computational limitation at high frequencies. A majority of research, therefore, has been based on the two-dimensional Classical Lamination Theory (CLT) of the Love-Kirchoff's thin plate. This model, by eliminating the thickness dimension, assumes no transverse shear deformation but takes into account membrane and bending motions of the structure. This approach is appropriate and efficient for thin plates but is no longer feasible when the shear deformation becomes non-negligible for thick plate cases. The first order shear deformation theory (SDT) using Reissner-Mindlin's assumption can undertake multi-layered thick plate cases [20]. Within this method, the membrane deformation depends on bending motion as well as shear motion that is assumed to be constant through the plate thickness. This, however, requires shear correction factors in order to consider the transverse shear stress variations [67]. Many commercial FEM solutions are based on CLT and SDT formulations. Higher order shear deformation theories are also proposed [52] [74] wherein a number of unknowns in equations of motion exceed five.

In order to reduce a model size of the multi-layered plate arrangement, Guyader and Lesueur [42] introduced an equivalent single layer modeling. This method is based on multi-layered plate equations and considers the wave propagation to determine equivalent plate properties in order to give the same transverse displacement as a multi-layered composite plate. It drastically reduces computation resources by simplifying two-dimensional element based models using equivalent parameters assigned to the region of a plate where any number of layers are placed upon. To model the damping effect in the structural system treated with a viscoelastic layer, this method has been adopted in this research. The method is further detailed in Section 3.2.1.

A partial treatment of the CLD formation (a patch arrangement) yields a cost-effective high performance compared to a full treatment. This saves a significant amount of material used, lead to a lighter mass of the final product, therefore, it has been increasingly popular in automotive and aerospace applications. For past two decades, many researchers have taken part in optimization study of a patch arrangement in order to maximize the system modal damping by selecting the optimal material while minimizing a weight by determining the optimal geometric parameters of the treatment over the surface of base structure. Mantena et al. [55] analyzed composite laminated beams with a CLD treatment and determined an optimal CLD distribution for the maximum damping. Many studies [9] [56] [93] haven been conducted concerning the

dimension/layout/location of the patches as design variables.

1.2.2 Poroelastic

Under the passive control category, air-borne noise problems are typically managed by partitions, absorbers, silencers, membrane resonators and such. Among them, porous materials such as polymer foams or mineral/glass wools are exceedingly popular for sound absorption and insulation purposes because of their light weight and easy replaceability. Fig. 1.8 shows microscopic images of some porous materials.

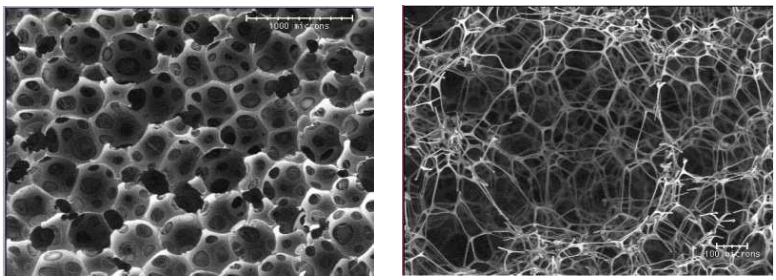

(a) (b)

Figure 1.8: Photograph by scanning electron microscope of the microscopic structures of porous materials [28]: (a) High density polyurethane foam, (b) Low density melamine foam

For the most part, currently available modeling techniques of porous materials are credited to Maurice Anthony Biot. He laid the foundation of the poroelasticity (porosity) theory (also known as Biot theory/model) [13] [14], which describes the mechanical behavior of fluid-saturated porous media. His model describes the poroelastic (normally called porous) medium by macroscopic displacements of solid and fluid phases represented by u^s and u_f respectively. One shear and two compression wave propagations are considered in the (u^s, u^f) formulation in which two phases are coupled through the elastic and thermal moduli. Since the Biot's establishment, a vast majority of the research has been stretched from his original formulation. Atalla and Panneton [5] [4] later proposed the mixed formulation (u^s, p) with field quantities of the solid displacement and the interstitial pressure p of the fluid. Within that model, six unknown fields of the original Biot's model are reduced to four. All of the models require a number of parameters describing the solid and fluid properties of a porous material: porosity ϕ, flow resistivity σ, tortuosity α_∞, viscous Λ and thermal Λ' characteristic length, solid ρ_s and fluid ρ_f density respectively. These parameters can be determined directly [65] or indirectly [83] [70].

A large computational cost is problematic which limits both original and mixed formulations to the low-frequency domain when discretizing the problem in finite extent (four and six degrees of freedom per node respectively). To bypass this problem, porous materials can be modeled as a dissipative fluid medium under the assumption of the solid phase being either rigid or limp. This model, known as equivalent fluid, was first proposed by Zwikker and Kosten [94]. The rigid frame model [3] [6] assumes the solid frame a motionless structure so that a single compression wave propagates inside porous medium. The limp model, proposed by Beranek [11] and further studied by Ingard [44] and Dazel [27], neglects bulk stiffness of the solid frame but accounts for its viscous and thermal dissipation mechanism. To the FE extent, both models have only a single degree of freedom per node by eliminating the solid displacement. In this research, the

equivalent fluid technique has been adopted for modeling the acoustic damping by the porous material. It drastically reduces a model size and all necessary parameters are obtainable through simple impedance tube measurements while the Biot's model parameters are normally available through manufacturer's aid. The method is further detailed in Section 3.2.2.

As the simplest approach to model a porous material, the empirical models are available. First proposed by Delany and Bazley [30] in 1970, the method uses no other than the flow resistivity of the material from which the characteristic impedance and the wave numbers are deduced. The density and the compressibility are formulated through the fitting procedure based on a large number of materials tested in impedance tube measurements [28]. However, it was later realized that this model can induce negative impedance by violating the Kramers-Kronig relations [28]. Miki [66] revised the method to eliminate this problem by implementing power laws functions.

1.3 Vibroacoustic modeling including dissipative treatments

In many vibroacoustic applications, mainly automotive and aerospace context, prediction models are required for structures treated with dissipative materials i.e. fully trimmed vehicle bodies. Trimmed structures are typically modeled in FE and/or SEA extent with various methodologies implemented to capture the characteristics of trim components.

In FE environments, many commercial solutions model viscoelastic treatments with shell or solid elements using the CLT and SDT formulations that can represent the mass, stiffness and damping of trim components. Coupling mechanisms (point, line, surface, etc.) are defined between structures and trim components and the system response is computed. In case of porous materials, the Biot's model may be fully implemented [69]. To reduce the computational cost, the mixed formulation (u^s, p) as well as the equivalent fluid models (u^f) are used in many commercial codes. Under practical circumstances of the industrial process, however, acoustic trim components are often over-simplified by the use of global damping constants and non-structural masses [17].

Within the SEA extent, trim components are mostly concerned with acoustic treatments in terms of the airborne noise prediction. The transmission path of a vehicle cabin space is commonly analyzed using the Transfer Matrix Method [3] obtained from the Biot's formulation [35] [23]. The vehicle cabin space is normally subdivided into acoustic SEA subsystems where the subsystem damping is typically induced by the boundary absorption [68].

With the use of FEM and SEA techniques, the frequency limitation issue prevails. The main challenge, most of all, is that the frequency-dependent characteristic of trim components impedes modal analysis and the near-field behavior yields highly localized effects [47]. In order to resolve these difficulties, recent research and development projects extend the mid-frequency techniques (introduced in Section 1.1) to a system analysis of trimmed structures. Numerous studies have been undertaken using the WBM [47] and hybrid FE-SEA [23] [22] [24] [86] methods mostly concerned with coupled structures of porous applications. The hybrid FE-SEA technique implementing the Biot's model has been demonstrated effective for the interior noise prediction of fully trimmed vehicles for the mid-high frequency range.

1.4 Conclusion and summary of the thesis

The project CLIC aims to develop a lighter-weight truck that maintains NVH performances of the initial design. The main objective of this research, therefore, is to establish a full vibroacoustic prediction model of a complex structure-bounded fluid system i.e. cabin body surfaces and cabin space treated with vibrational and acoustical damping materials for the mid-frequency domain. Since most commonly used element based and statistical methods are not suitable for the frequency domain, a proper prediction tool, which is flexible in modeling capabilities and feasible in computational cost, must be implemented. Driven by the high industrial interest, different numerical methods have been developed in recent years. Although many of these methods have been validated, the mid-frequency analysis remains to be a topic of prolific research.

For the project CLIC, the SmEdA method, originally developed to alleviate the classical SEA assumption, is considered for the mid-frequency vibroacoustic analysis of a trimmed structure. The method is extended to take account of the damping effect induced by dissipative materials in this research where development and validation of the methodologies are carried out. Dissipative materials (typically called trim components in automotive context) such as a viscoelastic layer and a poroelastic membrane will be applied to plate and cavity respectively. The viscoelastic layer will be fixed to the plate that is modeled as an equivalent plate [42]. The poroelastic membrane inside the cavity will be modeled as an equivalent fluid [94]. The modal damping loss factors of treated subsystems will be deduced using the Modal Strain Energy method [84] and Modal Strain Kinetic Energy methods [88]. Different configurations of dissipative treatments will be arranged and analyzed in the framework of SmEdA, and subsequent results are experimentally evaluted.

This Ph.D thesis is composed of five chapters:

- Chapter 2 reviews the formulation of SEA power flow equation. This is followed by the fundamental of the SmEdA method based on two oscillators coupled through a gyroscopic element. The method is then applied to the plate-cavity test case without presence of dissipative materials.
- Chapter 3 presents the modeling techniques of: (1) the vibrational damping by the equivalent plate model of viscoelastic materials, and (2) the acoustical damping by the equivalent fluid model of porous materials. Methodologies of each modeling technique and calculation examples will be given. This is followed by the modeling techniques to estimate the modal damping loss factor of the equivalent models of dissipative materials: (1) the Modal Strain Energy method for a damped plate subsystem, and (2) the Modal Strain Kinetic Energy method for a damped cavity subsystem.
- Chapter 4 presents the extension of the SmEdA method (analysis of the damping effect). For the test case, different damping configurations will be considered. Computation results are analyzed and compared between the test cases with/without dissipative treatments.
- Chapter 5 presents comparisons of the SmEdA results with experimental ones. The experiments are carried out with a point force (white noise) exerted on the plate. Measured quantities are the input mobility, injected power, subsystem damping loss factor and subsystem energy levels. Numerically approximated subsystem modal damping loss factors (using Modal Strain Energy and Modal Strain

Kinetic Energy methods) are compared to experimentally estimated results. Input mobility, injected power and subsystem energy levels are compared to predicted ones, and conclusions are drawn.

- Finally, the general conclusion and the research perspective are given in Chapter 6.

CHAPTER 2

Statistical Modal Energy Distribution Analysis

This chapter presents the mid-frequency vibroacoustic modeling of a structure-fluid problem based on the SmEdA method. The method is an extension of the SEA method by resolving the modal energy equipartition assumption. A brief reminder of the SEA method is given before introducing the SmEdA formulation for a general case. The method is then applied to a structure-fluid problem composed of a rectangular plate coupled to a parallelepipedic cavity.

2.1 Statistical energy analysis

Lyon [53] derived the general equation of energy transfer for two linearly coupled subsystem driven by random, broadband excitation. He showed that an average power flow between coupled groups of dynamical modes are proportional to the difference in average modal energies. It has been shown that the relation holds in the limit of "weak coupling" for a system represented by three or more arbitrarily coupled subsystems [38]. Fig. 2.1 describes the power flow within the system consisting of two linearly coupled subsystems. $\Pi_{1,inj}, \Pi_{2,inj}$ are the input powers injected into the subsystem 1 and 2 by a stationary harmonic force, and $\Pi_{1,dis}, \Pi_{2,dis}$ are the powers dissipated within the subsystems. Π_{12} and Π_{21} indicate the power transmitted from subsystem 1 to subsystem 2 and from subsystem 2 to subsystem 1. The power exchange between two subsystems can be written as

$$\begin{aligned} \Pi_{1,inj} &= \Pi_{1,dis} + \Pi_{12}, \\ \Pi_{2,inj} &= \Pi_{2,dis} + \Pi_{21} \end{aligned} \tag{2.1}$$

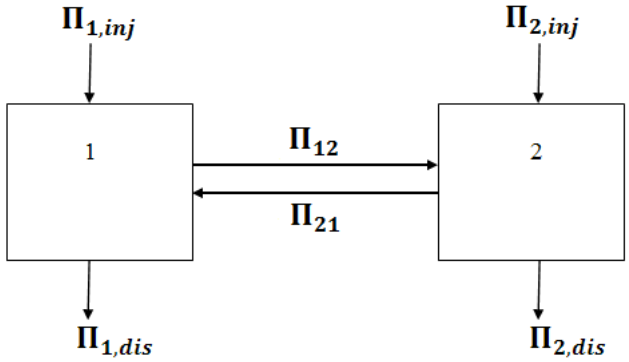

Figure 2.1: A two-subsystem SEA model

The dissipated power is given by

$$\begin{aligned} \Pi_{1,dis} &= \omega\eta_1 E_1, \\ \Pi_{2,dis} &= \omega\eta_2 E_2 \end{aligned} \tag{2.2}$$

where E_1, E_2 are total dynamic energies of the mode of subsystem 1 & 2 at angular frequency ω, and η_1, η_2 are the damping loss factors. The transmitted power is given by

$$\begin{aligned} \Pi_{12} &= \omega(\eta_{12}E_1 - \eta_{21}E_2), \\ \Pi_{21} &= \omega(\eta_{21}E_2 - \eta_{12}E_1) \end{aligned} \tag{2.3}$$

where η_{12}, η_{21} are the coupling loss factors. Note that while the damping loss factor η_1 is a rate at which energy is dissipated within the subsystem 1, the coupling loss factor is a rate at which energy is transmitted from subsystem 1 to subsystem 2. This can be expressed in terms of a difference of modal energies (average energy per mode) as

$$\Pi_{12} = \omega\eta_{12}n_1(\frac{E_1}{n_1} - \frac{E_2}{n_2}) \tag{2.4}$$

where n_1 and n_2 are the subsystem modal density. This equation explicitly displays that it is the differences of modal energies, not total energies, which drives the energy flow between subsystems [38]. Finally, the power balance Eq. 2.1 and 2.2 can be rewritten as

$$\begin{aligned} \Pi_{1,inj} &= \omega(\eta_1 - \eta_{12})E_1 - \omega\eta_{21}E_2, \\ \Pi_{2,inj} &= \omega(\eta_1 - \eta_{21})E_2 - \omega\eta_{12}E_1 \end{aligned} \tag{2.5}$$

Solving these equations gives total energy of each subsystem. From these total energies, more physical quantities can be deduced such as the time-space averaged square velocity of a structural subsystem and the time-space averaged square pressure of an acoustic subsystem. For a plate-cavity system, the total

subsystem energies are given by

$$E_{1,\Delta f} = \int_{f_1}^{f_2} \rho h L_x L_y \overline{V}^2 df,$$
$$E_{2,\Delta f} = \int_{f_1}^{f_2} \frac{L_x L_y L_z}{\rho c^2} \overline{P}^2 df \tag{2.6}$$

where $\overline{V}^2, \overline{P}^2$ are the time-space averaged squared velocity and pressure respectively, and L_x, L_y, L_z are dimensions of plate/cavity and h is a plate thickness.

2.2 Statistical modal energy distribution analysis

Statistical modal Energy distribution Analysis (SmEdA) was first developed by Maxit and Guyader [60] in attempt to resolve the SEA subsystem modal energy equipartition assumption. The method is applicable to a system of low modal overlap hence the mid-frequency domain.

2.2.1 Energy flow through two-coupled oscillators

Similar to SEA, SmEdA relation is based on the relation between two coupled oscillators of the masses M_1, M_2 and of the stiffnesses K_1, K_2 and damped by viscous dampers Δ_1, Δ_2. Two coupled oscillators are illustrated in Fig. 2.2. External forces F_1, F_2 applied to the system are exchanged through the coupling

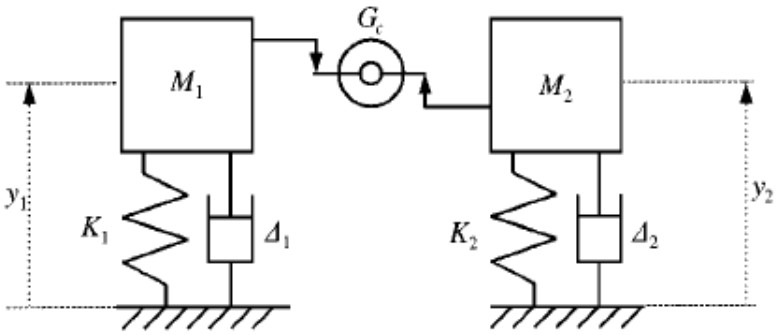

Figure 2.2: Two oscillators coupled by gyroscopic element [60]

constant G_c of the gyroscopic element that is proportional to the mass velocities $\dot{y}_1, \dot{y}_2$. The equation of motion is then given by

$$\ddot{y}_1(t) + \Delta_1 \dot{y}_1(t) + \omega_1^2 y_1(t) - \sqrt{M_1^{-1} M_2} \gamma \dot{y}_2(t) = F_1(t),$$
$$\ddot{y}_2(t) + \Delta_2 \dot{y}_2(t) + \omega_2^2 y_2(t) + \sqrt{M_1 M_2^{-1}} \gamma \dot{y}_1(t) = F_2(t) \tag{2.7}$$

where $\omega_1 = \sqrt{K_1 M_1^{-1}}$, $\omega_2 = \sqrt{K_2 M_2^{-1}}$, $\Delta_1 = \omega_1 \eta_1, \Delta_2 = \omega_2 \eta_2$ are respectively the natural angular frequencies and damping bandwidths of oscillator 1 and 2. γ is the gyroscopic modal coefficient and given

by $\gamma = G_c/\sqrt{M_1 M_2}$. The time averaged power exchanged between the oscillators is proportional to the difference between the time averaged total energies of the oscillators when the excitations are assumed to be uncorrelated, stationary and broad-banded. The time averaged power P_{12} between two linear oscillators is given by

$$P_{12} = \beta(E_1 - E_2) \tag{2.8}$$

It is known as the power-flow energy-difference proportionality relation [77] with the rate factor β given by

$$\beta = \frac{\gamma^2(\Delta_1\omega_2^2 + \Delta_2\omega_1^2)}{(\omega_1^2 - \omega_2^2)^2 + (\Delta_1 + \Delta_2)(\Delta_1\omega_2^2 + \Delta_2\omega_1^2)} \tag{2.9}$$

Notice that β involves only oscillator and coupling element parameter [77].

2.2.2 Dual modal formulation

A structure of two continuous mechanical subsystems shown in Fig. 2.3a that have linear elastic properties and viscous damping is considered. The system is loaded by a white noise with an angular center frequency ω_c. The dynamic behavior of the system can be then described by the Dual Modal Formulation (DMF) [48] based on the dual displacement-stress formulation.

According to the DMF, subsystem 1 is described by its displacement field and uncoupled-free modes and subsystem 2 is described by its stress field and uncoupled-blocked modes. Free and blocked boundary conditions of the uncoupled subsystem modes are illustrated in Fig. 2.3b. These subsystem modes can be

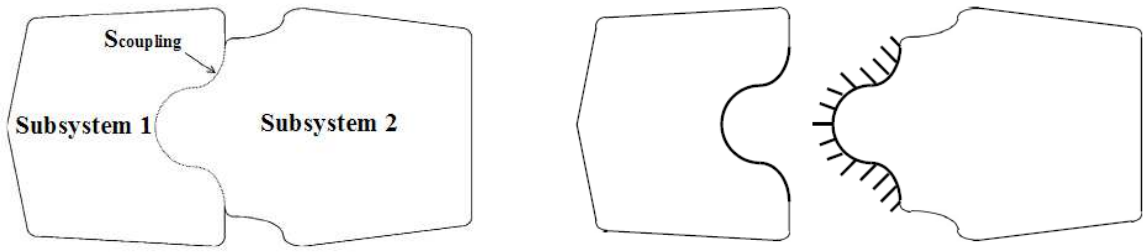

(a) (b)

Figure 2.3: DMF representation of a mechanical system [62]: (a) Coupling of two continuum mechanical systems, (b) Representation of the uncoupled subsystem boundary conditions (uncoupled-free subsystem 1, uncoupled-blocked subsystem 2)

easily obtained either analytically or numerically with FEM in case of a complex geometry. The modal expansions of the displacement W at point x of subsystem 1 and the stress σ at point x' of subsystem 2 can be written as

$$\begin{aligned} W(x,t) &= \sum_{n=1}^{N_1} a_n(t)\widetilde{W}_p^n(x), \\ \sigma(x',t) &= \sum_{m=1}^{N_2} b_m(t)\widetilde{\sigma}_q^m(x') \end{aligned} \tag{2.10}$$

where $a_n(t), b_m(t)$ are modal amplitudes, and $\widetilde{W}_p^n(x), \widetilde{\sigma}_q^m(x')$ are displacement modeshapes of subsystem 1 and stress modeshapes of subsystem 2. N_1, N_2 denote a number of resonant modes of subsystem 1 and 2 respectively.

The DMF consists of these expansions (Eq. 2.10) in a weak formulation of the vibroacoustic problem considered and using the orthogonality properties of the uncoupled modes [59]. With the change of modal variables,

$$b_q(t) = \dot{c}_q(t), \tag{2.11}$$

the modal equation of motion by the DMF is given by

$$\begin{aligned} &\ddot{a}_p^1(t) + \Delta_p^1 \dot{a}_p^1(t) + (\omega_p^1)^2 a_p^1(t) + \frac{1}{M_p^1} \sum_{m=1}^{N_2} \dot{b}_m^1(t) W_{pq}^{12} = \frac{F_p^1}{M_p^1}, \\ &\ddot{c}_q^2(t) + \Delta_q^2 \dot{c}_q^2(t) + (\omega_q^2)^2 c_q^2(t) - \frac{1}{(\omega_q^2)^2 M_q^2} \sum_{n=1}^{N_1} \dot{b}_q^2(t) W_{pq}^{12} = \frac{F_q^2}{(\omega_q^2)^2 M_q^2} \end{aligned} \tag{2.12}$$

where all variables are modal terms of uncoupled subsystem modes: mode p of subsystem 1 and mode q of subsystem 2. Δ_p^1, Δ_q^2 are the modal damping bandwidths, ω_p^1, ω_q^2 are the natural angular frequencies, M_p^1, M_q^2 are the modal masses, F_p^1, F_q^2 are generalized modal forces. Eq. 2.12 is analogous to Eq. 2.7

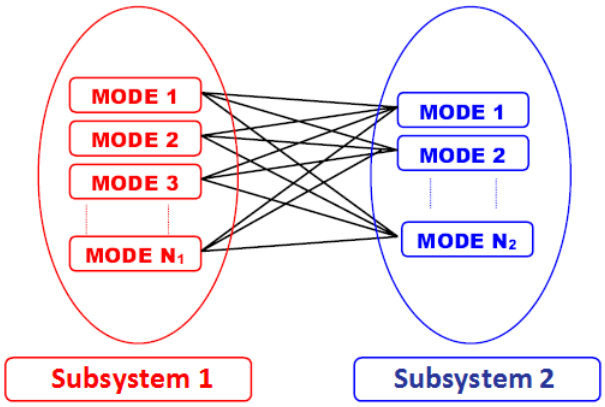

Figure 2.4: Schematic presentation of modal couplings between SmEdA subsystems [58]

of the two-coupled oscillator system. W_{pq}^{12} is the intermodal work over the coupling surface (S) between mode p of subsystem 1 and mode q of subsystem 2. It can be described with the subsystem modeshapes as follows

$$W_{pq}^{12} = \int_s \widetilde{W}_p^n \widetilde{\sigma}_q^m dS \tag{2.13}$$

The modal equation 2.12 explicitly shows that no direct coupling within the same subsystem occurs in a given frequency band. This is illustrated in Fig. 2.4

2.2.3 SmEdA modal energy balance equation

The SEA power balance equation (Eq. 2.1) between two subsystems can be reformulated in SmEdA modal energy terms. The power injected into mode p of subsystem 1 is dissipated within this mode and exchanged

with mode q of subsystem 2 as follows

$$\Pi^1_{p,inj} = \Pi^1_{p,dis} + \sum_{q=1}^{N_2} \Pi^{12}_{pq} \tag{2.14}$$

where Π^{12}_{pq} is power exchanged from mode p of subsystem 1 to mode q of subsystem 2. $\Pi^1_{p,inj}$ is injected power by the stationary white noise force and can be estimated using the relation established for one oscillator (subsystem 1). The injected power into mode p of subsystem 1 is given by

$$\Pi^1_{p,inj} = \frac{\pi S_F}{4M_p} \tag{2.15}$$

where S_F is the power spectral density of the generalized force in N^2/rad/s. $\Pi^1_{p,dis}$ is power dissipated by the internal damping of mode p and can be related to the modal energy as follows

$$\Pi^1_{p,dis} = \omega^1_p \eta^1_p E^1_p \tag{2.16}$$

where E^1_p, η^1_p are respectively energy and the damping factor of mode p.

The coupling through which energy is exchanged between mode p of subsystem 1 and mode q of subsystem 2 can be isolated in the modal Eq. 2.12 as follows

$$\begin{aligned}
&\ddot{a}^1_p(t) + \Delta^1_p \dot{a}^1_p(t) + (\omega^1_p)^2 a^1_p(t) + \sqrt{\frac{(\omega^1_p)^2 M^2_q}{M^1_p}} \frac{W^{12}_{pq}}{\sqrt{(\omega^2_q)^2 M^1_p M^2_q}} \dot{b}^2_q = L^1_{pq}(t), \\
&\ddot{c}^2_q(t) + \Delta^2_q \dot{c}^2_q(t) + (\omega^1_p)^2 c^2_q(t) - \sqrt{\frac{M^1_p}{(\omega^2_q)^2 M^2_q}} \frac{W^{12}_{pq}}{\sqrt{(\omega^2_q)^2 M^1_p M^2_q}} \dot{c}^2_q = L^2_{qp}(t)
\end{aligned} \tag{2.17}$$

where L^1_{pq}, L^2_{qp} denote the generalized force and the interactions forces with all the others modes. With Eq. 2.17 and 2.7, the power exchanged between two coupled oscillators analogous to Eq. 2.8 can be obtained for mode p and q as follows

$$\Pi^{12}_{pq} = \beta^{12}_{pq}(E^1_p - E^2_q) \tag{2.18}$$

where β^{12}_{pq} is the intermodal coupling factor deduced from Eq. 2.9. It can be split into the spatial term β^{12}_W (intermodal spatial coupling factor) related to spatial modeshape and the spectral term β^{12}_ω (intermodal spectral coupling factor) related to subsystem resonance:

$$\beta^{12}_{pq} = \beta^{12}_W \times \beta^{12}_\omega \tag{2.19}$$

where

$$\beta^{12}_W = \frac{(W^{12}_{pq})^2}{M^1_p M^2_q}, \tag{2.20}$$

$$\beta^{12}_\omega = \frac{\eta^1_p \omega^1_p (\omega^2_q)^2 + \eta^2_q \omega^2_q (\omega^1_p)^2}{((\omega^1_p)^2 - (\omega^2_q)^2)^2 + (\eta^1_p \omega^1_p + \eta^2_q \omega^2_q)(\eta^1_p \omega^1_p (\omega^2_q)^2 + \eta^2_q \omega^2_q (\omega^2_q)^2)} \tag{2.21}$$

Finally, the energy balance equation for mode p of subsystem 1 and mode q of subsystem 2 can be formulated by substituting Eq. 2.16 and 2.18 into Eq. 2.14 as follows

$$\Pi^1_{p,inj} = \omega^1_p \eta^1_p E^1_p + \sum_{q=1}^{N_2} \beta^{12}_{pq}(E^1_p - E^2_q) \qquad \forall p \in [1, ..., N_1],$$
$$\Pi^2_{q,inj} = \omega^2_q \eta^2_q E^2_q + \sum_{p=1}^{N_1} \beta^{12}_{pq}(E^2_q - E^1_p) \qquad \forall q \in [1, ..., N_2] \tag{2.22}$$

By solving theses equations, modal energies can be determined. Subsequently, the total subsystem energies E^1, E^2 are obtained by adding all modal energies within the frequency band as follows

$$E^1 = \sum_{p=1}^{N_1} E^1_p, \quad E^2 = \sum_{q=1}^{N_2} E^2_q \tag{2.23}$$

Considering average modal energy in a given frequency band Δf i.e. the equipartition relation, $E^1_p = \frac{E^1}{N_1}, E^2_q = \frac{E^2}{N_2}$, the SEA ensemble power balance can be obtained from Eq. 2.22 and the CLF can be deduced as follows,

$$\eta_{12} = \frac{1}{N_1 \omega_c} \sum_{p=1}^{N_1} \sum_{q=1}^{N_2} \beta^{12}_{pq},$$
$$\eta_{21} = \frac{1}{N_2 \omega_c} \sum_{p=1}^{N_1} \sum_{q=1}^{N_2} \beta^{12}_{pq} \tag{2.24}$$

where η_{12} is the CLFs from subsystem 1 to subsystem 2.

The SmEdA modal approach gives an advantage over the SEA analysis since a system with the low modal overlap driven by a localized excitation is not problematic. The other advantage is that the method can be easily implemented for systems of heterogeneous subsystems and of complicated geometry since uncoupled subsystem modal information can be extracted by the use of standard FE codes.

2.2.4 Plate-cavity problem

A rectangular plate coupled to a parallelepipedic acoustic cavity is considered. The plate is considered stiff while the cavity is soft. In accordance with the DMF formulation, the coupling surface can be then characterized with free plate displacement mode (subsystem 1) and blocked cavity pressure mode (subsystem 2) as illustrated in Fig. 2.5. Note that the subsystem subscripts are 1 for plate with mode p and 2 for cavity with mode q, and such notations will be consistent throughout this thesis. The intermodal work W^{12}_{pq} over the coupling surface S is given by

$$W^{12}_{pq} = \int_s \Phi^1_p P^2_q dS \tag{2.25}$$

where Φ^1_p, P^2_q are displacement modeshape p of the plate and pressure modeshape q of the cavity respectively. Note that the modal masses are normalized to a unit value as $M^1_p = M^2_q = 1$. Computations

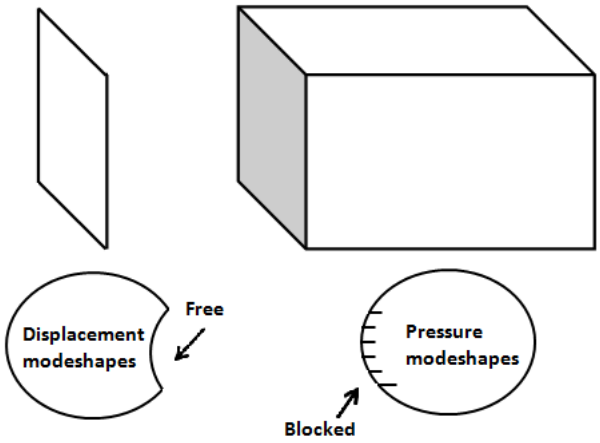

Figure 2.5: A rectangular plate coupled to an acoustic cavity via coupling surface (grey area). Subsystem descriptions with their boundary conditions in SmEdA model.

of the intermodal coupling factors ($\beta_{\omega}^{12}, \beta_{W}^{12}$) are performed with the modal information of the uncoupled subsystem ($\omega_p^1, \Phi_p^1, \omega_q^2, P_q^2$) that can be easily extracted from standard FE codes.

The plate is a 1 mm steel with dimensions of 0.5×0.6 (m^2). Young's modulus, density and Poisson's ratio are 2.03 GPa, 7523.1 kg/m^3 and 0.33 respectively. The plate is clamped at its boundaries. Cavity dimensions are $0.5 \times 0.6 \times 0.7$ (m^3) and all surfaces are rigid. Undamped modeshapes and resonant frequencies of the plate are obtained using *NASTRAN* software modal extraction of the Lanczos method. The mesh size is chosen in order to have a minimum of six elements on the bending wavelength at 8 kHz. The plate is modeled with 13,776 of shell elements. Note that the cavity modal information has analytically calculated.

2.2.4.1 Modal overlap

The modal overlaps of each subsystem are presented in Fig. 2.7. The modal overlap is given by $M(\omega) = \omega\eta n(\omega)$ where $n(\omega)$ is the modal density. Subsystem modal densities are computed with resonant modes obtained from a FE computation of uncoupled plate and from an analytical computation of uncoupled cavity i.e. $n(\omega) \approx \frac{N}{\Delta\omega}$ where N is a number of resonant modes and $\Delta\omega$ is a frequency bandwidth. The number of subsystem resonant modes (N) in 1/3 octave band is presented in Table 2.1.

1/3 octave (Hz)	315	400	500	630	800	1k	1.25k	1.6k
Plate	6	7	10	11	16	19	24	35
Cavity	2	3	2	8	14	21	21	90
	2k	2.5k	3.15k	4k	5k	6.3k	8k	
	41	50	69	87	106	144	185	
	151	282	567	1154	2096	4227	8754	

Table 2.1: Number of subsystem resonant modes in 1/3 octave band

The subsystem damping loss factors η_1, η_2 have been experimentally estimated by the high-resolution modal analysis method proposed by Ege et al [36] which will be discussed in Chapter 5. Frequency-band

averaged global values shown in Fig. 2.6 (averaged over modal values of selected resonant modes) are considered for 1/3 octave band analysis. Note that the SmEdA computation performed on the plate-cavity

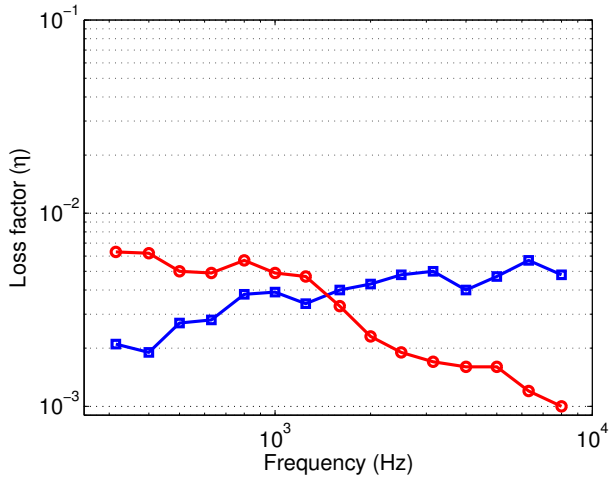

Figure 2.6: Experimentally estimated subsystem damping loss factor (□: plate, ◯: cavity)

system in this chapter are done with such averaged experimental values since no modal damping loss factors of a steel plate and an acoustic cavity are available by numerical means.

The modal overlap of the mid-frequency domain is said to be between 30 % and 100 % [36]. Presented in Fig. 2.7, the mid-frequency domain in this case is from 1 kHz to 2 kHz for the plate and from 800 Hz to

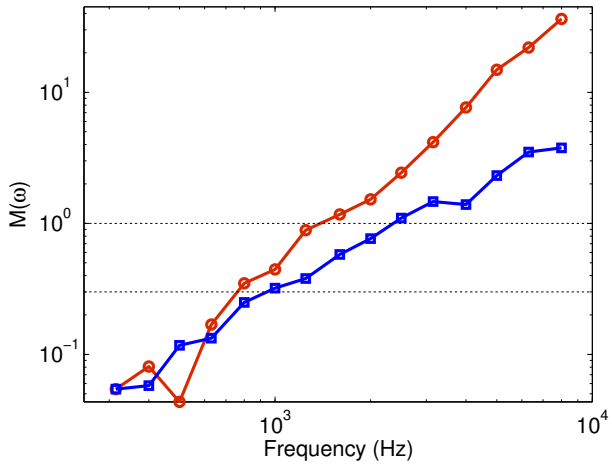

Figure 2.7: The subsystem modal overlap factor in 1/3 octave band (□: plate, ◯: cavity). Dotted lines indicate a range of the mid-frequency ($30\ \% < M < 100\ \%$)

1.25 kHz for the cavity.

2.2.4.2 Injected power

The power is injected by the stationary white noise force applied at coordinate $(x, y) = (0.2, 0.2)$ (m). Analogous to Eq. 2.14, the injected power into the plate mode p is given by

$$\Pi^1_{p,inj} = \frac{\pi S_F}{M^1_p}(\Phi^1_p)^2(x, y) \tag{2.26}$$

where $\Phi^1_p(x, y)$ is the modeshape of the plate mode p at point (x, y), and S_F is the power spectral density (W/Hz). The "rain on the roof" excitation is implicated in the SEA formulation which produces the energy equipartition for a source subsystem [62]. However, it is often very difficult to apply multiple excitations and obtain the injected powers in many practical situations where the excitation could be localized. The injected power obtained with Eq. 2.26 is plotted for frequency bands centered at 1 kHz and at 3.15 kHz. It

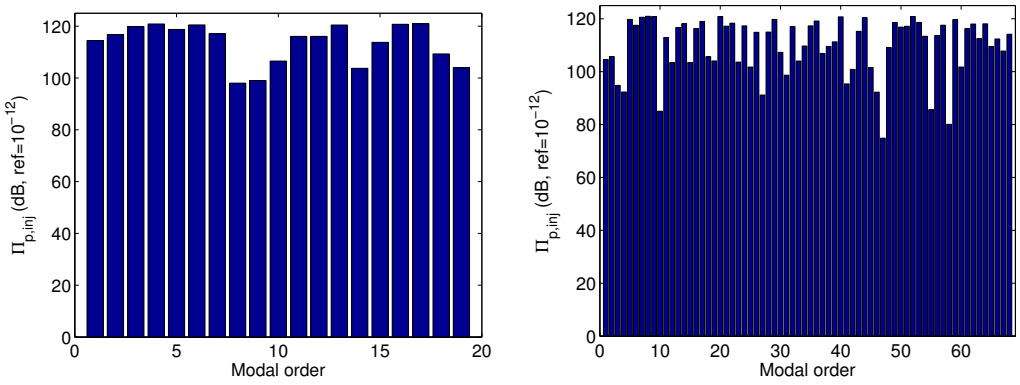

(a) (b)

Figure 2.8: Modal injected power ($\Pi^1_{p,inj}$): (a) 1 kHz band, (b) 3.15 kHz band

can be seen in both frequency bands that the injected power strongly varies among resonant modes where maximum differences between two modes are 23 dB in 1 kHz band and 47 dB in 3.15 kHz band. Such disproportionate modal power distribution does not occur with the "rain on the roof" excitation.

2.2.4.3 Modal coupling factor

Fig. 2.9 shows the intermodal spatial β^{12}_W and spectral β^{12}_ω coupling factors as a function of coupled resonant modes between two subsystems in 1 kHz and 3.15 kHz bands. The intermodal spectral coupling factor β^{12}_ω becomes stronger as a difference between two subsystem resonant frequencies approaches zero ($\omega^1_p \approx \omega^2_q$, see Eq. 2.21). This is seen in both frequency bands as subsystem modes are classified with increasing natural frequencies. On the other hand, the intermodal spatial coupling factor β^{12}_W is seen to vary distinctly among mode couples due to subsystem modeshapes. It indicates the spatial coincidence of the mode couple.

Fig. 2.10 shows the intermodal coupling factor β^{12}_{pq} in 1 kHz and 3.15 kHz bands. In 1 kHz band, energy is mostly exchanged through two pairs of mode couples. In other words, no energy equipartition is respected despite a sufficient number of modes in both subsystems (see Table 2.1) that can be qualified as SEA subsystems. The dominant mode couple in this frequency band is composed of the 4th plate mode

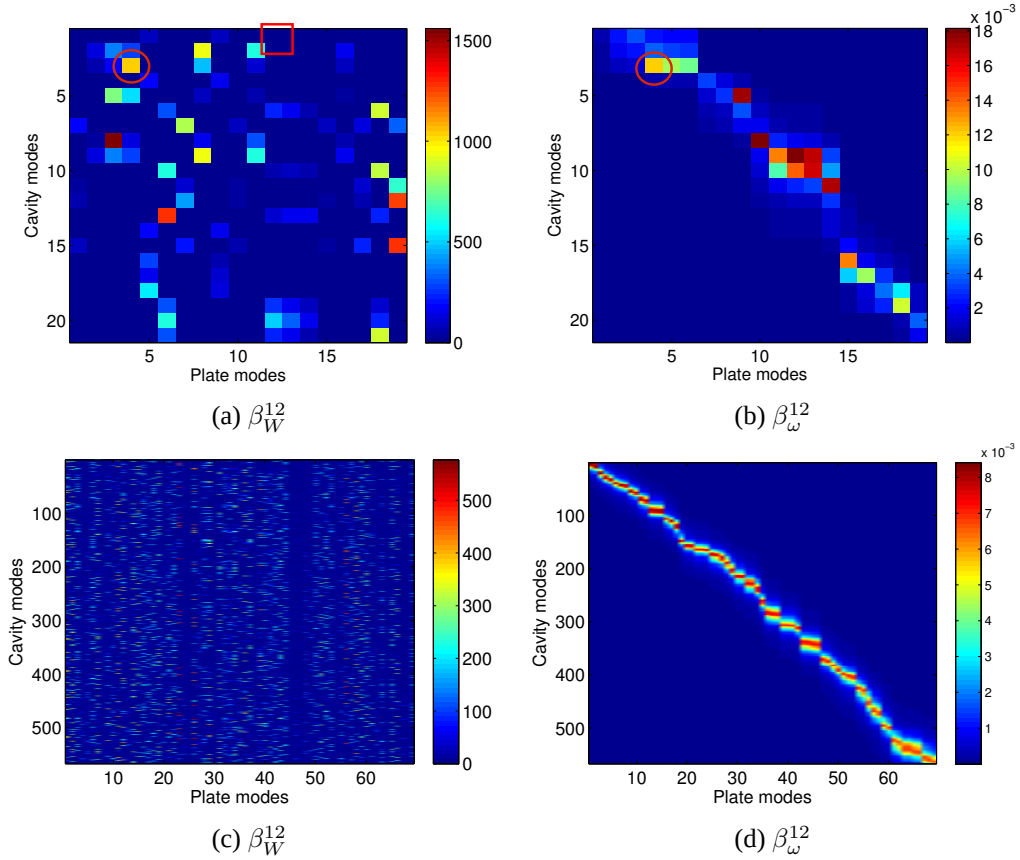

(a) β_W^{12} (b) β_ω^{12}

(c) β_W^{12} (d) β_ω^{12}

Figure 2.9: The intermodal spatial (β_W^{12}) and spectral (β_ω^{12}) coupling factors versus coupled resonant modes: (Top) 1 kHz band, (Bottom) 3.15 kHz band

and the 3rd cavity mode. This is a product of spatially and spectrally strong couplings marked in circle in Fig. 2.9a and 2.9b. The spatial coupling has an amplifying effect on some spectrally coupled modes while reducing the coupling strength of others. As a result, β_{pq}^{12} varies disproportionately among mode couples. In 3.15 kHz band, on the other hand, more mode couples participate in energy exchange. All plate modes

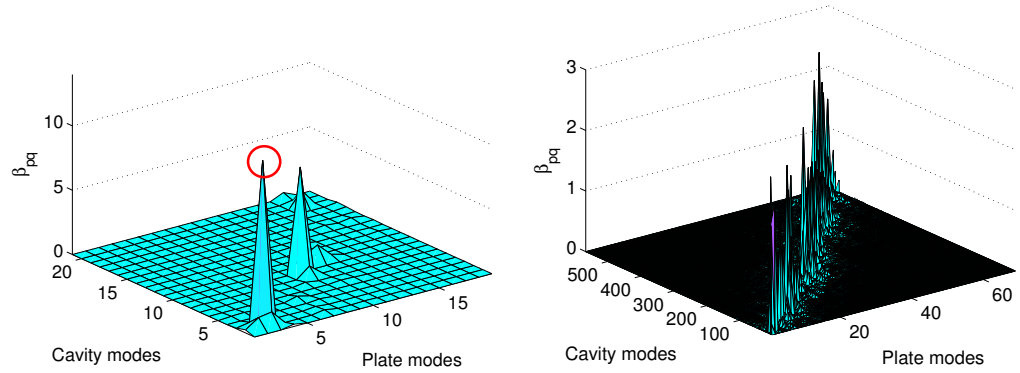

(a) (b)

Figure 2.10: The intermodal coupling factors (β_{pq}^{12}) versus coupled resonant modes (Modes indexed with increasing natural frequencies): (a) 1 kHz band, (b) 3.15 kHz band

are coupled to at least one cavity mode, approaching near equipartition as it can be observed in Fig. 2.12c and 2.12d.

In 1 kHz band, the energy exchange is dominated by the mode couple between the plate mode at 926 Hz and the cavity mode at 922 Hz (the mode couple marked in circle in Fig. 2.9a, 2.9b and 2.10a). Fig. 2.11a and 2.11b show subsystem modeshapes at the coupling surfaces for these two resonant modes. It is clearly seen that both subsystems have axial modes with the same wavelength in x direction approaching near spatial coincidence. Both spectral and spatial coincidences of two subsystem modes have resulted in the strongest coupling in the frequency band. On the other hand, the mode couple composed of the 12th plate mode and the 1st cavity mode is the weakest in terms of the spatial coupling (mode couple marked in rectangle in Fig. 2.9a). As seen in Fig. 2.11c and 2.11d, subsystem modeshapes show no spatial coincidence.

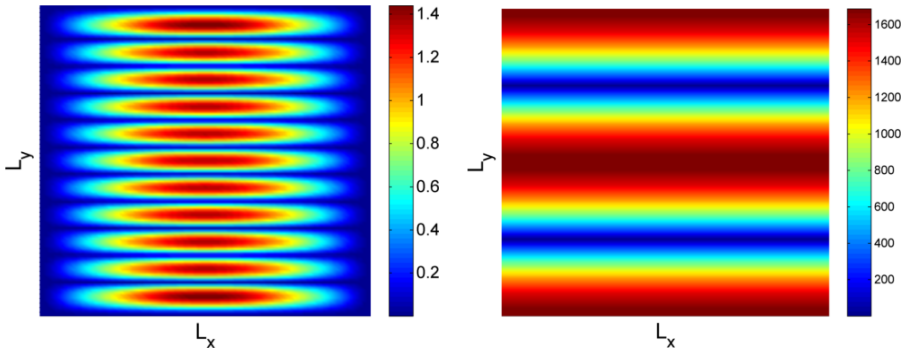

(a) Plate at 926 Hz (b) Cavity at 922 Hz

(c) Plate at 1009 Hz (d) Cavity at 915 Hz

Figure 2.11: Subsystem modeshapes at the coupling surface in 1 kHz band: (Top) Mode couple (3,8) (high β_W^{12} and β_ω^{12} marked in circles in Fig. 2.9a and 2.9b respectively, and the highest β_{pq}^{12} marked in circle in Fig. 2.10a), (Bottom) Mode couple (12,1) (the lowest β_W^{12} marked in rectangle in Fig. 2.9a)

2.2.4.4 Subsystem modal energy

Fig. 2.12 shows subsystem modal energies in 1 kHz and 3.15 kHz bands. Modal energies are obtained by solving Eq. 2.21. It is clearly seen that energy is disproportionately distributed among resonant modes. This comes from the fact that the injected power varies from one mode to another (see Fig. 2.8), which leads to a variation of modal energy in the excited plate. Such effect is amplified for the cavity by the filtering effect of the junction i.e. the variation of the modal coupling factors from one mode to another [61].

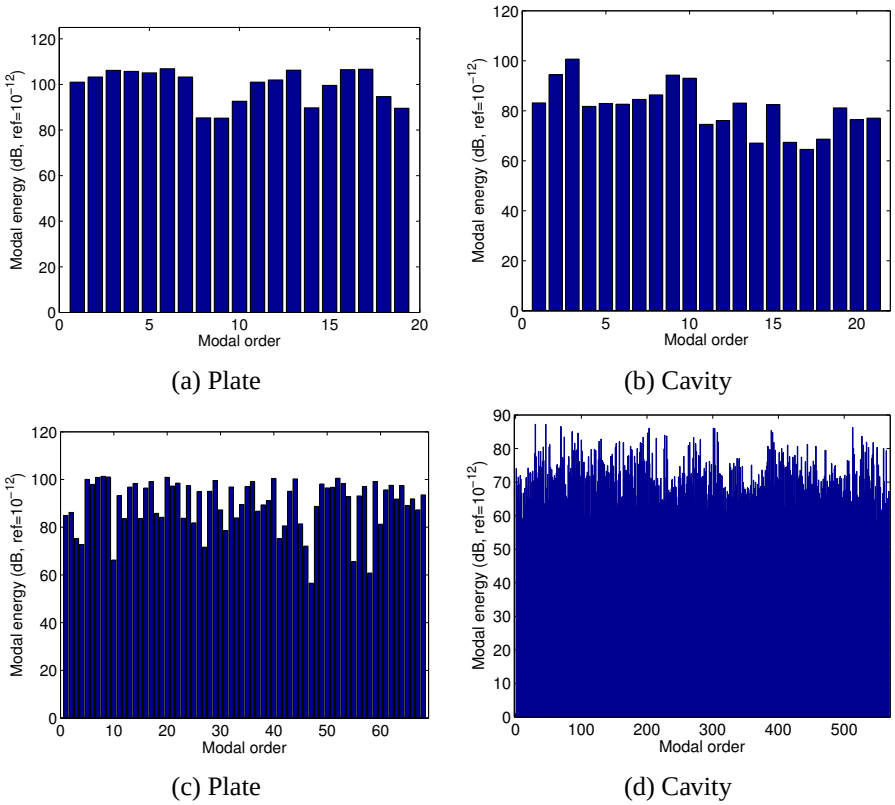

(a) Plate (b) Cavity

(c) Plate (d) Cavity

Figure 2.12: Subsystem modal energy distribution (Modes indexed with increasing natural frequencies): (Top) 1 kHz band, (Bottom) 3.15 kHz band

2.2.4.5 Influence of the boundary condition on the energy transmission

Fig. 2.13 plots subsystem energy ratios (E_{cavity}/E_{plate}) for cases of the simply supported plate (analytically computed) coupled to cavity and the clamped plate (numerically computed) coupled to cavity. Note that subsystem subscripts are 1 for the plate and 2 for the cavity and will be consistent throughout this thesis. At low frequencies, boundary conditions have generally a strong impact on resonant frequencies while the modal density at high frequencies is less influenced. This can be seen below 1 kHz that two cases

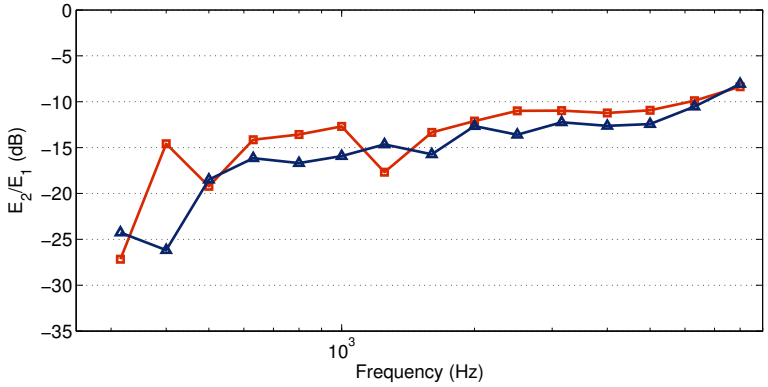

Figure 2.13: Subsystem energy ratio (□: clamped plate-cavity, △: simply supported plate-cavity)

are apparently different whereases the difference decreases with frequency since two plates have a similar

number of modes.

2.2.4.6 Influence of the damping on the energy transmission

The main interest of this Ph.D research is to study the effect of the damping within the coupled system. How the damping in each subsystem influences subsystem energies is of interest. Fig. 2.14 shows a change of the subsystem energy ratio for a clamped plate-cavity system with respect to the subsystem damping loss factor. By monotonically increasing the damping in one subsystem while maintaining it constant in

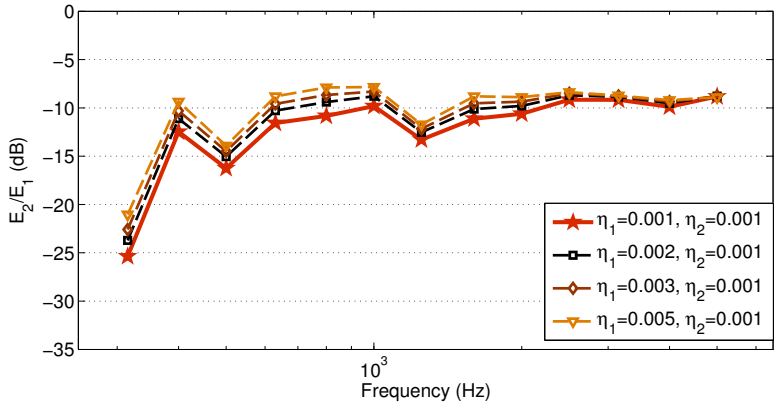

(a)

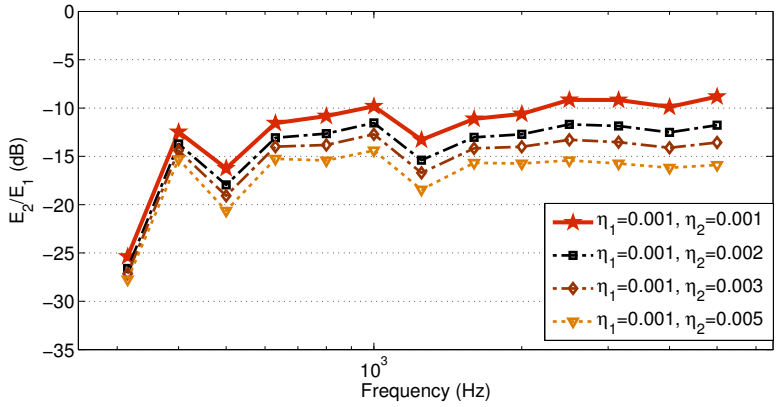

(b)

Figure 2.14: Subsystem energy ratio of the clamped plate-cavity in 1/3 octave band with respect to the subsystem damping (Constant damping loss factor for all frequency bands): (a) Increase of the plate damping, (b) Increase of the cavity damping

the other, its influence on the subsystem energy ratio can be observed. Note that given damping levels are a constant value for all frequency bands and are arbitrarily chosen. Up to 800 Hz, both subsystem dampings are seen to influence the ratio. As the plate damping increases, plate energies diminish, resulting an increase of the ratio curve. By contrary, an increase of the cavity damping lowers the ratio compared to the reference curve (of $\eta_1 = \eta_2 = 0.001$). Above 1 kHz, increasing the plate damping is seen to have decreasing impact whereas the ratio curve has substantially dropped as the cavity damping is increased. In other word, the energy ratio is seen far more responsive to the cavity damping than the plate damping, and such phenomenon has become more prominent with increasing frequencies.

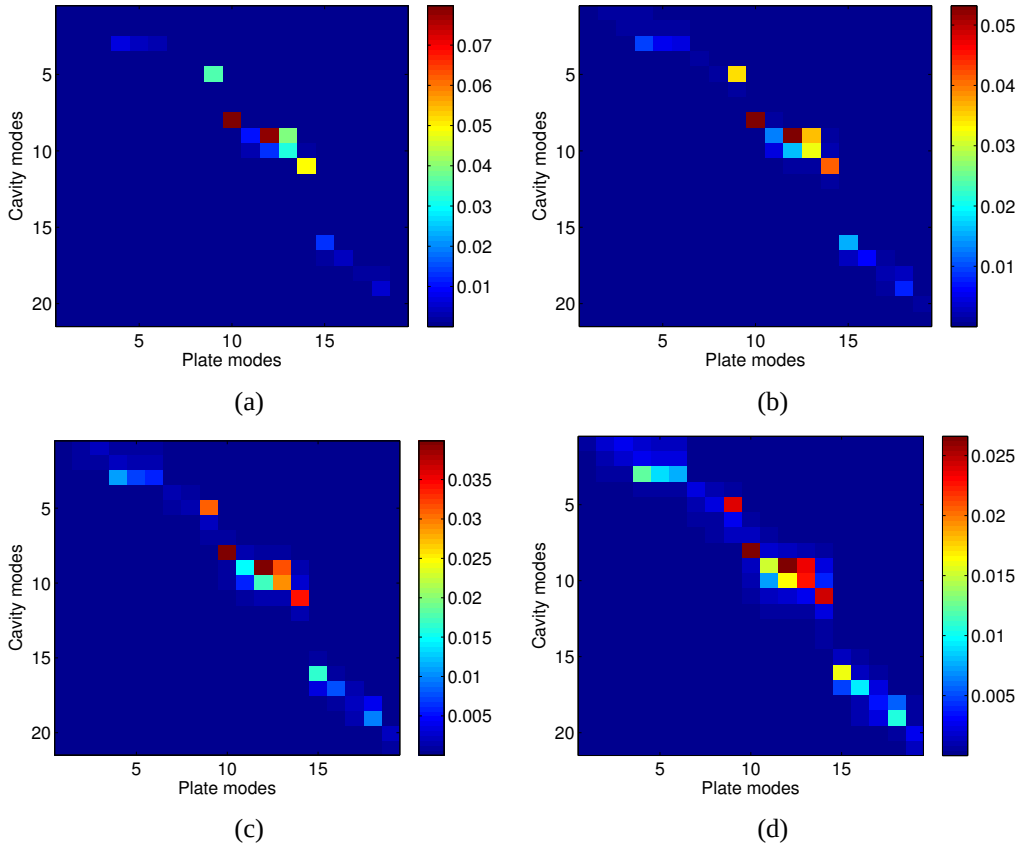

Figure 2.15: The intermodal spectral (β_{ω}^{12}) coupling factors versus coupled resonant modes with respect to the plate damping: (a) $\eta_1 = 0.001$, $\eta_2 = 0.001$, (b) $\eta_1 = 0.002$, $\eta_2 = 0.001$, (c) $\eta_1 = 0.003$, $\eta_2 = 0.001$, (c) $\eta_1 = 0.005$, $\eta_2 = 0.001$

Fig. 2.15 shows the influence of the plate damping on the intermodal spectral coupling factor β_{ω}^{12}. While the damping loss factor has no direct impact on the spatial coupling β_{W}^{12} (see Eq. 2.20), the spectral coupling factor is seen to have clear influence (see Eq. 2.21): the higher the damping is, the more mode couples participate in energy exchange. On the other hand, the coupling strength (amplitude) has decreased as the damping increases.

2.3 Conclusion

For vibracoustic analysis of a coupled system, the SEA method is commonly used. However, the ensemble energy analysis is only relevant to systems with the high modal density and is known to result in gross overestimations of modal energy levels in case of systems with low modal overlap (low modal density in most case). Such problem can be resolved by the SmEdA method where the energy exchange is deduced from the subsystem modal coupling. Since the subsystem coupling is deduced only from the knowledge of uncoupled subsystem modes, the use of the FEM facilitates industrial applications. The method can be also easily related to the classical SEA power balance formulation as well as the CLF.

For a plate-cavity problem, the SmEdA analysis has demonstrated that the energy equipartition does not occur in the low frequency domain. At low modal overlap, subsystem energies are exchanged through

a few number of dominant mode couples where spatial and spectral coincidences have occurred. Modal energy disparities have occurred largely due to the frequency coincidence and this can be accentuated by the spatial coupling. In the mid-frequency domain, more resonant modes are coupled to exchange energy, achieving near modal energy equipartition.

It has shown that boundary conditions have a minor impact on subsystem energy transfer and this is due the similar modal densities between two cases (simply supported and clamped boundaries). The subsystem energy ratio has been shown highly dependent on the damping of a receiving subsystem. The effect of increasing the damping of a source subsystem has diminished with increasing frequency while increasing the receiving subsystem damping has shown otherwise. This is due to the fact that the treatment on the plate has reduced both subsystem energies simultaneously whereases increasing the cavity damping only affects the cavity energies. It has been also seen that increasing subsystem damping leads to more mode couples while decreases the strength of each mode couple.

In this chapter, a plate-cavity problem with no additive damping has been analyzed. The objective of this research is to extend the SmEdA method to include the damping effect introduced by dissipative materials into the system. In following chapter, therefore, numerical techniques to model the plate treated with viscoelastic damping materials and the cavity treated with porous materials are presented.

CHAPTER 3

Modeling Techniques of Dissipative Material

The methodology to introduce dissipative materials into the SmEdA method is presented in this chapter. It is based on three steps:

1. Dissipative materials are represented by simplified equivalent models. The equivalent single layer model will be presented in Section 3.1 for describing the plate covered with a viscoelastic layer. The equivalent fluid model will be considered in Section 3.2 for describing porous materials in the cavity.

2. Each subsystem including the equivalent models of the dissipative materials is modeled with FEM. The FE matrices including the energy dissipation are then computed. The Modal Strain Energy and Modal Strain Kinetic Energy methods presented in Section 3.3.1 and 3.3.2 respectively are used to estimate the modal damping loss factor of each subsystem mode.

3. The SmEdA calculation is performed considering the modal damping loss factor estimated in the second step. (This step is not presented in this chapter: SmEdA calculation results will be presented in next chapter.)

3.1 Equivalent single layer modeling for viscoelastic materials

3.1.1 Methodology

A method to simplify a plate consisting of layers of isotropic damping materials is considered. The equivalent single layer model [42] defines a single layer that has the same transverse displacement of multi-layers by using equivalent viscoelastic modulus in the standard thin plate equation (Love-Kirchhoff thin plate

theory). It describes the plate motion with the displacement of the first layer by assuming the displacement field of each layer identical. This can drastically reduce computational resources compared to a three-dimensional thick plate model (Reissner-Mindlin's model).

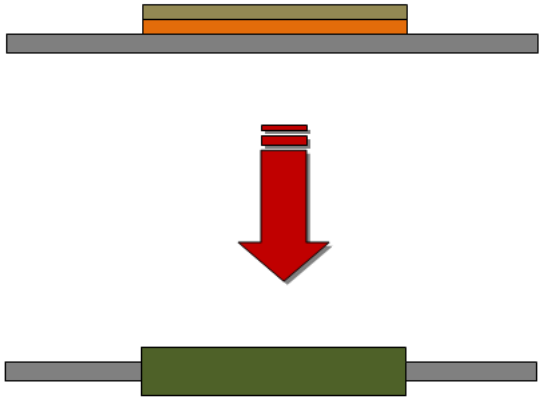

Figure 3.1: Schematic of equivalent single layer modeling

The equivalent plate model considers bending, membrane, shear and rotational motions at each layer. Then the continuity conditions on displacements and shear effects at each layer interface are used to give an equation of motion of the entire multi-layered plate field expressed in the function of the first layer field [42]. The equation of global motion of a multi-layered plate under free vibration is then given by

$$-\omega^2(\mathfrak{T})\begin{Bmatrix} W \\ \psi_x^1 \\ \psi_y^1 \\ \phi_x^1 \\ \phi_y^1 \end{Bmatrix} + (\mathfrak{V})\begin{Bmatrix} W \\ \psi_x^1 \\ \psi_y^1 \\ \phi_x^1 \\ \phi_y^1 \end{Bmatrix} = \{0\} \tag{3.1}$$

$W, \psi_x^1, \psi_y^1, \phi_x^1, \phi_y^1$ are respectively independent functions defining transverse displacement, membrane displacement and shear rotation of the first layer along x and y directions. The derivation of these equations is given in full detail in the original publication [42].

A particular solution of Eq. 3.1 is a plane traveling wave as follows

$$\begin{Bmatrix} W \\ \psi_x^1 \\ \psi_y^1 \\ \phi_x^1 \\ \phi_y^1 \end{Bmatrix} = \begin{Bmatrix} \bar{W} \\ \bar{\psi^1}_x \\ \bar{\psi^1}_y \\ \bar{\phi^1}_x \\ \bar{\phi^1}_y \end{Bmatrix} e^{jk_x x} \tag{3.2}$$

where the overline $(-)$ indicates an amplitude of each wave function. The wave propagation in x direction can represent the plate motion in this approach since an isotropic material is considered i.e. all directions of the wave propagation are equivalent [41]. When introducing the solution Eq. 3.2 into Eq 3.1, two decoupled problems are obtained: (1) the transverse motion coupled with membrane and shear effect in x direction

and (2) the in-plane motion in y direction.

Since an acoustic radiation of the plate is due to the transverse motion, only the first problem is considered here. By assuming a small thickness of the multi-layer which neglects the inertia associated with membrane, shear and rotational effects, a simplified equation is obtained (see [42] for the detail):

$$-\omega^2\delta_{13}\bar{W} + \left\{A_1k^4 - \frac{A_2}{A_3k^2 + \omega\sqrt{M_sA_4}}k^6\right\}\bar{W} = 0, \tag{3.3}$$

where $A_1, A_2, A_3, A_4, \delta_{13}$ are coefficients depending on the angular frequency ω and the material properties of each layer i.e. complex Young's modulus, density, Poisson's ratio and thickness. $k = \sqrt{\omega}\left(\frac{M_s}{B}\right)^{\frac{1}{4}}$ is wave number of the free bending wave and M_s is mass per unit area.

On the other hand, the equation of motion expressing the transverse traveling wave of the thin Love-Kirchhoff plate is considered:

$$M_s\frac{\partial^2 W_{LK}}{\partial t^2} + B\left\{\frac{\partial^4 W_{LK}}{\partial x^4} + 2\frac{\partial^4 W_{LK}}{\partial x^2\partial y^2}\frac{\partial^4 W_{LK}}{\partial y^4}\right\} = 0 \tag{3.4}$$

where $B = \frac{Eh^3}{12(1-v^2)}$ is the plate bending stiffness. E, h, v are complex Young's modulus, thickness and Poisson's ratio respectively. The subscript LK indicates the Love-Kirchhoff plate. A transverse plane wave traveling in x direction, $W_{LK} = \bar{W}_{LK}e^{jkx}e^{j\omega t}$, then must satisfy

$$-\omega^2 M_s\bar{W}_{LK} + Bk^4\bar{W}_{LK} = 0 \tag{3.5}$$

In order to formulate the equivalence between $\bar{W}$ and $\bar{W}_{LK}$, Eq. 3.3 is compared with Eq. 3.5. This gives

$$M_s = \delta_{13}, \tag{3.6}$$

$$B = A_1 - \frac{A_2^2}{A_3k^2 + \omega\sqrt{M_sA_4}}k^2 \tag{3.7}$$

When substituting the frequency dependent wave number k into Eq. 3.7, a polynomial equation is obtained as follows

$$A_4B^{\frac{3}{2}} + A_3B - A_1A_4B^{\frac{1}{2}} - A_1A_3 + A_2 = 0 \tag{3.8}$$

This equation of the variable B has three roots. One of them can be associated to the dominant transverse motion that can give the bending stiffness of the equivalent layer [41]. Finally, the parameters of equivalent layer ($\rho_{eq}, v_{eq}, E_{eq}$) can be determined from mechanical properties of each layer:

$$\begin{aligned}\rho_{eq} &= \frac{\sum h_i\rho_i}{\sum h_i},\\ v_{eq} &= \frac{\sum h_iv_i}{\sum h_i},\\ E_{eq} &= \frac{12(1-v_{eq}^2)B}{h_t^3}\end{aligned} \tag{3.9}$$

where h_t is total thickness of the composite panel, and the subscripts eq and i indicate equivalent and i^{th} layer. The equivalent material loss factor η_{eq} can be determined from the computed complex Young's modulus E_{eq}. Both quantities vary with vibration frequency, which will be discussed in next section.

Note that the equivalent values of Poisson's ratio and density are approximated as averaged values over a thickness of the composite panel.

3.1.2 Frequency dependency of the viscoelastic material

It is well known that viscoelastic materials have mechanical characteristics such as Young's modulus and damping loss factor that vary with frequency. Elastic Young's modulus of a given material can be computed using the time-temperature superposition principle of which master modulus curve as a function of time is determined with the empirical Williams-Landel-Ferry (WLF) model [87]. Complex shear modulus is given by

$$\begin{aligned} Re\{G(f)\} =& 10^{\sum_{n=0}^{N} A_n Log(\alpha_T f)^n}, \\ Im\{G(f)\} =& 10^{\sum_{n=0}^{N} B_n Log(\alpha_T f)^n}, \\ \alpha_T =& 10^{\frac{-c_1(T-T_{ref})}{c_2+T-T_{ref}}} \end{aligned} \tag{3.10}$$

where A_n, B_n are polynomial coefficients, c_1, c_2 are empirical constants and T, T_{ref} are temperature chosen and reference temperature respectively. The values (A_n, B_n, c_1, c_2) of a given material need to be experimentally determined for a wide range of frequencies at several temperatures. Subsequently, Young's modulus and the damping loss factor can be given by

$$E(f) = 2G(f)(1+v) \tag{3.11}$$

$$\eta(f) = \frac{Im\{G(f)\}}{Re\{G(f)\}} \tag{3.12}$$

3.1.3 Model example

In order to verify the equivalent single layer model, the damped plates studied in the publication [71] are considered. A square aluminum plate is treated with a PVC (polyvinyl chloride) patch. Equivalent parameters of the composite material $(E_{eq}(f), \rho_{eq}, v_{eq}, \eta_{eq}(f))$ are computed. The computation are performed using *MOVISAND* software that was developed at LVA by Guyader and Cacciolati [41]. Material properties of the example models are given in Table 3.1. Note that all properties are taken from the publication [71] where constant values are assigned to PVC regardless of its thickness i.e. no WLF model is applied. *MOVISAND* computations are performed for a frequency range from 1 Hz to 2000 Hz. Note that *MOVISAND* computation results are infinite plate parameters. Fig. 3.2 shows the variations of Young's modulus and damping factors with respect to vibration frequency. It can be seen that neither quantity varies significantly.

Once equivalent parameters are determined, dynamic analyses of a finite plate can be easily performed in standard FE codes. A schematic of the finite plate modeling is illustrated in Fig. 3.3. The equivalent plate method is tested with three different arrangements of a PVC layer (one full coverage and two partial coverages, namely configuration 8 and 10) and is evaluated by comparing the frequency response with the

	Aluminum	PVC	Equivalent	Equivalent
Thickness (mm)	1	3 & 3.6	4	4.6
E (Pa)	7.1e10	2.4e7	$E_{eq}(f)$	$E_{eq}(f)$
$\rho(\mathrm{kg/m^2})$	2700	1200	1575	1526
υ	0.33	0.45	0.42	0.42
η	0.02	0.35	$\eta_{eq}(f)$	$\eta_{eq}(f)$

Table 3.1: Mechanical properties of aluminum, PVC and equivalent plate estimated using *MOVISAND* software

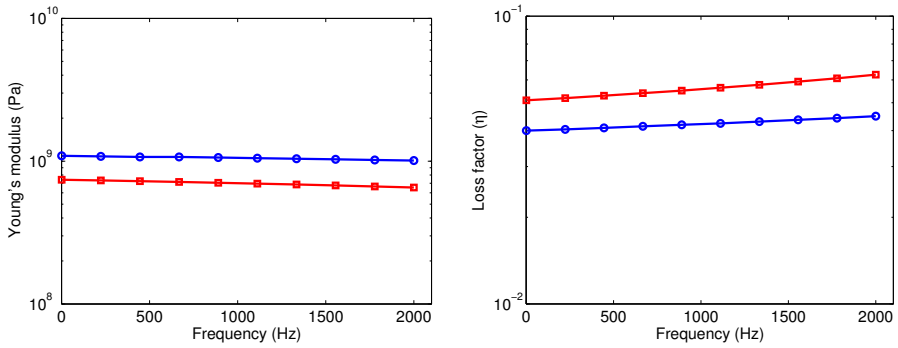

(a) (b)

Figure 3.2: Equivalent parameters in a constant frequency band (Δf=222 Hz) for the aluminum-PVC composite panel estimated using *MOVISAND* software (◯: aluminum + PVC 3 mm, □: aluminum + PVC 3.6 mm): (a) Young's modulus, (b) Material loss factor

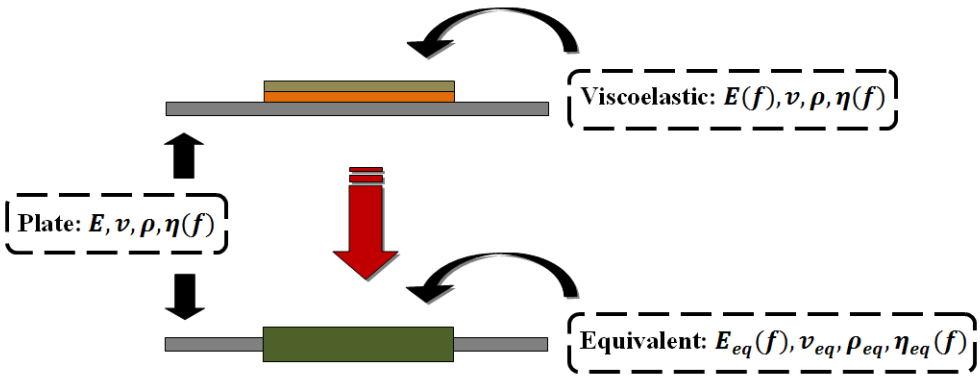

Figure 3.3: Schematics of FE models of the multi-layered plate and the equivalent single layer plate

double layer models. The base plate is 1 mm aluminum and its dimensions are 0.2×0.2 (m). Thicknesses of the PVC layers are 3 mm for the full coverage and 3.6 mm for the partial coverage. Three FE mesh models are shown in Fig. 3.4 with the indication of the surface coverage by PVC with respect to the effective plate area. The double layer plates are modeled with a tied contact (deformable contact) at mid-surfaces between the base plate and the PVC layer using shell elements. For the equivalent plates, the composite part (the base plate + the PVC layer) is characterized with frequency dependent equivalent parameters given in Table 3.1 and Fig. 3.3, and the remaining area is the aluminum plate whose parameters are also given in Table 3.1.

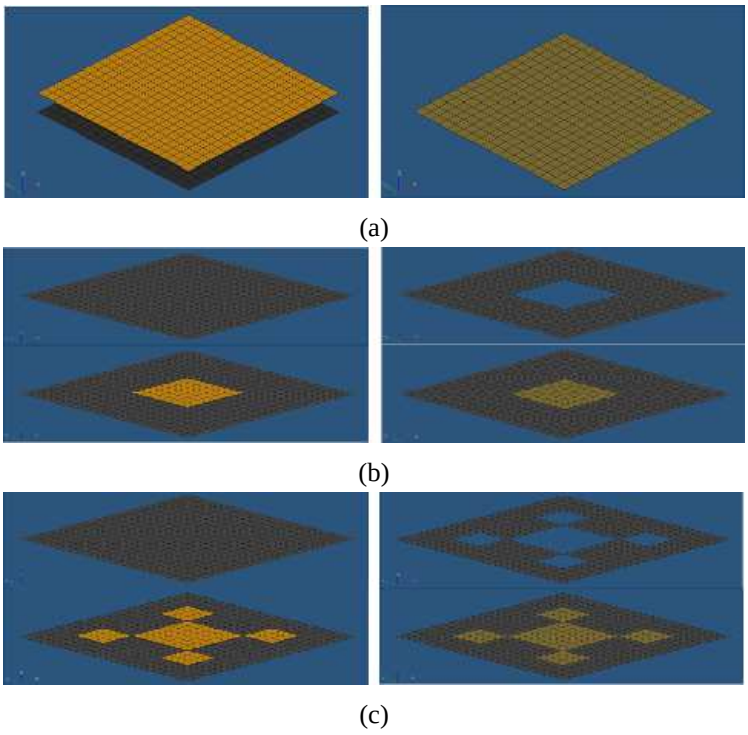

Figure 3.4: FE mesh models of the aluminum plates treated with PVC layers (Left: double layer models, Right: equivalent models): (a) Full coverage (3 mm, 100 %), (b) Patch configuration 8 (3.6 mm, 11 %), (c) Patch configuration 10 (3.6 mm, 22 %)

PVC arrangement	Method	η_1	η_2
Full coverage	Reference (experimental)	0.047	0.04
	Equivalent layer	0.069	0.069
	Double layer	0.067	0.065
Configuration 8	Reference (experimental)	0.036	0.024
	Equivalent layer	0.049	0.049
	Double layer	0.049	0.041
Configuration 10	Reference (experimental)	0.033	0.028
	Equivalent layer	0.052	0.051
	Double layer	0.049	0.052

Table 3.2: The modal damping loss factor of the aluminum-PVC plate models. The values are estimated with the half-power bandwidth method.

Since Young's modulus and loss factors of the equivalent plate shown in Fig. 3.3 do not vary significantly, constant values of the equivalent parameters ($E_{eq} = 1.09\ GPa$, $\eta_{eq} = 0.04$ for 4 mm, and $E_{eq} = 0.741\ GPa$, $\eta_{eq} = 0.051$ for 4.6 mm) are considered for the composite cores. All three models are clamped at the boundaries. A harmonic transverse point force is applied at the same position on each model, and the point response is calculated with *NASTRAN* software.

The frequency responses are compared between double layer models, equivalent models and experimental results from the publication as shown in Fig. 3.5. Note that only first two resonant modes of each model are studied in the publication. The experimental resonant modes are lower than the equivalent modes by about 7 % in average. This discrepancy largely comes from the neglegence of the accelerometer mass

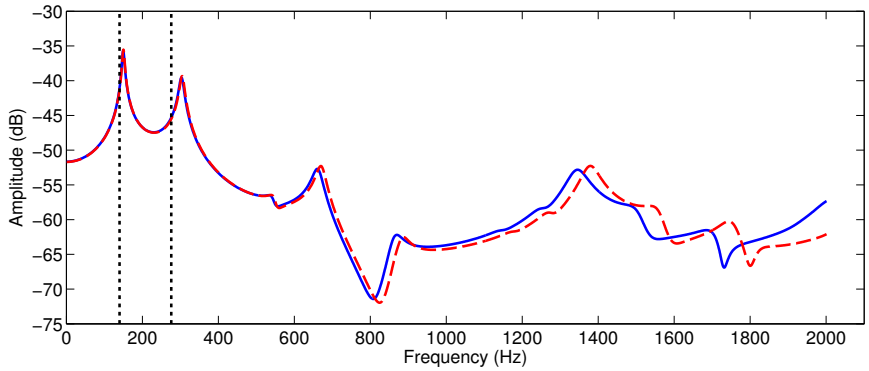

(a)

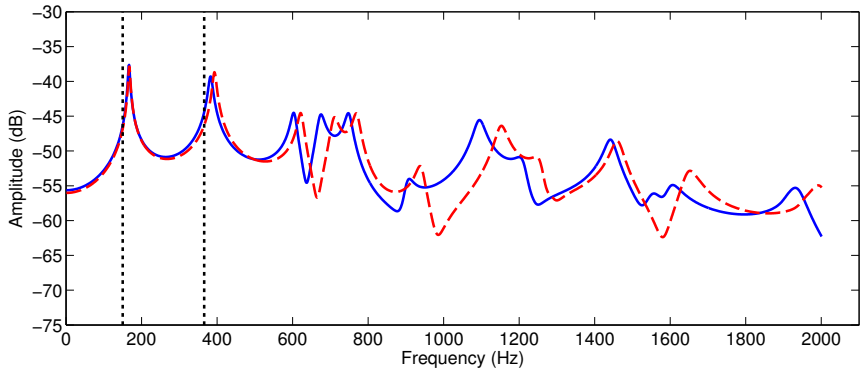

(b)

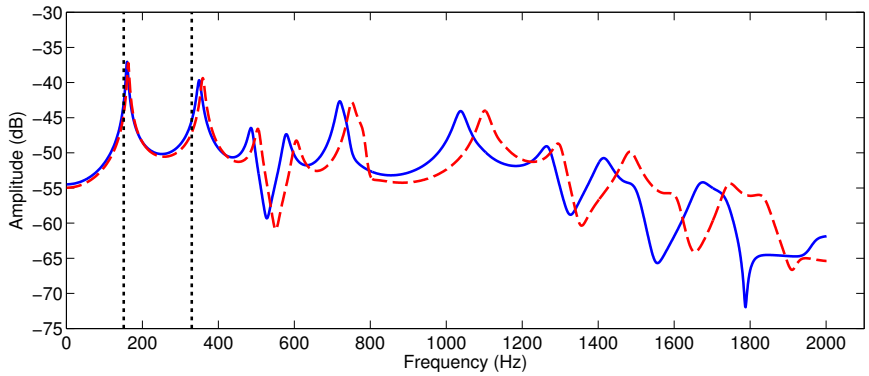

(c)

Figure 3.5: Frequency response (a single point response) of the finite plate models (Solid: equivalent model, Dashed: double layer model, Dotted: experimental resonance from the publication [71]): (a) Full coverage, (b) Patch configuration 8, (c) Patch configuration 10

(8 gm) [71]. The resonant peaks in configuration 8 & 10 appear to be shifted for frequencies above 600 Hz. Nonetheless, the results are overall well comparable for all three models, demonstrating a validity of the equivalent model approach. It should be noted that the computation time spent on the equivalent models are an average four times less than the double layer models. Such advantage becomes more apparent when modeling large-scaled structures.

The modal damping loss factors, estimated with the half-power bandwidth method, are presented for the first two resonant modes in Table 3.2. The equivalent and experimental results differ by 38 % in average,

and both numerical results are always greater than the experimental one.

3.2 Equivalent fluid modeling for poroelastic materials

3.2.1 Methodology

A porous material contains pores that are typically filled with fluid (liquid or gas). A skeleton portion of the material is called a solid frame where a sound wave can travel through. Energy exerted to a porous medium can be transmitted between a solid phase and a fluid phase through elastic, inertial, viscous, and thermal effects. The Biot's model is then expressed from the coupling of equations of motion of two phases. Since the deformable solid phase is implied in the Biot's model, two independent displacement fields exist [18]. The solid phase displacement is represented by $\mathbf{u}^s$ and the fluid phase by $\mathbf{u}^f$. Assuming the harmonic time dependence $e^{j\omega t}$, two equations of each phase motion can be written as

$$\begin{aligned} -\omega^2\tilde{\rho_{11}}\mathbf{u}^s - \omega^2\tilde{\rho}_{12}\mathbf{u}^f =& N \bigtriangledown^2 \mathbf{u}^s + (\tilde{P} - N) \bigtriangledown \bigtriangledown \cdot \mathbf{u}^s + \tilde{Q} \bigtriangledown \bigtriangledown \mathbf{u}^f, \\ -\omega^2\tilde{\rho_{12}}\mathbf{u}^s - \omega^2\tilde{\rho}_{22}\mathbf{u}^f =& \tilde{Q} \bigtriangledown \bigtriangledown \mathbf{u}^s + \tilde{R} \bigtriangledown \bigtriangledown \cdot \mathbf{u}^f \end{aligned} \tag{3.13}$$

where ω is angular frequency and $\tilde{\rho}_{11}$ and $\tilde{\rho}_{22}$ are densities of the frame and fluid phases. $\tilde{\rho}_{12}$ is an interaction between inertial forces of the solid and fluid phases together with viscous dissipation [34]. The tilde ($\sim$) indicates that associated physical properties are complex and frequency dependent. $\tilde{P}, N, \tilde{R}$ are compression modulus, shear modulus of the frame and compression modulus of the fluid respectively. $\tilde{Q} = (1-\phi)\tilde{K}_f$ are elastic coupling modulus between the two phases including thermal effects where ϕ and $\tilde{K}_f$ are porosity and effective compressibility modulus respectively. In this model, three wave motions (one shear and two compression waves) can travel inside porous medium. To solve this problem, a weak integral form is generally considered [10].

If the solid frame is assumed to be rigid when excited by airborne plane waves, it can be modeled as an equivalent fluid. In this case, wave propagation takes place in the fluid phase of the material and the motion of the solid phase is just due to solid-fluid coupling [28]. An equivalent fluid is characterized by a number of bulk properties; impedance, propagation constant, dynamic density and dynamic compressibility. For an equivalent fluid model under the rigid frame assumption $\mathbf{u}^s = 0$, one compression wave propagates and Eq. 3.13 reduce to a single equation of the fluid phase:

$$\tilde{K}_f \bigtriangledown^2 \mathbf{u}^f + \omega^2\tilde{\rho}_{eq}\mathbf{u}^f = 0 \tag{3.14}$$

where $\tilde{\rho}_{eq}$ is equivalent fluid density. The equivalent wave number is given as

$$k_{eq} = \omega\sqrt{\frac{\tilde{\rho}_{eq}}{\tilde{K}_f}} \tag{3.15}$$

Subsequently, the celerity $\tilde{c}_{eq}$ and the characteristic impedance Z_c of the equivalent fluid can be expressed

as a function of density and compressibility given by

$$Z_c = \sqrt{\tilde{K}_f \cdot \tilde{\rho}_{eq}} \tag{3.16}$$

$$\tilde{K}_f = \frac{Z_c \omega}{k_{eq}} \tag{3.17}$$

$$\tilde{c}_{eq} = \sqrt{\frac{\tilde{K}_f}{\tilde{\rho}_{eq}}} \tag{3.18}$$

There are several different equivalent fluid models depending on the expressions of parameters. They normally differ by a number of macroscopic parameters such as flow resistivity, porosity, tortuosity and characteristic length that create bulk properties. Empirical models can give the equivalent density and fluid wavenumber from a few parameters. For example, the Delany-Bazley model [28] depends only on flow resistivity σ and is given by

$$\begin{aligned} Z_c =& \rho_o c_0 \left(1 + 0.0571\, X^{-0.754} - j\, 0.087\, X^{-0.732}\right), \\ k_{eq} =& \frac{\omega}{c_0} \left(1 + 0.09781\, X^{-0.700} - j\, 0.189\, X^{-0.595}\right) \end{aligned} \tag{3.19}$$

where $X = \frac{\rho_o f}{\sigma}$ is a frequency (f) dependent adimensional number that quantifies the relative importance of inertial effects [28]. ρ_o and c_0 are density and celerity of air respectively. Note that this method only corresponds to the treatment backed by rigid cavity walls e.g. not on or in front of the vibrating plate surface. Equivalent parameters can be determined from material properties directly measured with an acoustical experiment.

A major advantage of this approach is that model parameters are easily obtainable with no prior knowledge of macroscopic material properties. The Biot's model parameters require laboratory equipment to be measured following the international standard ISO otherwise are available by manufacturer's aid. In this research, equivalent parameters are directly derived from impedance tube measurements. This is presented in following section.

3.2.2 Two-cavity method

Bulk properties of a porous material such as characteristic impedance Z_c and propagation constant k_{eq} describe the interaction between material and sound wave and are independent of a material thickness and a size. They can be derived from a set of distinctive surface impedance measurements (Kundt tube measurement) known as "Two-cavity method" proposed by Yaniv [90] and Utsuno [85].

A sample layer of homogeneous porous material is placed inside the impedance tube as seen in Fig. 3.6. Z_c and k_{eq} are derived from a pair of surface impedances Z_s and arbitrary impedances Z_a by changing an air depth (d) behind the porous material inside the tube. The acoustic impedance behind the material is considered as a closed-tube impedance that can be obtained theoretically. The acoustic impedance Z_s at a reference surface can be related to the characteristic impedance Z_c and the propagation constant k_{eq} as

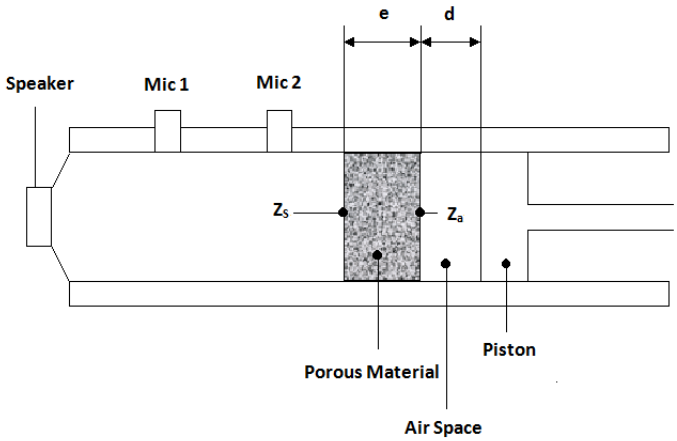

Figure 3.6: Impedance tube measurement of the "Two-cavity method" [85].

follows

$$Z_c = \pm\sqrt{\frac{Z_{a1}Z_{a2}(Z_{s1}-Z_{s2}) - Z_{s1}Z_{s2}(Z_{a1}-Z_{a2})}{(Z_{s1}-Z_{s2}) - (Z_{a1}-Z_{a2})}}, \tag{3.20}$$

$$k_{eq} = \frac{1}{2je} ln\left(\frac{Z_{a1}-Z_c}{Z_{a1}+Z_c}\frac{Z_{s1}+Z_c}{Z_{s1}-Z_c}\right) \tag{3.21}$$

where Z_{a1} and Z_{a2} are the impedance of a closed tube with different air space depths of d_1 and d_2 respectively, Z_{s1} and Z_{s2} are the reference surface impedances, and e indicates a thickness of a porous sample. The impedances of a closed tube are given

$$\begin{aligned} Z_{a1} &= -\,j\rho_0 c_0\, cot(k_0 d_1), \\ Z_{a2} &= -\,j\rho_0 c_0\, cot(k_0 d_2) \end{aligned} \tag{3.22}$$

where $k_0 = \omega/c_0$ is the acoustic wave number.

3.2.3 Equivalent parameters of the composite fibre

The porous material considered in the plate-cavity test case is a composite fibre of a thickness of 30 mm that has been cut from the rear surface insulator of *Midlum Renault Truck* cabin as seen in Fig. 3.7. To characterize it, the cutout sample has been placed at one end of the impedance tube. Following the procedure described in Section 3.2.2, Z_c and k_{eq} are obtained from a set of measured surface impedances (Z_{s1}, Z_{s2}) and Eq. 3.20 and 3.21. *B&K* impedance tube type 4206 (available frequency range: 50 Hz $\sim$ 6.4 kHz) is used for the measurements. A big tube with a diameter of 10 cm is used to measure Z_{s1}, Z_{s2} for frequencies up to 1.6 kHz, and a small tube with a diameter of 3 cm is used for a range from 1.6 kHz to 6.4 kHz.

Obtained parameters are shown in Fig. 3.8. Note that Z_c is normalized with the air impedance $\rho_0 c_0$. Once Z_c and k_{eq} are obtained from the measurements using Eq. 3.20 and 3.21, the equivalent fluid parameters ($\tilde{c}_{eq}, \tilde{\rho}_{eq}, \tilde{K}_f$) can be deduced with Eq. 3.17 and 3.18. Determined equivalent fluid celerity, density and compressibility of the composite fibre are shown in Fig. 3.9. Visible transitions in the experimental data above 1.6 kHz are due to the change of the tube size in the measurements. To evaluate the results, Z_c and

(a) (b)

Figure 3.7: Composite fibre of *Midlum Renault Truck*: (a) Composite rear surface insulator, (b) Composite fibre sample cutout

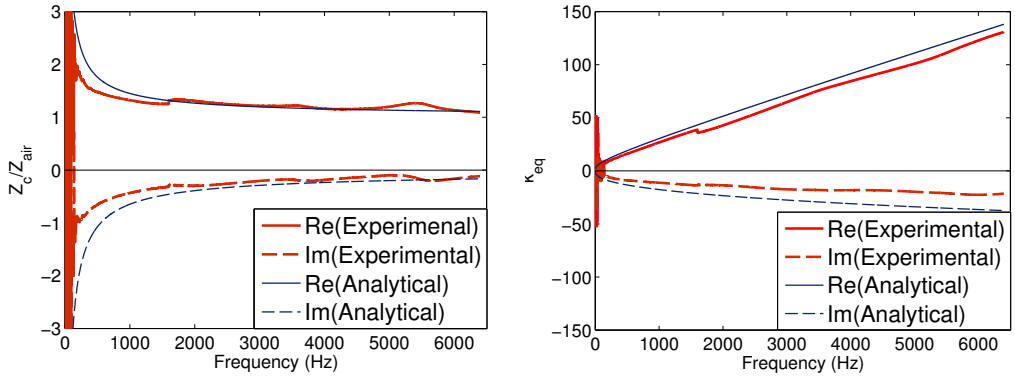

(a) (b)

Figure 3.8: Complex equivalent parameters of the composite fibre: (a) Normalized characteristic impedance, (b) Equivalent fluid wavenumber

k_{eq}, are computed using the empirical Delany-Bazley model given in Eq. 3.19. Note that the flow resistivity σ required for the analytical calculation is provided by *Renault Truck*. Subsequently, equivalent parameters are determined using Eq. 3.17 and 3.18 and compared to the experimental results.

The Delany-Bazley model is an empirical model represented in terms of Power-law relations: its prediction accuracy is normally given within the confidence range of the adimensional number (X) that quantifies the relative importance of inertial effects compared to viscous ones [28]. The experimental results are comparable with Delany-Bazley model result considering the nominal value of the flow resistivity.

In order to evaluate the equivalent parameters estimated with "Two-cavity method," a FE simulation including the equivalent fluid has been carried out on the test case, and the results have been compared

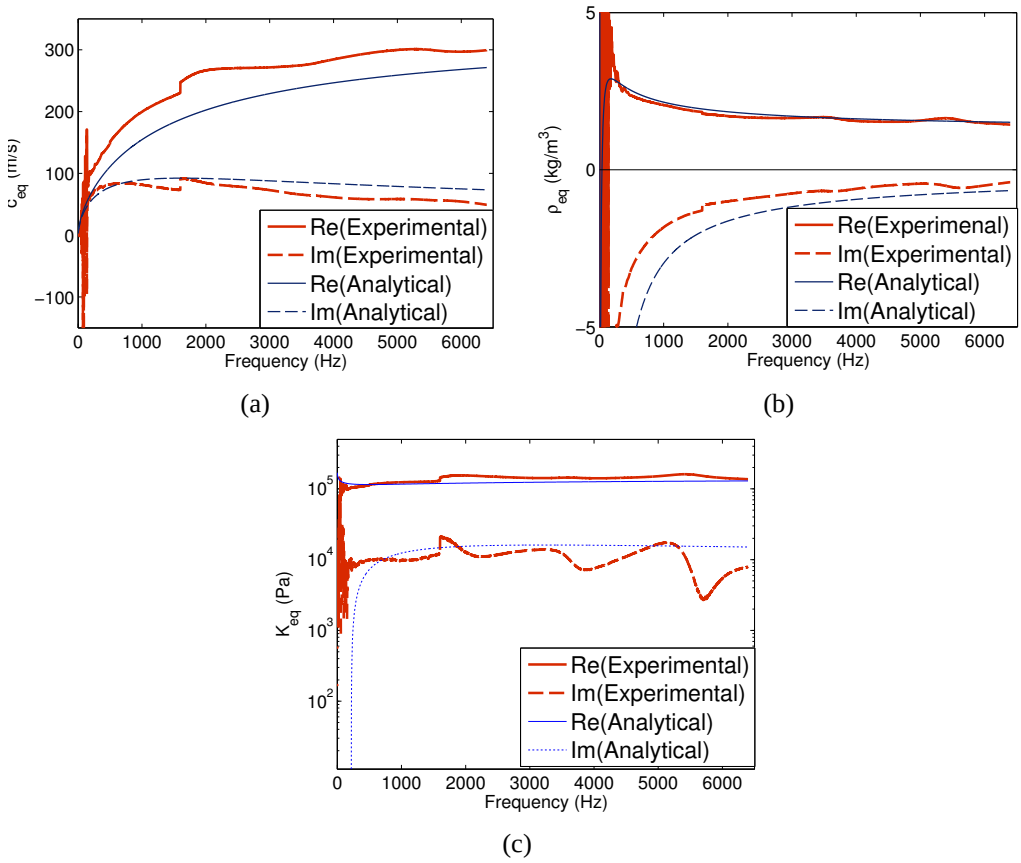

Figure 3.9: Complex equivalent parameters of the composite fibre: (a) Equivalent celerity, (b) Equivalent density, (c) Equivalent compressibility

to measured data. The test case is the big impedance tube with the composite fibre at one end. Fig. 3.10 shows a mesh model of the impedance tube. The mesh model is three dimensional solid, isoparametric

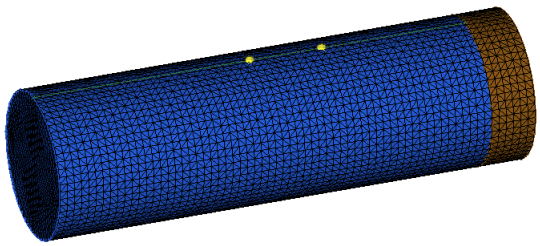

Figure 3.10: FE model of the impedance tube terminated by the composite fibre (Blue component: air, Brown component: composite fibre, Yellow dots: microphone locations)

tetrahedral element, and a mesh size is determined to have a minimum of six elements on the wavelength of air at 6 kHz. The composite fibre of 30 mm is placed at one end of the tube and is terminated by a rigid end. The inner tube surface is also rigid so that the normal components of the particle velocity are zero. Sound pressure is computed at two observation points whose locations are identical to those of the microphones. Within the FE model, the composite fibre is defined as a fluid component whose frequency

dependent complex equivalent parameters ($\tilde{c}_{eq}$ and $\tilde{\rho}_{eq}$) are considered. *ACTRAN* software has been used to compute the frequency response.

Fig. 3.11 compares experimental and numerical results for the frequency responses measured at the second microphone position and the modal damping loss factor. The half-power bandwidth method has been used to estimate the modal damping. It can be seen that the first two resonant peaks (frequency positions and bandwidths) are relatively in good agreement. The modal damping loss factors of the numerical response are lower than experimental ones where the discrepancy in between is about 49 % in average. The amplitudes are seen different between two results since the velocity of the loudspeaker membrane inside the tube has not been measured while unit velocity has been imposed in the FE calculation. It has been demonstrated that the comparisons with the Delany-Bazley model and the FE simulation allows the validation of the process to estimate the equivalent parameters.

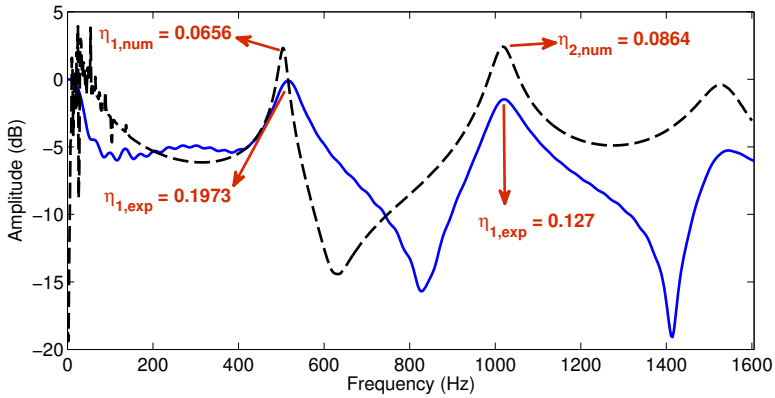

Figure 3.11: Frequency response of the impedance tube terminated by the composite fibre and the modal damping loss factor (Solid: experimental, Dashed: numerical *ACTRAN* software). Amplitudes normalized with the numerical maximum. The damping loss factor is indicated for each resonant peak.

3.3 Estimation of the modal damping loss factor

Once each dissipative material is properly defined with a simplified equivalent model, a subsequent task is to determine the modal parameters of the subsystems to which the materials are applied. These parameters are modal frequencies, modeshapes at the coupling surface and the modal damping loss factors that need to be determined in order to compute the intermodal coupling loss factor (β_{pq}^{12} in Eq. 2.19). Therefore, the objective for the plate-cavity test case is to estimate these parameters for (1) the plate damped with a viscoelastic material ($\omega_p^1, \Phi_p^1, \eta_p^1$) and (2) the cavity damped with a porous material ($\omega_q^2, \Phi_q^2, \eta_q^2$). Subsequently, the intermodal spectral coupling factor β_ω^{12} can be computed. It should be noted that the subsystems are uncoupled with predefined boundary conditions so that FE computations can be performed to give the modal parameters.

Estimation of the modal damping loss factor of each subsystem is presented in this section. For the plate, the MSE method [84] is performed. Section 3.3.1.1 presents its methodology, and calculation examples of the plate models damped with PVC patches are given in Section 3.3.1.2. For the cavity, the MSKE

method [88] is performed. Section 3.3.2.1 presents its methodology, and calculation examples with the impedance tube damped with the composite fibre are given in Section 3.3.2.2.

Both methods have been implemented into the modal extraction of *NASTRAN* software so that the modal damping loss factors are included in the output of the computation.

3.3.1 Modal strain energy method

3.3.1.1 Methodology

The Modal Strain Energy (MSE) method [84] is a numerical approach to estimate the modal damping loss factors of structures treated with viscoelastic damping material. It has been proven sufficiently accurate and efficient in terms of computational cost hence widely used in various applications [46] [92] [50]. The method considers a linear viscous damping model that is derived from the eigenvalue analysis of a complex stiffness model.

A structure damped with a viscoelastic layer is considered. The equation of motion of the discretized FE system in the frequency domain is given by

$$\left\{K^* - \omega^2 M\right\} u = F \tag{3.23}$$

where K^* is the complex stiffness matrix, M is the mass matrix, u is the displacement vector and F is the force. The normal mode n satisfies

$$\left\{K - \omega_n^2 M\right\} \Phi_n = 0 \tag{3.24}$$

where ω_n is the angular modal frequency and Φ_n is the spatial modeshape normalized by a unit mass i.e. $\Phi_n^T M \Phi_n = 1$. The displacement u can be expressed as a linear combination of the normal modes as follows

$$u = \sum_{k=1}^{n} A_k \Phi_k \tag{3.25}$$

where A_k is the modal amplitude of mode k. Substituting Eq. 3.25 into u, Eq. 3.23 can be written, using the modal orthogonality property and neglecting the cross modal term in the imaginary part, as follows

$$\left[\omega_n^2 \left\{1 + j\frac{\Phi_n^T Im\{K^*\}\Phi_n}{\omega_n^2}\right\} - \omega^2\right] A_n = F_n \tag{3.26}$$

where $F_n = \Phi_n^T F$. By comparing Eq. 3.26 with the standard model equation of complex stiffness given by

$$\left[\omega_n^2(1 + j\eta_n) - \omega^2\right] A_n = F_n, \tag{3.27}$$

the modal damping loss factor can be obtained:

$$\eta_n = \frac{\Phi_n^T Im\{K^*\}\Phi_n}{\omega_n^2} \tag{3.28}$$

Although the elastic Young's modulus is frequency and temperature dependent, the MSE method requires material properties to be constant for a given eigenvector (modeshape) [40]. Therefore, these parameters are normally estimated based on average values for a given frequency band. Such process should be respected for different frequency bands (1/3 octave bands, for instance). It should be noted that viscoelastic material within the MSE method must conform to the dynamic stress-strain behavior [40].

3.3.1.2 Model example

The MSE method is used to calculate the damping loss factor of the finite plate models shown in Fig. 3.4 of Section 3.1.2. The first two resonant frequencies and associated modal loss factors of three damped plate models given in the publication [71] are computed with the MSE method. The results are then compared to measured data using the half-power bandwidth method in the publication. As seen in Table 3.3, the

PVC arrangement	Method	η_1	η_2
Full coverage	Reference (experimental)	0.047	0.04
	MSE	0.04	0.04
Configuration 8	Reference (experimental)	0.036	0.024
	MSE	0.0282	0.0281
Configuration 10	Reference (experimental)	0.033	0.028
	MSE	0.029	0.029

Table 3.3: The system modal damping loss factors (of the first two resonant modes) of the aluminum-PVC plate models. The reference data [71] are measured with the half-power bandwidth method.

MSE method gives good approximated values comparable to the reference data. However, the values are generally underestimated in this case. An average discrepancy between models is around 11 %.

3.3.2 Modal strain kinetic energy method

3.3.2.1 Methodology

The Modal Strain Kinetic Energy method, recently proposed by Yamaguchi et al [88], extends the MSE method to take account of porous materials. It was developed to approximate the modal damping loss factor of automotive double-wall structures in FE modeling where a porous material is characterized as an equivalent fluid component of which the damping effect is coupled with that of a viscoelastic solid component. The porous fluid phase is considered so that the sound field is characterized with the complex equivalent density and the compressibility. A viscoelastic solid part is characterized with complex modulus. The modal damping of the total system is approximated from a ratio of the strain/kinetic energies of the damping elements to the energies of the total system. The equation of motion in [88] is formulated in displacement whereas the FE (*NASTRAN* software) computation is made with respect to the pressure vector. It has been redeveloped in a slightly different manner here, considering the pressure formulation.

The differential equation describing an acoustic field (air) treated with a porous material (equivalent fluid) can be expressed as

$$(K^* - \omega^2 M^*)P = u \tag{3.29}$$

where P is the nodal pressure vector in the frequency domain and u is the flow velocity. The sound field is composed of the air and the equivalent fluid that are expressed with the kinetic energy matrix K^* (complex stiffness) and the strain energy matrix M^* (complex mass) [26] as follows

$$\begin{aligned} K^* &= \frac{\bar{K}_0}{\rho_0} + \frac{\bar{K}_{eq}}{\rho^*_{eq}}, \\ M^* &= \frac{\bar{M}_0}{\rho_0 (c^*_0)^2} + \frac{\bar{M}_{eq}}{\rho^*_{eq}(c^*_{eq})^2} \end{aligned} \tag{3.30}$$

where subscripts $0, eq$ indicate the air and the equivalent fluid respectively and the overline $(-)$ indicates that a matrix corresponds to the elementary matrix (depending only on the element geometry and the element interpolation functions). The air and porous material are characterized with the complex fluid density and compressibility:

$$\rho_0 (c^*_0)^2 = \rho_0 c_0^2 (1 + j\eta_0) \tag{3.31}$$

$$\rho^*_{eq} = \rho_{eq}(1 + j\chi_e), \quad \rho^*_{eq}(c^*_{eq})^2 = \rho_{eq} c^2_{eq}(1 + j\eta_e) \tag{3.32}$$

where η_0 is the damping describing the energy dissipated in the air, $\eta_e = \frac{Im\{\tilde{K}_f\}}{Re\{\tilde{K}_f\}}$, $\chi_e = \frac{Im\{\tilde{\rho}_{eq}\}}{Re\{\tilde{\rho}_{eq}\}}$ are the material damping describing the energy dissipated by thermal and viscous effect in the porous material [88]. Substituting Eq. 3.31 and 3.32 into Eq. 3.30, Eq. 3.29 can be written as

$$\left[\bar{K}_0 + \frac{\bar{K}_{eq}}{1+\chi_e^2}(1 - j\chi_e) - \omega^2(\bar{M}_0 + \bar{M}_{eq}) - j\omega^2(\eta_0 \bar{M}_0 + \eta_e \bar{M}_{eq})\right] P = u \tag{3.33}$$

The normal mode of the conservative system satisfies

$$\left\{(\bar{K}_0 + \bar{K}_{eq}) - \omega_n^2(\bar{M}_0 + \bar{M}_{eq})\right\} \Phi_n = 0 \tag{3.34}$$

where Φ_n is the spatial modeshape normalized by a unit mass i.e. $\Phi_n^T(\bar{M}_0 + \bar{M}_{eq})\Phi_n = 1$. The modal expansion can be substituted into P:

$$P = \sum_{m=1}^{n} A_m \Phi_m \tag{3.35}$$

Subsequently, projecting the resulted equation on the modeshape Φ_n and neglecting the cross modal term in the imaginary part, Eq. 3.33 can be written as

$$\left[\bar{\omega}_n^2 \left\{1 - j\frac{\chi_e}{1+\chi_e^2}\frac{\Phi_n^T \bar{K}_{eq}\Phi_n}{\bar{\omega}_n^2}\right\} - \omega^2\left\{1 - j(\eta_0 \Phi_n^T \bar{M}_0 \Phi_n + \eta_e \Phi_n^T \bar{M}_{eq}\Phi_n)\right\}\right] A_n = u_n \tag{3.36}$$

where $u_n = \Phi_n^T u$ and $\bar{\omega}_n^2$ is the modal angular frequency given by

$$\bar{\omega}_n^2 = \Phi_n^T \bar{K}_0 \Phi_n + \frac{1}{1+\chi_e^2}\Phi_n^T \bar{K}_{eq}\Phi_n \tag{3.37}$$

By introducing

$$\bar{\chi}_n = \frac{\chi_e}{1+\chi_e^2}\frac{\Phi_n^T \bar{K}_{eq}\Phi_n}{\bar{\omega}_n^2} \tag{3.38}$$

and

$$\bar{\eta}_n = \eta_0(\Phi_n^T \bar{M}_0 \Phi_n) + \eta_e(\Phi_n^T \bar{M}_{eq} \Phi_n), \tag{3.39}$$

Eq. 3.36 can be written as

$$\left\{\bar{\omega}_n^2(1 - j\bar{\chi}_n) - \omega^2(1 - j\bar{\eta}_n)\right\} A_n = \Phi_n^T u \tag{3.40}$$

The modal damping is assumed to be small ($\bar{\eta}_n \ll 1$) since it is generally $\eta_0 \ll 1, \eta_{eq} \ll 1$. Eq. 3.40 can be then approximated as

$$\left[\bar{\omega}_n^2 \left\{1 + j(\bar{\chi}_n + \bar{\eta}_n)\right\} - \omega^2\right] A_n = \Phi_n^T u \tag{3.41}$$

By comparing Eq. 3.41 with the standard model equation (see Eq. 3.27), the modal damping loss factor η_n can be obtained as follows

$$\eta_n = (\eta_0 SE_0 + \eta_e SE_{eq}) - \left\{\frac{\chi_e}{1 + \chi_e^2} KE_{eq}\right\} \tag{3.42}$$

where

$$\begin{aligned} SE_0 &= \Phi^T \bar{M}_0 \Phi \\ SE_{eq} &= \Phi^T \bar{M}_{eq} \Phi \\ KE_{eq} &= \frac{\Phi^T \bar{K}_{eq} \Phi}{\bar{\omega}_n^2} \end{aligned} \tag{3.43}$$

SE_0, SE_{eq} are the ratio of the elastic strain energy of each element (air and equivalent fluid) to the total strain energy of the system, and KE_{eq} are the ratio of the elastic kinetic energy of the equivalent fluid to the total kinetic energy of the system. The modal damping loss factor η_n of the total system in Eq. 3.42 includes the damping loss factor of the air component and of the porous component.

3.3.2.2 Model example

The MSKE method is used to approximate the modal damping loss factor of the impedance tube test case damped with the composite fibre, presented in Section 3.2.3. The same FE model shown in Fig. 3.10 has been used to extract the strain and kinetic energy of the system with *NASTRAN* software for frequencies up to 5 kHz band. The modal damping loss factor (η_n) is determined in 1/3 octave band with the frequency dependent material loss factors ($\eta_e = \frac{Im\{\tilde{K}_f\}}{Re\{\tilde{K}_f\}}, \chi_e = \frac{Im\{\tilde{\rho}_{eq}\}}{Re\{\tilde{\rho}_{eq}\}}$) determined from the values presented in Fig. 3.9c and 3.9b of the composite fibre respectively. η_e and χ_e of the composite fibre are averaged over each frequency band as shown in Fig. 3.12 and are considered in Eq. 3.42 in order to determine the modal damping loss factor. The air damping of the impedance tube with rigid terminations at both ends experimentally estimated with the high-resolution modal analysis method based on the ESPRIT algorithm [36] (the method further detailed in next chapter) from the frequency response measured with microphones. The modal damping loss factors of the empty impedance tube are plotted in Fig. 3.13.

Fig. 3.14 compares the MSKE predictions to experimental results estimated with the ESPRIT algorithm on the impedance tube damped with the composite fibre. The MSKE method has overestimated a few modes in this case, however, such values can be explained by highly localized damping effect of the com-

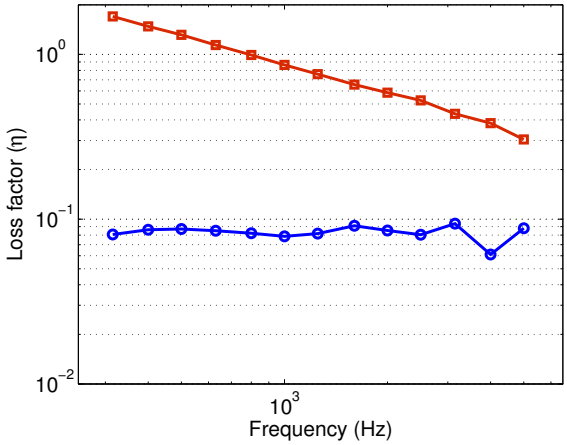

Figure 3.12: Material loss factors of the composite fibre in 1/3 octave band (□: χ_e, ◯: η_e)

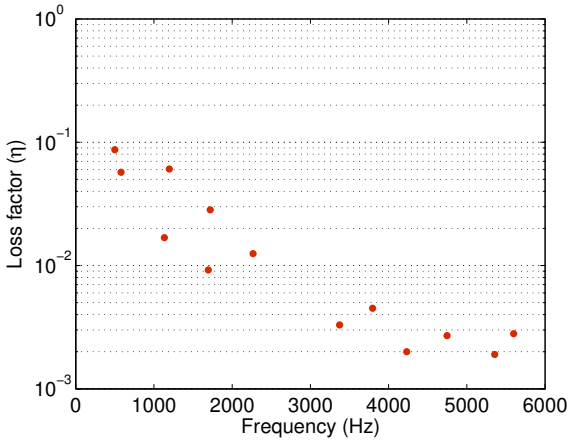

Figure 3.13: Experimental modal damping factors (using the ESPRIT algorithm) of the impedance tube terminated by a rigid wall

posite fibre inside the tube. Fig. 3.15 shows modeshapes of the tube at two resonant modes. The modal damping at 2970 Hz (marked with arrow in Fig. 3.14) is significantly higher than other modes in considered frequency band since its resonant mode is completely localized in the region of the composite fibre where much of the modal energy is dissipated within (see Fig. 3.15). No detectable mode in the frequency response of the tube explains the absence of modal values around that frequency in the experimental result. On the other hand, the modal energy at 3451 Hz is well distributed over the tube, particularly near the microphones, resulting in low energy dissipation (see Fig. 3.15). This is also observed in the experimental value at 3401 Hz (marked with arrow in Fig. 3.14). It is clear that the ESPRIT algorithm can not detect all the modes, particularly ones that are heavily damped. It is more effective estimating the damping of weakly damped modes that have significant modeshape amplitudes at the microphone positions. It explains why the MSKE method has given a high number of modes and relatively higher damping loss factor than the ESPRIT algorithm.

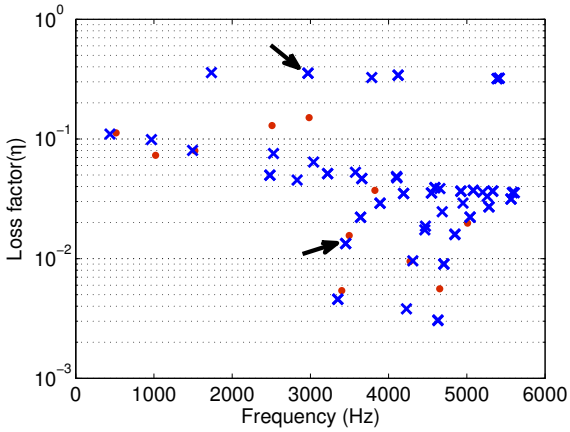

Figure 3.14: The damping factors of the impedance tube terminated by the composite fibre (•: experimental, ×: MSKE)

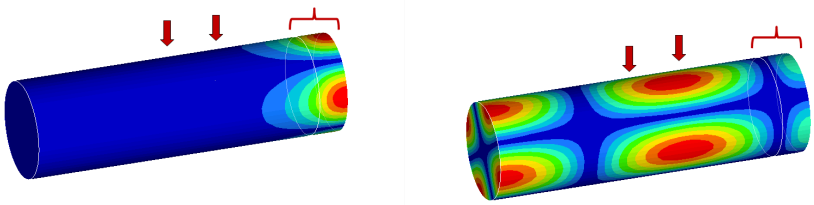

(a) (b)

Figure 3.15: Modeshape of the impedance tube with the composite fibre (Arrow and parenthesis indicate the microphone position and the composite fibre position respectively): (a) At 2970 Hz, (b) At 3451 Hz

3.4 Conclusion

The equivalent single layer model has been presented and applied on the plate treated with viscoelastic layers. This model provides a simple approach for determining the response of a multi-layered plate in FE modeling. Frequency dependent equivalent parameters can be determined from viscoelastic properties of each layer. Subsequently, FE modeling can be easily performed without defining the coupling between layer interfaces. The method applied on the plate examples has demonstrated a reasonable performance and a significantly reduced computational cost compared to the double layer models.

The composite fibre has been modeled as an equivalent fluid by assuming a rigid solid frame under an airborne plane-wave excitation. The method simplifies the Biot's coupled equations (between fluid and solid) and drastically reduces computational cost. With "Two-cavity-method," the model parameters have been easily determined, and the values are in good agreement with the predictions of the Delany-Bazley empirical model.

The MSE and MSKE methods have been adopted to determine the modal damping loss factor of a plate treated with viscoelastic PVC patches and of an acoustic cavity treated with the porous composite fibre respectively. The MSKE is an extension of MSE that includes the damping effect induced by porous materials. The MSE has produced comparable damping levels of the sample plate models compared to

the experimental values whereas the MSKE has appeared to overestimate compared to the experimental values for the impedance tube test case. However, high modal damping values can be explained by strong localization of the modes into the composite fibre and can not be estimated experimentally by the ESPRIT algorithm.

In order to extend the SmEdA technique for a structure-fluid system treated with dissipative materials, all necessary modeling techniques have been presented in this chapter: (1) the equivalent plate model associated with viscoelastic materials and the MSE method to estimate the modal damping loss factor of a damped plate and (2) the equivalent fluid model associated with porous materials and the MSKE method to estimate the modal damping loss factor of a damped cavity. In next chapter, all of the methods are applied to model a damped plate-cavity system in the framework of SmEdA.

CHAPTER 4

Test Case Applications With Dissipative Materials

The previous chapter has presented simplified methods to represent a viscoelastic layer and a porous material included in FE models. Such models associated with the MSE and MSKE methods can estimate the modal damping loss factor that is considered in the SmEdA model. Finally, the SmEdA computation can be performed taking account of the damping effect of the dissipative treatments. In this chapter, the methodology is applied to the plate-cavity system including the dissipative materials that are used in the CLIC truck cabin.

- Section 4.1 introduces two damped test cases: (1) a system with the viscoelastic damping pad on the plate and (2) a system with the composite fibre in the cavity.
- Section 4.2 presents the damping loss factors of uncoupled subsystems estimated with the MSE and MSKE methods.
- Section 4.3 presents the analyses of the damped test cases in comparison with the original case with no damping treatment.

4.1 Description of the different damped configurations

Two test cases have been arranged for the dissipative materials applied to the plate-cavity system: (1) the plate damped with the viscoelastic damping pad and (2) the cavity damped with the composite fibre. The objective is to achieve the SmEdA computation on these two treatment cases and to compare the results to the original system without treatment. Test cases are named as follows

- *Bare*: bare plate coupled to empty cavity.

- *Visc1*: plate treated with one viscoelastic damping pad coupled to empty cavity.
- *Visc2*: plate treated with two viscoelastic damping pad coupled to empty cavity.
- *Poro*: bare plate coupled to cavity treated with the composite fibre.

The dissipative materials are shown in Fig. 4.1. Both materials are originally used in *Midlum* truck cabin BIW and have been provided by *Renault Truck*.

The viscoelastic layer is a 2.6 mm thick prefabricated damping pad. It can be semi-permanently attached to the plate by being heated. A single damping pad occupies 15 % of the plate surface area and its mass is

(a) (b)

Figure 4.1: Dissipative materials inside *Midlum Renault Truck*: (a) Viscoelastic damping pad, (b) Composite fibre from the rear surface insulator (membrane in red circle presented in Fig. 3.7a)

approximately 19 % of the plate mass. The composite fibre is 3 cm thick mineral fibre, taking around 2 % of the cavity volume. This material has been already modeled as the equivalent fluid whose properties have been presented in Section 3.2.3. Fig. 4.2 presents damped uncoupled subsystem configurations for the test cases. Fig. 4.3 illustrates the test cases of the plate-cavity system.

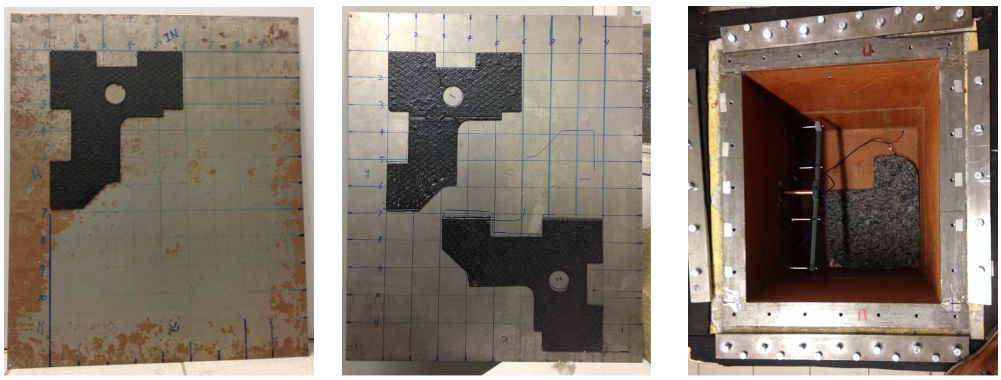

(a) (b) (c)

Figure 4.2: Treated subsystems: (a) *Visc1*, (b) *Visc2*, (c) *Poro*

At first, the parameters of the equivalent plate and the equivalent fluid are determined. Model parameters of the equivalent plate will be presented in following section. The composite fibre is modeled as an equivalent fluid whose model properties have been presented in Section 3.2.3. Subsequently, each subsystem

(a) (b) (c)

Figure 4.3: SmEdA test cases of the dissipative materials: (a) *Bare*, (b) *Visc1&2*, (c) *Poro*

is modeled with FE software with the equivalent parameters assigned to the damping components. The plate is modeled with 13,776 of shell element, and the cavity is modeled with 4,031,412 of solid, isoparametric tetrahedral elements. The plate and cavity mesh sizes are determined in order to have a minimum of six elements on bending wavelength at 8 kHz and air wavelength at 6 kHz respectively. Modeshapes and resonant frequencies of the subsystems are obtained using *NASTRAN* modal extraction of the Lanczos method. Fig. 4.4 presents mesh models of the damped subsystems. Each model is uncoupled subsystems whose boundary conditions are predefined under the SmEdA formulation. While computing the FE models, the system matrices (mass and stiffness) are extracted to compute the modal damping loss factor using the MSE and MSKE methods. As the final step, SmEdA calculation can be performed. The modal

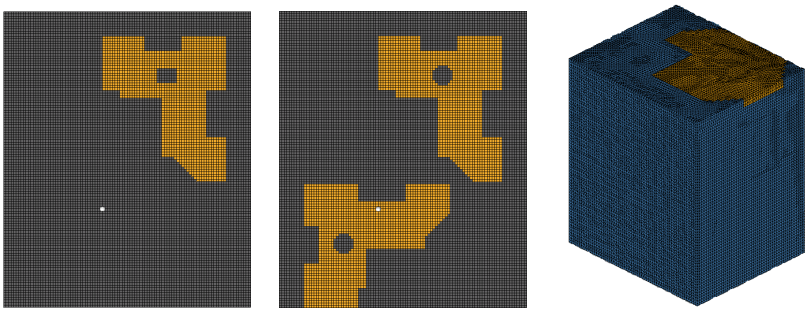

(a) (b) (c)

Figure 4.4: Damped subsystem mesh model (White point on the plate indicates the excitation point): (a) *Visc1*, (b) *Visc2*, (c) *Poro* (Figure seen upside down)

injected power considered in each test case corresponds to a normal point force exerted at the plate coordinate $(x, y) = (0.2, 0.2)$ (m) (the same point as *Bare* case presented in Section 2.2.4). Fig. 4.5 illustrates a SmEdA computation process in block diagrams. The influence of the damping on subsystem energy exchange is then analyzed by assessing *Visc1&2* and *Poro* cases versus *Bare*.

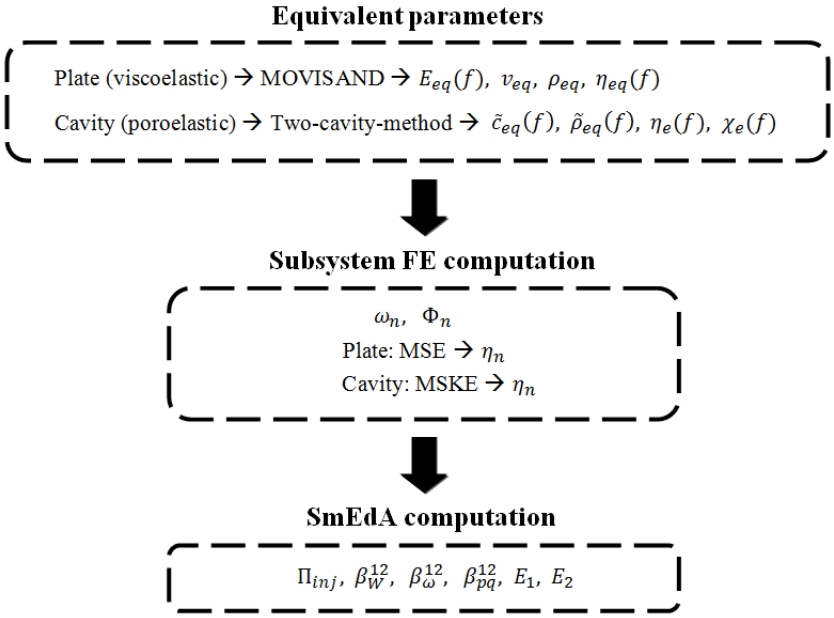

Figure 4.5: SmEdA modeling process. Model parameters are given in Eq. 2.26 (Π_{inj}), 2.19 (β_{pq}^{12}), 2.20 (β_W^{12}) and 2.23 (E_1, E_2)

4.2 Estimation of the subsystem modal damping loss factor

4.2.1 Plate damping

In order to determine the damping loss factor of *Visc1&2* plates, equivalent parameters are first determined using *MOVISAND* software. Calculations are made using the WLF model for the viscoelastic material (given in Eq. 3.10) at 20 °C. Material properties (ρ, v), polynomial coefficients (A_n, B_n) and empirical constants (c_1, c_2) of the viscoelastic damping pad were provided by *ACOEM*. They have been measured using the DMA testing (Dynamic Mechanical Analysis), a technique used to characterize the viscoelastic behavior of polymers [39]. The material properties of the plate, viscoelastic damping pad and equivalent layer (plate + viscoelastic damping pad) are presented in Table 4.1. The density of the steel plate has been calculated from the total weight ($M = \rho h S$ where h, S are thickness and total surface area respectively), and Young's modulus has been determined from an averaged relative natural frequency difference of the free-free plate for a first few modes between FE model and experimental result.

Material properties of the plate, viscoelastic damping pad and equivalent layer (plate + viscoelastic damping pad) are presented in Table 4.1. The parameters of the viscoelastic damping pad and equivalent layer have been computed for an infinite plate. Frequency dependent Young's modulus and damping loss factor are plotted in Fig. 4.6. Note that the damping loss factor of the plate has been experimentally determined by the high-resolution modal analysis method, which will be detailed in Section 5.2.4.1. They are averaged from modal values determined for selected resonant modes in 1/3 octave band. It is seen that the damping loss factors of the viscoelastic damping pad are substantially greater than those of the plate while Young's modulus is seen otherwise. The damping loss factor of the equivalent layer has been increased compared

	Steel	Damping pad	Equivalent
Thickness (mm)	1	3	4
E (Pa)	2.03e11	$E(f)$	$E_{eq}(f)$
$\rho(\mathrm{kg/m^2})$	7523	1533	3196
v	0.33	0.35	0.34
η	$\eta(f)$	$\eta(f)$	$\eta_{eq}(f)$

Table 4.1: Mechanical properties of the plate, damping pad and equivalent plate estimated with the equivalent single layer modeling (*MOVISAND* software)

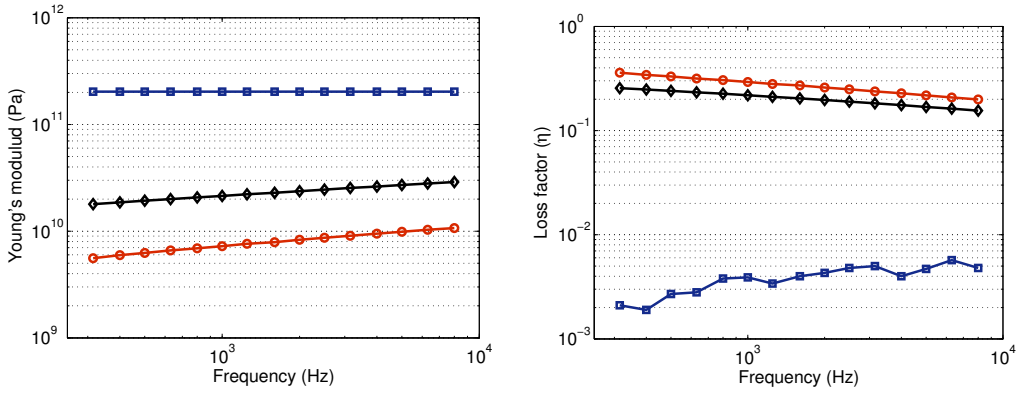

(a) (b)

Figure 4.6: Properties of the plate components in 1/3 octave band. The values of the viscoelastic damping pad and the equivalent layer are computed at 20 °C using *MOVISAND* software. (□: 1 mm steel plate (*Bare*), ◯: 3 mm viscoelastic damping pad, ♢: 4 mm equivalent layer): (a) Young's modulus, (b) Experimental damping loss factor

to that of the plate. It can be observed that both equivalent parameters ($E_{eq}(f), \eta_{eq}(f)$) vary gradually with frequency so that the MSE computation can be performed in each 1/3 octave band by taking the band-global values.

Fig. 4.7 presents the modal damping loss factors of *Visc1* and *Visc2* plates in comparison with those of the plate, viscoelastic damping pad and equivalent layer. Note that the modal damping loss factors are the uncoupled plate subsystem parameter (η_p^1 in Eq. 2.21). The viscoelastic damping pad gives the plate substantially high damping at low frequencies while its effect diminishes with increasing frequencies as it can be seen for decreasing values of the equivalent layer. Compared to *Visc1* plate, the values of *Visc2* are approximately 40 % higher throughout the frequency range. It can be clearly observed from both configurations that the damping levels can vary in large magnitude between resonant modes. Since some modes are weakly influenced by the viscoelastic damping pad, their damping levels remain low. These modes have low spatial deformation around the pad as seen in Fig. 4.8a for the resonant mode at 1584 Hz. This mode has the lowest damping level (marked in circle in Fig. 4.7) in the frequency band (1.6 kHz). In contrary, some modes are highly damped as their spatial deformation occurs around the pad. This can be seen for the high modal damping level at 1828 Hz (marked in circle in Fig. 4.7) in its modeshape presented in Fig. 4.8b.

Such variation of the modal damping loss factor can be taken into account in frequency band SmEdA

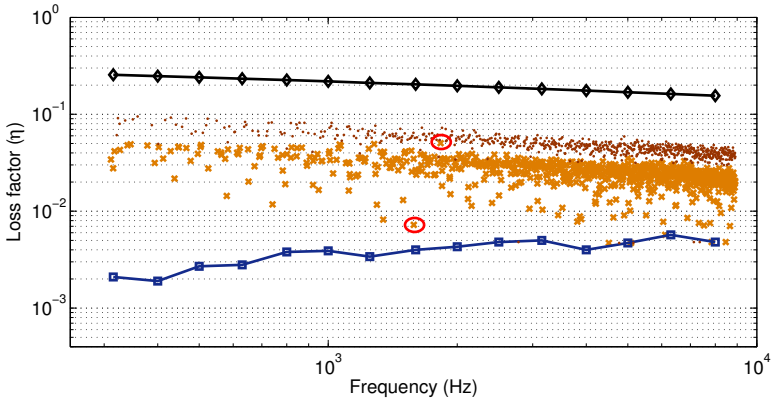

Figure 4.7: The damping loss factor (♢: 4 mm equivalent layer, □: experimental result of the steel plate (*Bare*) averaged in 1/3 octave band, ×: modal values of *Visc1* plate estimated with MSE, •: modal values of *Visc2* plate estimated with MSE)

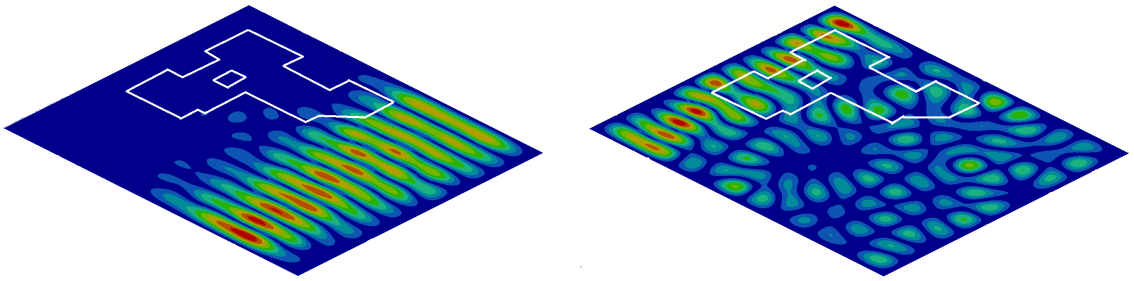

(a) (b)

Figure 4.8: Modeshape of *Visc1* plate: (a) At 1584 Hz, (b) At 1828 Hz

analysis for determining a prediction interval of the subsystem energy ratio. Such analysis will be presented in Section 5.3.

4.2.2 Cavity damping

The damping loss factor of the cavity treated with the composite fibre has been estimated with the MSKE method. The material loss factors of the equivalent fluid η_e, χ_e have been determined in Section 3.2.3. These parameters are assigned to the the equivalent fluid component in the FE model of *Poro* cavity. While FE computation is performed, the damping loss factor is computed following Eq. 3.42 in 1/3 octave band with extracted mass and stiffness matrices of the air and the porous components. Note that the damping level of *Poro* cavity is determined up to the 5 kHz band since the equivalent fluid parameters obtained with the impedance tube measurement are valid until 6.4 kHz.

Fig. 4.9 plots the damping loss factors of the empty cavity (*Bare*) and *Poro* cavity in 1/3 octave band. Note that the modal damping loss factors of *Poro* cavity are the uncoupled subsystem parameter (η_q^2 in Eq. 2.21). The empty cavity values have been experimentally determined by the high-resolution modal analysis method, which will be detailed in Section 5.2.4.1. The empty cavity values are averaged from modal values determined for selected resonant modes in each frequency band.

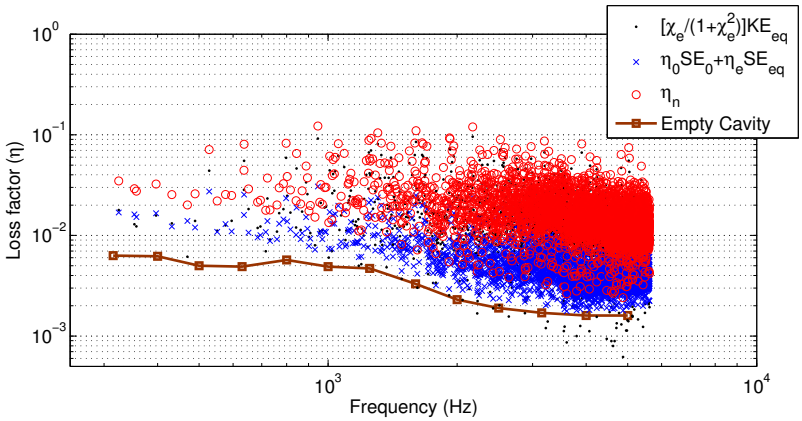

Figure 4.9: The modal damping loss factors estimated with the MSKE method

It can be seen that the composite fibre has increased the damping nearly ten times compared to the empty cavity. The composite fibre produces the damping effect due to the fluid elasticity ($\eta_e = \frac{Im\{\tilde{K}_f\}}{Re\{\tilde{K}_f\}}$) associated with the strain energy SE_{eq} and to the fluid density ($\chi_e = \frac{Im\{\tilde{\rho}_{eq}\}}{Re\{\tilde{\rho}_{eq}\}}$) associated with the kinetic energy KE_{eq} (see Eq. 3.42 and 3.43). It can be seen that the viscous and thermal effects (fluid density) strongly attribute to the total damping.

Once the modal damping loss factors are determined, all necessary parameters are available for the uncoupled subsystems and subsequently, SmEdA computation can be performed.

4.3 Influence of the dissipative materials on the plate-cavity system

4.3.1 Modal overlap

The modal overlaps of all subsystem configurations are presented in Fig. 4.10. Subsystem modal densities

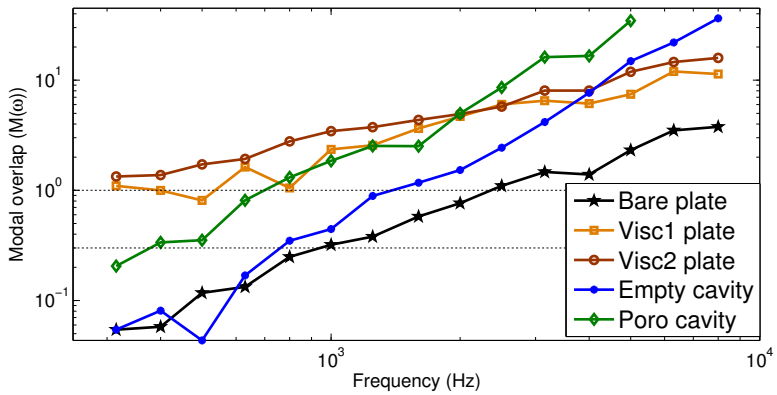

Figure 4.10: The modal overlap of the uncoupled subsystems in 1/3 octave band. Dotted lines indicate a range of the mid-frequency ($30\ \% < M < 100\ \%$)

are computed from resonant modes obtained from uncoupled FE models. The modal damping loss factors η_1, η_2 of each configuration are experimentally approximated, and frequency-band averaged (global) values

are considered for 1/3 octave band analysis. Although the modal densities of each subsystem between treated and untreated configurations at all frequencies, the modal overlaps of the treated configurations are considerably higher than those of the untreated due to the high damping. The mid frequency domain of the treated configurations (*Visc1* and *Poro*) is 500 kHz and from 500 Hz to 630 kHz respectively.

4.3.2 Modal coupling factor

Fig. 4.11 presents the intermodal spatial coupling factor β_W^{12} as a function of coupled resonant modes between two subsystems in in 1 kHz band for each test case (a whole system). It can be seen that the

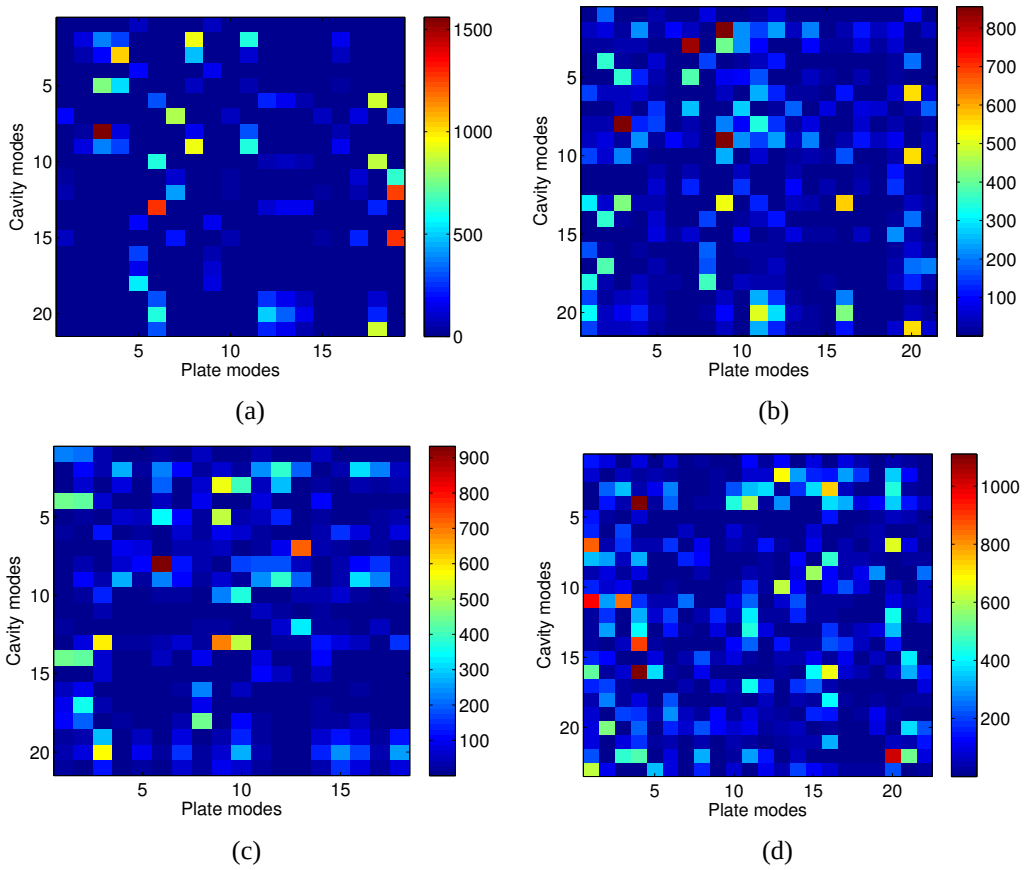

Figure 4.11: The intermodal spatial coupling factors (β_W^{12}) versus coupled resonant modes in 1 kHz band: (a) *Bare*, (b) *Visc1*, (c) *Visc2*, (d) *Poro*

treatment cases have more mode couples having significant spatial coupling factors compared to *Bare* case, however, the strongest couple (amplitude) is obtained for *Bare* case. This is contrary to *Bare* case analysis presented in Section 2.2.4.5 where no change in β_W^{12} has occurred when changing either subsystem damping loss factor. On the other hand, the number of mode couple has increased in the intermodal spectral coupling factor β_ω^{12} while their coupling strengths (amplitudes) have been diminished (see Fig. 2.15). The same phenomenon has occurred in these test cases as presented in Fig. 4.12d.

The intermodal coupling factor (β_{pq}^{12}) in 1 kHz band is presented for all test cases in Fig. 4.13. Contrary to *Bare* case where energy exchange is dominated by just two pairs of mode couples, an increasing number

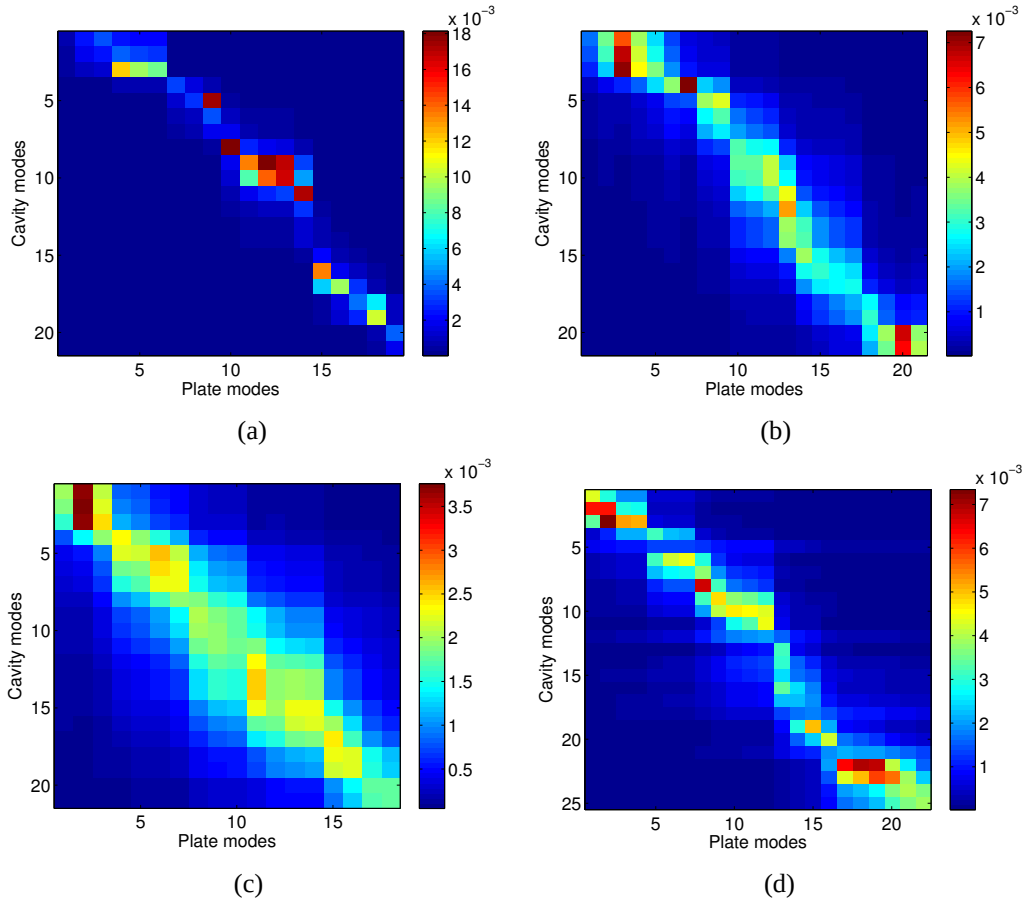

Figure 4.12: The intermodal spectral coupling factors (β_W^{12}) versus coupled resonant modes in 1 kHz band: (a) *Bare*, (b) *Visc1*, (c) *Visc2*, (d) *Poro*

of modes are coupled in the treated cases. However, it is clearly seen that their amplitudes have diminished. Such phenomenon is more prominent for the plate treatment cases (*Visc1&2*) where the number of mode couples increase as the damping effect increases. Despite the similar modal densities between untreated and treated subsystems (the number of modes in 1 kHz band for *Bare* plate: 19, *Visc1* plate: 21, *Visc2* plate: 18, *Bare* (empty) cavity: 21 and *Poro*: 25), more mode couples participate in energy exchange, approaching the energy equipartition. This is a result of the high modal overlap.

Fig. 4.14 presents the CLF (coupling loss factor) of each test case. The CLF shows an ensemble view of the subsystem modal energy exchange in a given frequency band as an average value is considered (see Eq. 2.24). The CLFs are seen to have small differences between each case, particularly above 1 kHz. Although the dissipative treatments have caused more subsystem modes to be coupled compared to *Bare* case, the coupling strengths have generally diminished in *Visc1&2*. As a result, the total amount of energy exchanged in a given frequency band has become comparable. On the other hand, *Poro* case has more energies exchanged than the rest above 1 kHz. This suggests that the amount of energy transferring from a source subsystem to a receiving subsystem depends on the damping of a receiving subsystem. It can be also seen that the CLFs of plate-cavity (η_{12}) are greater than those of cavity-plate (η_{21}). This complies with the energy reciprocity relation ($\eta_{12}/\eta_{21} = n_2(\omega)/n_1(\omega)$) and indicates that more energies transfer from the plate to the cavity than the opposite way.

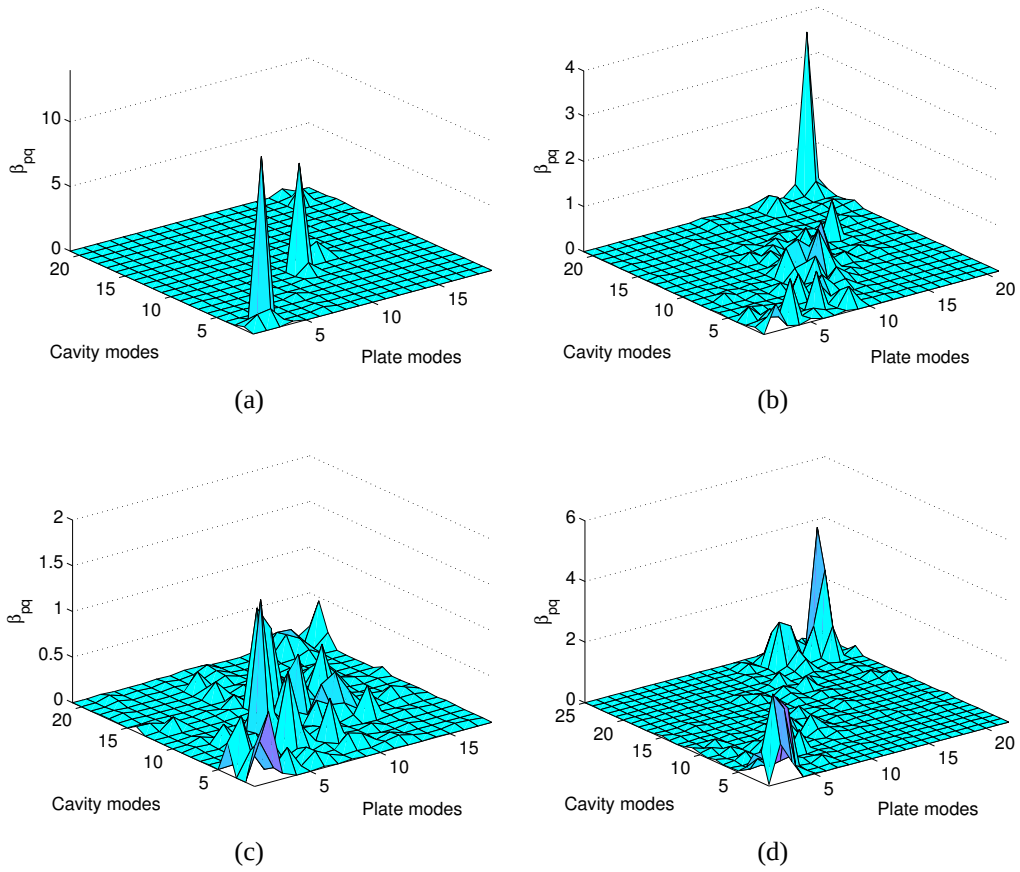

Figure 4.13: The intermodal coupling factors (β_{pq}^{12}) versus coupled resonant modes in 1 kHz band (Modes indexed with increasing natural frequencies): (a) *Bare*, (b) *Visc1*, (c) *Visc2*, (d) *Poro*

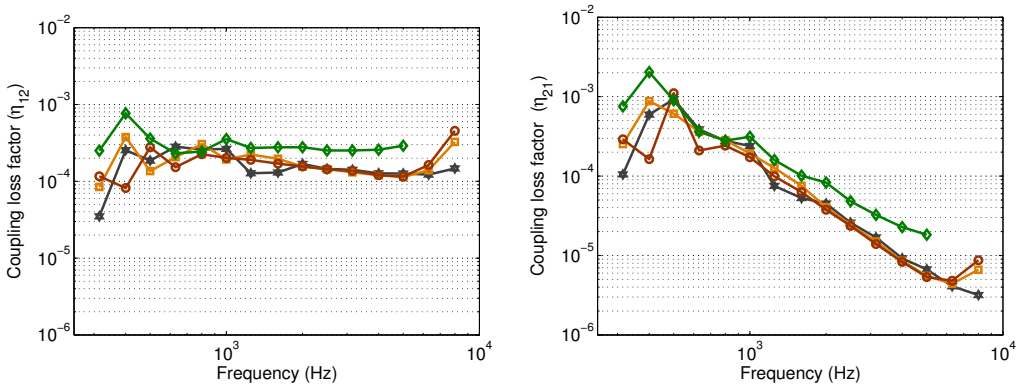

(a) (b)

Figure 4.14: Coupling loss factor of each test case in 1/3 octave band ($\star$: *Bare*, $\square$: *Visc1*, $\bigcirc$: *Visc2* and $\diamondsuit$: *Poro*): (a) Plate-cavity (η_{12}), (2) Cavity-plate (η_{21})

4.3.3 Subsystem energy

Fig. 4.15 presents subsystem energies in 1/3 octave band for all test cases that have been computed with the SmEdA method. Note that the SmEdA analysis of *Poro* case has been carried out up to the 5 kHz band following the available frequency range of *Poro* cavity. The viscoelastic damping pads induces a significant

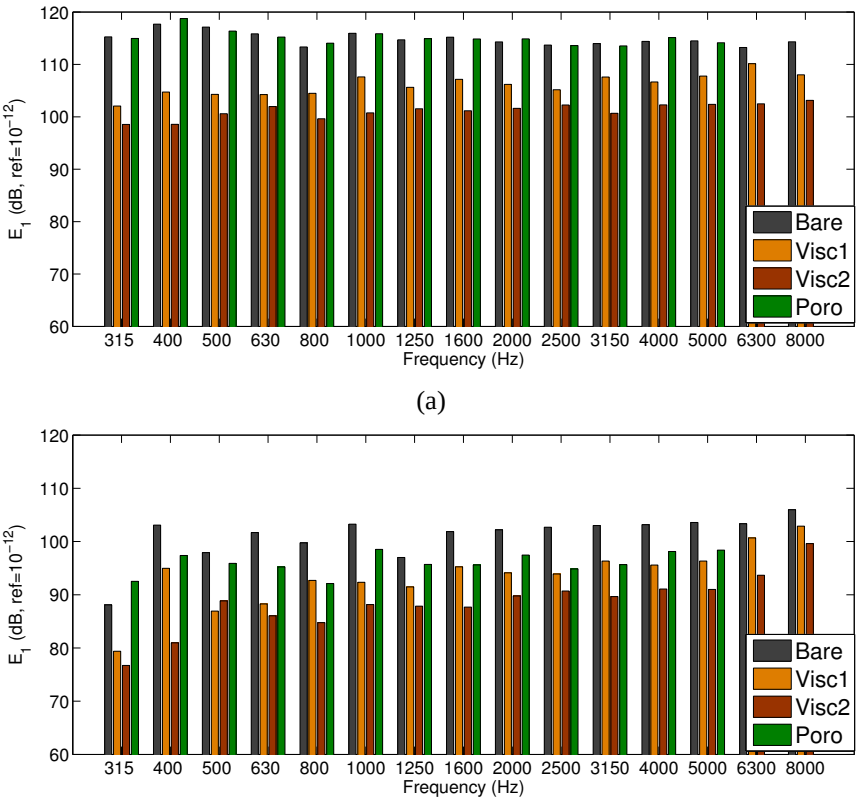

(a)

(b)

Figure 4.15: Subsystem energies of all test cases in 1/3 octave band: (1) Plate energies, (2) Cavity energies

amount of reduction to plate energies. Energies of *Visc1* are reduced by an average 7.5 dB in all frequency

bands compared to *Bare*. For *Visc2*, energies are further decreased by an average 3.3 dB compared to *Visc1* although two damping pads do not necessarily double the effect.

Cavity energies have decreased when either subsystem is treated. *Poro* case has its cavity energies reduced by an average 8 dB compared to *Bare*. However, its energy is 4 dB higher than that of *Bare* at 315 Hz. This is largely due to the spectral coupling strength (β_{ω}^{12}) that has been modified by the composite fibre. The number of subsystem modes in that frequency band is six for the plate and two for both cavity cases i.e. *Bare* (empty) and *Poro*. As presented in Table 4.2, both resonant frequencies of *Poro* cavity approach those of the plate closer than *Bare* cavity. This leads *Poro* case to have stronger spectral coupling

	Bare cavity	Plate	*Poro* cavity
Resonance (Hz)	283	303	324
	340	307	353
		308	
		318	
		330	
		335	

Table 4.2: Subsystem resonant frequencies in 315 Hz band

than *Bare* case as seen in Fig. 4.16. Consequently, its intermodal coupling factor (β_{pq}^{12}) is three times higher than *Bare* case and, in turn, its cavity modal energies (determined using Eq. 2.22) are higher as well.

It can be seen that the cavity energies of *Poro* case are higher than those of *Visc2* case by an average 5 dB at all frequencies except 500 Hz: more energies in a receiving subsystem can be reduced by heavily treating an excited subsystem rather than a receiving subsystem. However, it should be noted that this is a result of the power injection into the plate. This suggests that a structural damping treatment alone can achieve energy dissipation simultaneously in both subsystems in case of a structureborne noise source.

Fig. 4.17 shows a subsystem energy ratio (E_{cavity}/E_{plate}) of all cases. Note that subscripts for each subsystem are 1 for the plate and 2 for the cavity and will be consistent for all presented results. No substantial changes have occurred between *Bare* and *Visc1&2* at mid-high frequencies. At low frequencies below 1.6 kHz, the fact that only a few resonant modes participate in energy exchange can explain the variations. Compared to *Bare*, the ratios of *Visc1&2* cases have very small changes since the damping pads have resulted in energy reduction in both subsystems. On the other hand, the ratio of *Poro* is lower than all other cases as much as 8 dB at 800 Hz. This is due to the energy dissipation solely within the cavity while plate energies remain unchanged. This well corresponds to the result presented in Fig. 2.14 as the energy ratio has been demonstrated more sensitive to the cavity damping. As the plate is directly excited, the cavity energies are always far smaller than those of the plate unless the CLF is greater than the internal damping loss factor [91]. A change of the ratio is, therefore, not expected unless energies of a receiving subsystem are reduced in direct manner (dissipated by an absorbing material).

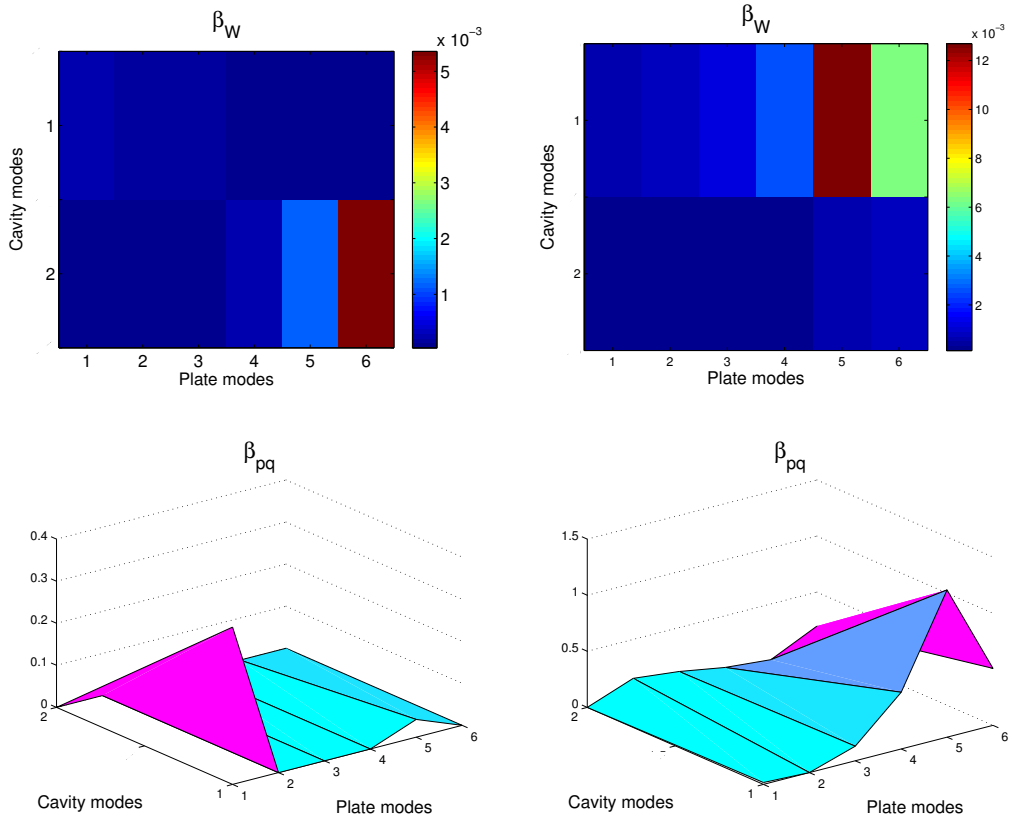

Figure 4.16: The intermodal spectral (β_{ω}^{12}) and coupling (β_{pq}^{12}) factors versus coupled resonant modes in 315 Hz band (Modes indexed with increasing natural frequencies): (Left) *Bare*, (Right) *Poro*

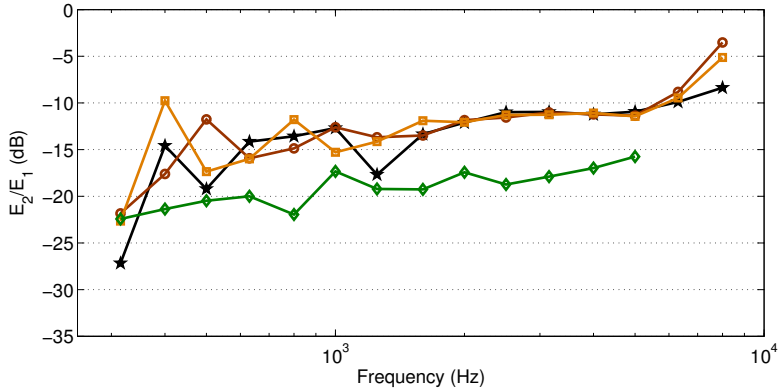

Figure 4.17: Subsystem energy ratio in 1/3 octave band using all modal damping loss factors($\star$: *Bare*, $\square$: *Visc1*, $\bigcirc$: *Visc2*, $\diamondsuit$: *Poro*)

4.4 Conclusion

The proposed methodology to include dissipative materials in the SmEdA modeling has been applied to the plate-cavity system. The plate subsystem treated with the viscoelastic damping pad has been modeled as an equivalent plate and its damping loss factor has been determined with the MSE method. The equivalent fluid method has been used to model the composite fibre placed inside the cavity and the damping loss

factor of the treated cavity has been determined with the MSKE method. Both methods have a major practical appeal for which the underlying real mode assumption leads to simplified system matrices hence reduced computational cost.

The dissipative materials have shown the clear influence on the subsystem modal coupling. More subsystem resonant modes participate in energy exchange as the dissipative materials increase the subsystem modal overlaps. However, this does not lead to more energy transmission from plate to cavity but at most indicates that energies are well distributed among modes. The amount of energy exchanged by mode couples, in fact, has been clearly reduced by the dissipative materials. It has also shown that more cavity energies are reduced by treating the plate than directly treating the cavity. This implicates that a structural damping treatment alone can achieve energy dissipation in both subsystems under a structureborne noise source. On the other hand, the subsystem energy ratio does not significantly change between treated and untreated cases particularly at mid-high frequencies unless a receiving subsystem (cavity) is directly treated.

In this chapter, the SmEdA method has been extended to include the damping effect and tested on different treatment cases. The plate-cavity system under the influence of the dissipative materials has been described in entirely numerical manner. In next chapter, all numerical results will be experimentally evaluated. The injected power, subsystem energies and subsystem damping loss factor will be compared to experimental results.

CHAPTER 5

Experimental Validation

Experimental validations are carried out on the SmEdA computation results of the plate-cavity system (*Bare*, *Visc*, *Poro*). Subsystem energies of the test cases and relative subsystem damping loss factors are experimentally estimated and are compared to the SmEdA predictions.

- Section 5.1 presents the experimental setup.
- Section 5.2 presents the measured quantities. These are input mobility, injected power, subsystem energy and subsystem damping loss factors.
- Section 5.3 presents the comparisons between numerical and experimental subsystem energies of the different test cases.

5.1 Experimental setup

Dimensions of the steel plate and the cavity are 0.54×0.64 (m^2) and $0.5 \times 0.6 \times 0.7$ (m^3) respectively. The cavity is parallelepipedic and its five surfaces are the 16 cm solid concrete that is acoustically rigid. The plate is coupled to the cavity by clamping its boundaries (of 2 cm width) with four metal bars screwed to the top ledges of the cavity. Fig. 5.1 shows the mechanical coupling of the plate-cavity system.

A stationary harmonic transverse force is exerted by *B&K* electrodynamic mini-shaker Type 4810 on the plate at the same point as the numerical models $(x, y) = (0.2, 0.2)(m)$. Measurements were performed for two frequency domains depending on the excitation spectrum. The excitation is sweep signals for (1) the low domain from 1 Hz to 3.2 kHz with a resolution 0.5 Hz and (2) the high domain from 3.2 kHz to 10 kHz with a resolution 1.5625 Hz. At the point of excitation, the force and the acceleration were measured with an impedance head.

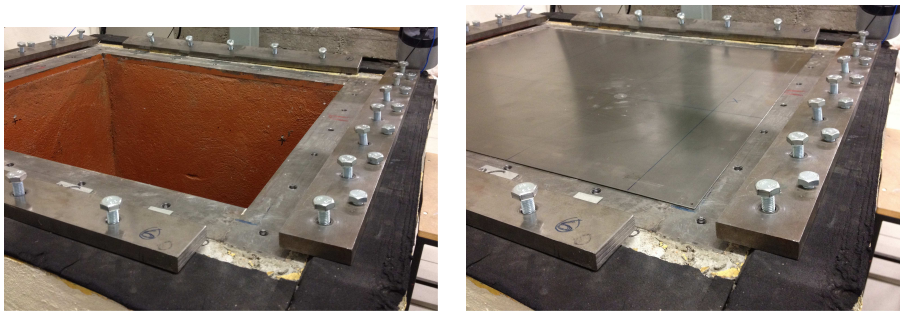

Figure 5.1: Coupling of the plate-cavity system

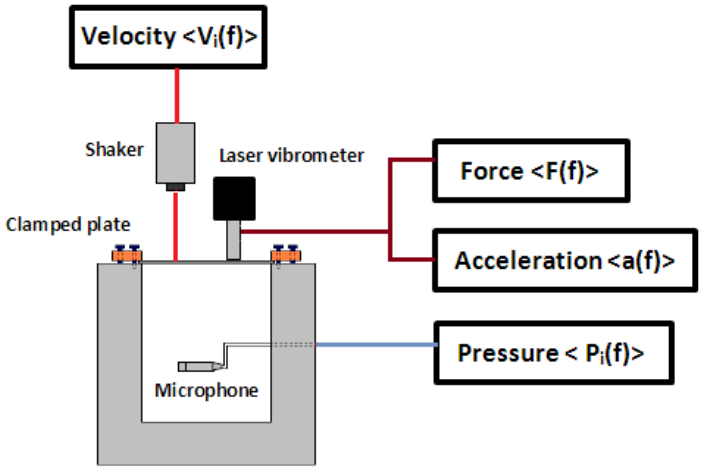

Figure 5.2: Schematic of the experimental setup

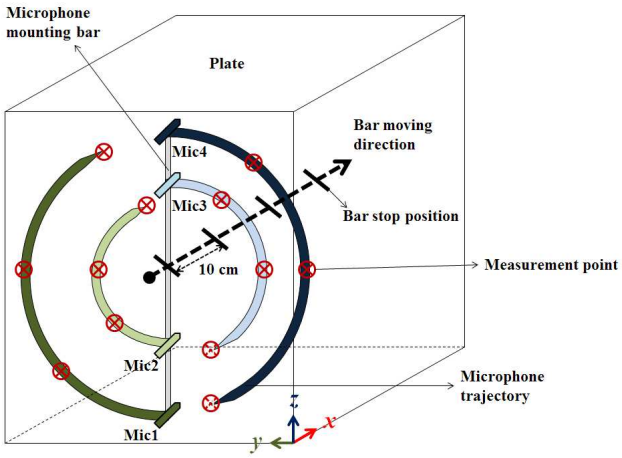

Figure 5.3: Microphone positions inside the cavity. 16 positions are made in yz plane by turning the mounting bar. The bar moves along x direction. Total 64 positions are taken.

To measure the plate velocity $\overline{V}(f)$, *Polytec* laser scanning vibrometer (OFV-3001 controller, OFV-056 scanning head and PSV-Z-040-H junction box) has been used. The shaker and the scanning device were mounted above the plate-cavity system as seen in Fig. 5.2. The cavity pressure $\overline{P}(f)$ was measured

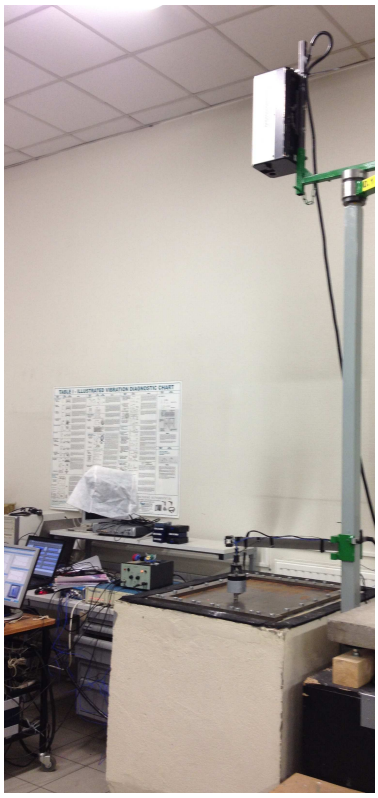

(a)

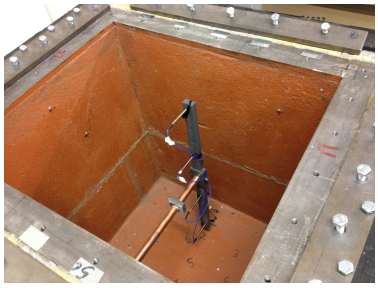

(b)

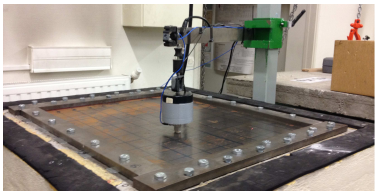

(c)

(d)

Figure 5.4: Experimental setup: (a) Plate-cavity system and the mounted vibrometer, (b) Mounted microphones inside the cavity, (c) Excitation, (d) Measurement equipment

with four 1/4 inch *PCB* 130D21 condenser microphones. The microphones were mounted in a bar that can be rotated inside the closed cavity by turning the connecting shaft. The cavity pressure measurement is illustrated in Fig. 5.3. Total 64 positions have been taken to determine the cavity energy. The input mobility and cavity pressure were treated with the multichannel FFT analyzer *OROS*. The experimental set up and the equipment are shown in Fig. 5.4. All measured quantities have been post-processed with *MATLAB*.

5.2 Measured quantities

5.2.1 Input mobility

To determine the injected power into the plate, driving force and plate response at a point of excitation are required (see Eq. 5.7). However, such quantities measured in situ can be often influenced by the mass of the impedance head and other attached elements. The seismic mass inside the device normally tempers a force measurement so that measured input mobility value can be different from the actual input mobility especially at higher frequencies [75]. This effect should be taken into account by the use of the correction factor. The impedance head used in the measurements seen in Fig. 5.5 weights 0.02 kg. The measured

Figure 5.5: PCB 288D01 Impedance head

input mobility $Y_m(\omega)$ is given by

$$Y_m(\omega) = \frac{\dot{x}(\omega)}{F(\omega)} = H_{\dot{x}F} = \frac{1}{j\omega}\frac{G_{\ddot{x}F(\omega)}}{G_{FF(\omega)}} = \frac{1}{j\omega}H_{\ddot{x}F}(\omega) \tag{5.1}$$

where $\ddot{x}(\omega)$, $F(\omega)$ denote the surface velocity at the point of excitation and the force respectively, $G_{FF(\omega)}$, $G_{\ddot{x}F(\omega)}$ are the force auto-spectrum and the cross-spectrum between the force and the acceleration respectively. The force measured by the impedance head F_M is modified from the actual force applied to the plate $F(t)$ by the inertia of the seismic mass $F_I = \ddot{x}\Delta M$ [21] as seen in Fig. 5.6.

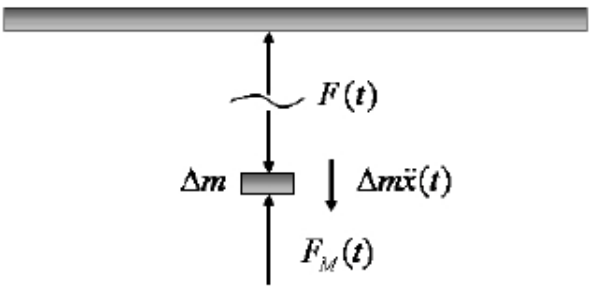

Figure 5.6: Mass effect of the impedance head on the force measurement [21]

The mobility of the impedance head can be measured by mounting the impedance head on a shaker

without loading the plate. This is given by

$$Y_I(\omega) = \frac{1}{j\omega H_I} \tag{5.2}$$

where $H_I = G_{FF(\omega)}/G_{\ddot{x}F(\omega)}$. The actual (corrected) input mobility $Y_{m'}$ of the plate can be then obtained by [21]

$$Y_{m'}(\omega) = \frac{\dot{x}(\omega)}{F_M(\omega) - F_I(\omega)} = \frac{\dot{x}(\omega)/F_M(\omega)}{1 - F_{I(\omega)}/F_M(\omega)} = \frac{Y_m(\omega)}{1 - Y_m(\omega)/Y_I(\omega)} \tag{5.3}$$

On the other hand, an analytical expression of $Y_I(\omega)$ can be given, knowing the mass Δm:

$$Y_I = \frac{1}{j\omega\Delta m} \tag{5.4}$$

Fig. 5.7 presents an imaginary part of the measured mobility of the impedance head in comparison with the analytical results obtained with Eq. 5.4. It can be seen that the actual seismic mass is close to 0.008 kg.

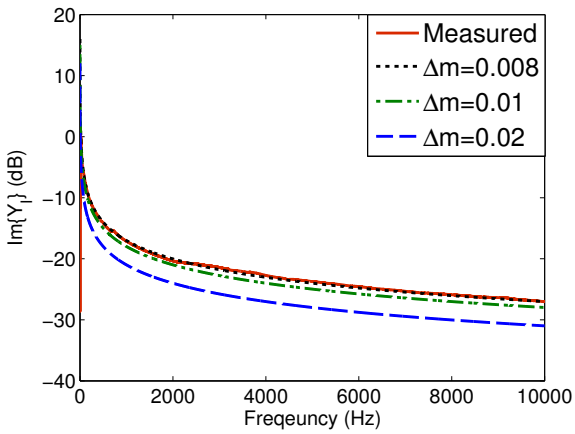

Figure 5.7: Mass dynamics of the impedance head. Comparison between measured and analytical results (Δm in kg)

In order to evaluate the correction factor, the corrected mobility can be compared to theoretical values. The input mobility $Y_m(\omega)$ of a lightly damped plate can be estimated by superposing the modal deformations at the point of excitation as follows

$$Y_m(\omega) = j\omega \sum_{i=1}^{+\infty} \frac{\Phi_i^2(x,y)}{m_i(\omega_i^2 + 2j\xi_i\omega_i\omega - \omega^2)} \tag{5.5}$$

where m_i, $\Phi_i^2(x,y)$, ξ_i are the i^{th} modal mass, modeshape at coordinate (x,y) and damping ratio respectively [36]. The real part of the input mobility only depends on the mass and modal density of the plate at high frequencies [36] so that the asymptotic value of an infinite plate can be obtained:

$$Y_m(\omega) \quad \overrightarrow{+\infty} \quad Re\{Y_m(\omega)\} = \frac{1}{4h^2}\sqrt{\frac{3(1-v^2)}{E\rho}} \tag{5.6}$$

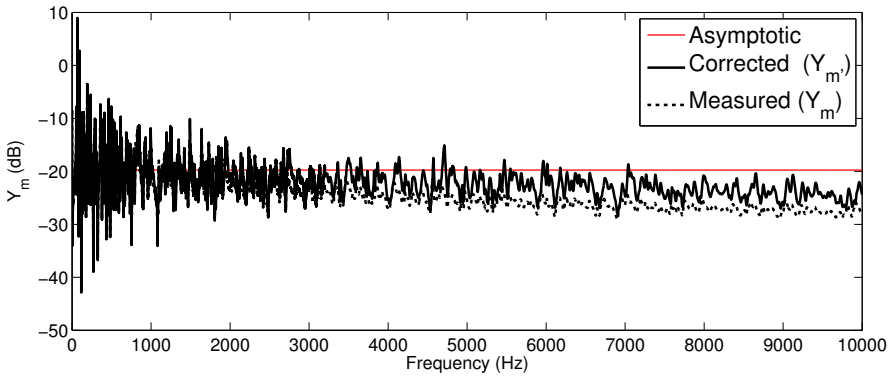

(a)

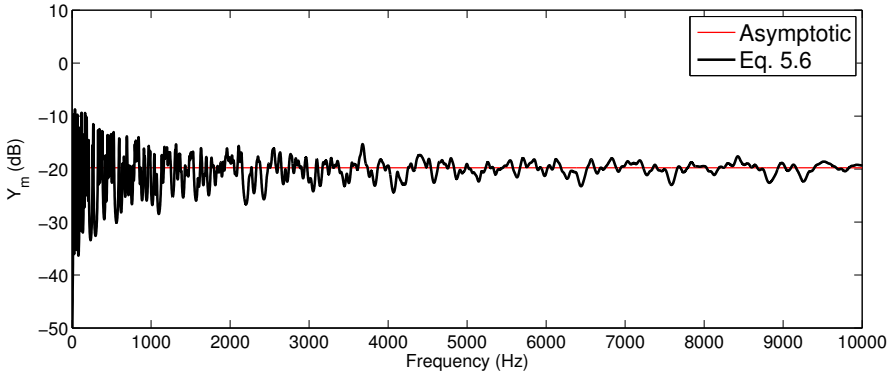

(b)

Figure 5.8: Input mobility of *Bare* plate in comparison with the asymptotic value: (a) Measured/corrected result, (b) Analytical result (Eq. 5.5)

The asymptotic value (Eq. 5.6) and analytical result (Eq. 5.5) can be compared to the corrected input mobility. Fig. 5.8 shows the results. The analytical result (Eq. 5.5) has been obtained with an arbitrary damping ($\xi_i = 0.005$) and the modeshape $\Phi_i^2(x, y)$ has been obtained at the plate coordinate $(x, y) = (0.2, 0.2)$ (m) in Section 2.2.4. The effect of the impedance head is clear at high frequencies. Although the corrected mobility is still lower than the asymptotic value, the correction factor has effectively increased the amplitude as much as 6 dB at high frequencies. Note that the injected powers and normalized subsystem responses for the test cases, presented in the following sections, take this correction factor into account.

5.2.2 Injected power

The injected power into the plate subsystem can be experimentally estimated from the force spectrum and the input mobility at the point of excitation. In a given frequency band, the time- and frequency-averaged power injected into a structural subsystem is given by [29]

$$P_{inj} = \int_{\omega_1}^{\omega_2} Re\{Y_m(\omega)\} S_f(\omega) d\omega \tag{5.7}$$

where S_F is the power spectral density of the force (N^2/Hz).

The injected power introduced in the SmEdA formulation can be estimated by considering the injected

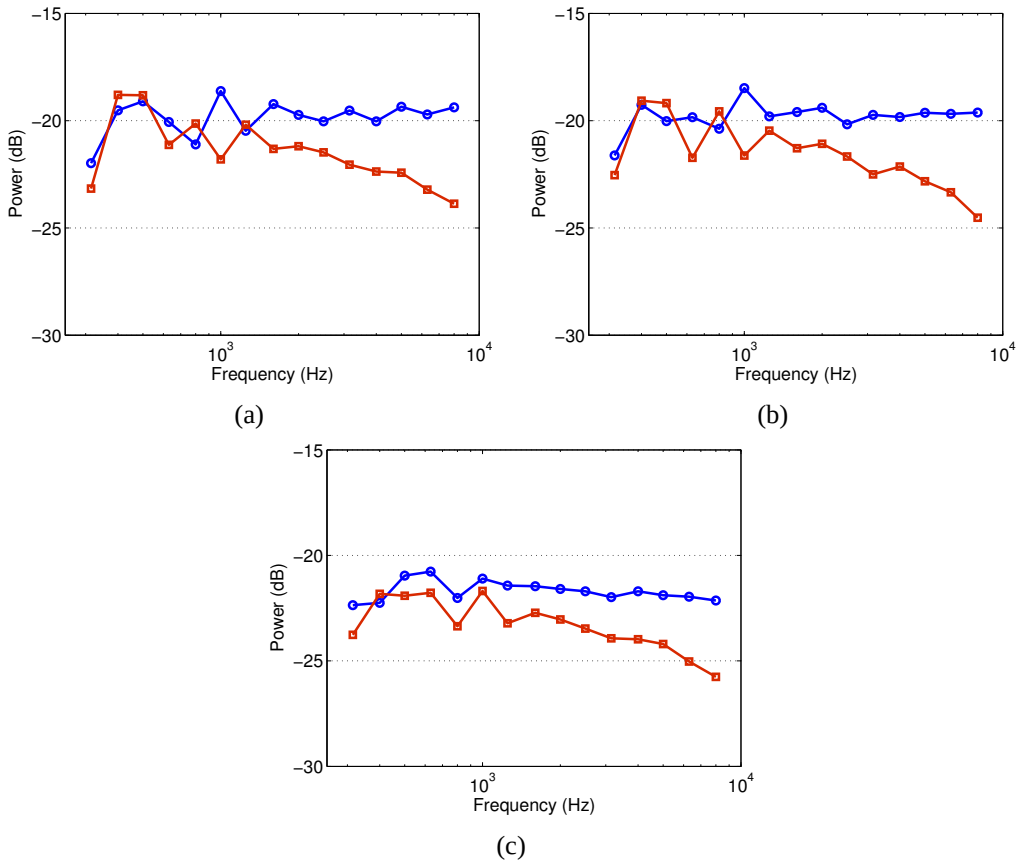

Figure 5.9: The injected power in 1/3 octave band (□: experimental, ◯: numerical): (a) *Bare*, (b) *Visc1*, (c) *Visc2*

power into the plate modes:

$$\Pi^1_{inj} = \sum_{p=1}^{N_1} \Pi^1_{p,inj} \tag{5.8}$$

where N_1 is the number of plate modes and $\Pi^1_{p,inj}$ is the modal injected power given in Eq. 2.26. The result in 1/3 octave band can be then compared to the experimental one estimated using Eq. 5.7. Fig. 5.9 shows the injected power of *Bare* and *Visc1&2* cases. Numerical results are comparable with experimental ones at low-mid frequencies (up to 2.5 kHz) for all three cases. Discrepancies are less than 3 dB in between. It can be seen that the numerical results have small differences between *Bare* and *Visc1*. On the other hand, the amplitude of *Visc2* is seen lower than *Bare* and *Visc1* by an average 2 dB. Since the force has been applied to all test cases at the same coordinate ($(x, y) = (0.2, 0.2)$) where the plate is not covered with the damping pad for *Visc1* case (see Fig. 4.4a), the results of *Bare* and *Visc1* are comparable. In contrary, for *Visc2* case, the force is located directly in front of the viscoelastic layer (see Fig. 4.4b). This can explain why the injected power is influenced in this case. At high frequencies, all three cases show large discrepancies as much as 4 dB. Some factors can be hypothesized to explain decreasing experimental values above 2.5 kHz.

The correction curve approach presented in Section 5.2.1 gives an acceptable mass compensation in the force measurement. Nonetheless, the corrected mobility seen in Fig. 5.8 is still below the theoretical asymptotic value by more than 1.5 dB above 3 kHz. Suppose that the actual thickness of the plate (used in

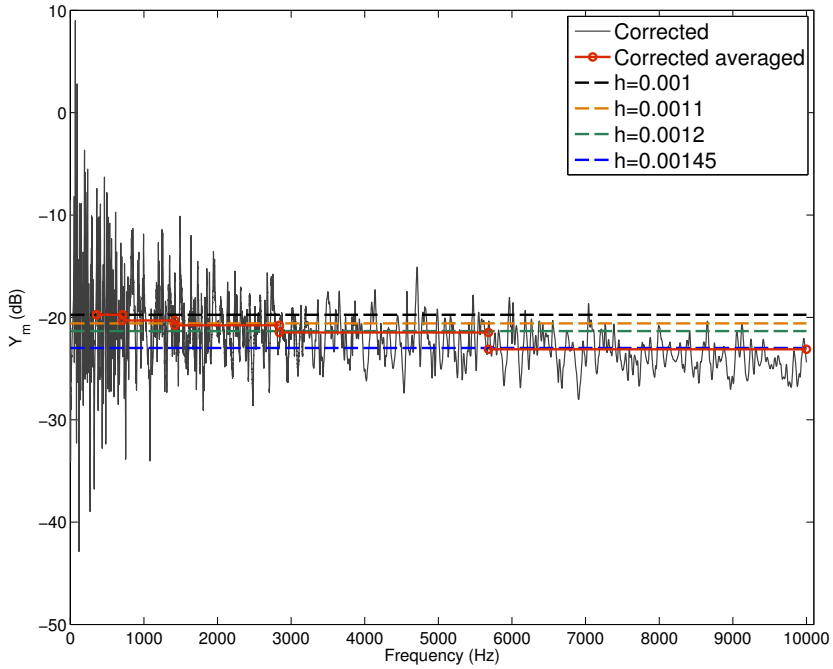

Figure 5.10: Asymptotic values of the input mobility (corrected) of *Bare* plate with respect to a plate thickness (Corrected values in solid ◯ are averaged in an octave band)

the measurements) is not homogeneous, a very small irregularity in the plate cross-section can, in fact, yield a large change in amplitude of the asymptotic input mobility value. Fig. 5.10 plots the corrected measured input mobility and its octave-band-averaged constant values in comparison with different asymptotic values depending on the thickness (h) of the plate. A thickness less than a half millimeter yields a discrepancy of approximately 3 dB in the asymptotic value to which the octave-band-averaged constant value of the corrected input mobility is comparable at high frequencies (centered at 4 kHz).

Another likely factor is an error in the measured input mobility induced by the impedance head. In fact, there exits a systematic error in the acceleration measurement caused by the mechanical assembly of an impedance head that can produce a substantially biased result at high frequencies [43]. Fig. 5.11 shows a typical design of an impedance head. Two piezoelectric crystals measure the force applied to a structure and its acceleration. Such design causes the input force across a finite mounting stiffness to produce relative motion between structure and the base of the acceleration crystal [15]. Therefore, an instrument of this type to capture an input force and a response at the same time affects any measurement regardless of the load impedance and inevitably produces a systematic error. This error is proportional to the force and the square of the frequency and inversely proportional to the stiffness of the force crystal and its attachment to the structure [15]. Some improved design can be made to increase the force crystal stiffness, nevertheless, it is only to minimize the error. The measured data at high frequencies are inevitably inaccurate [15]. As a result, an accurate measurement of the injected power at high frequencies is not an easy task.

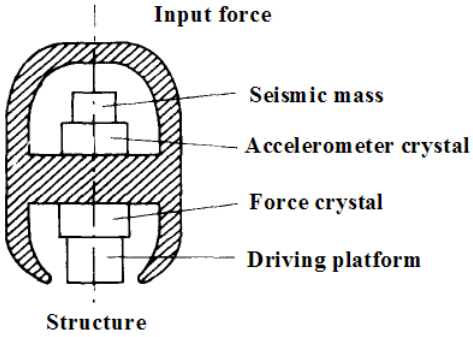

Figure 5.11: Schematic of a typical impedance head design [15]

5.2.3 Subsystem response

As the force was exerted on the plate, the plate velocity and the cavity pressure were simultaneously measured. A schematic of the measurement setup is illustrated in Fig. 5.2. The plate velocity $\overline{V}(f)$ was measured at more than 130 points.

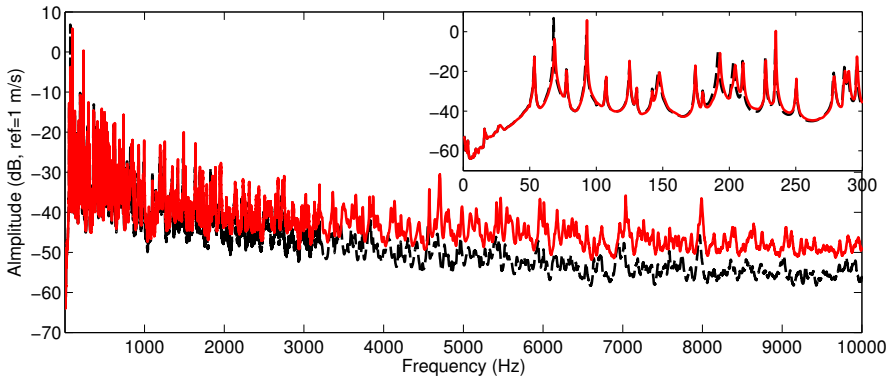

(a)

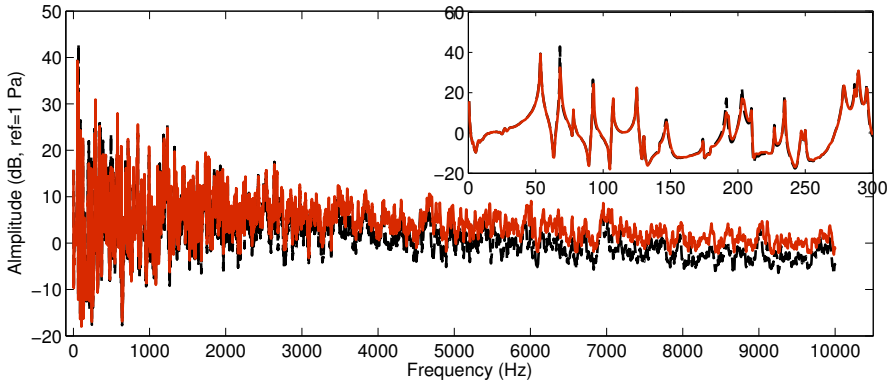

(b)

Figure 5.12: Corrected average squared subsystem responses of *Bare* case (Solid: corrected, Dashed: original): (a) Normalized plate velocity, (b) Normalized cavity pressure

The cavity pressure $\overline{P}(f)$ was measured at 64 points. All measured quantities were normalized with the

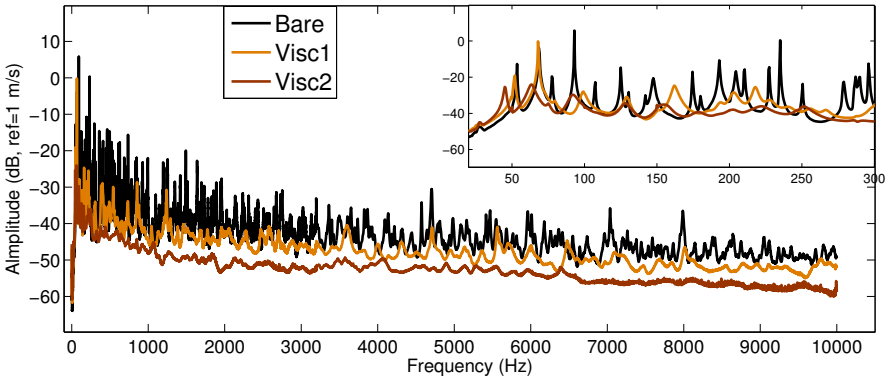

(a)

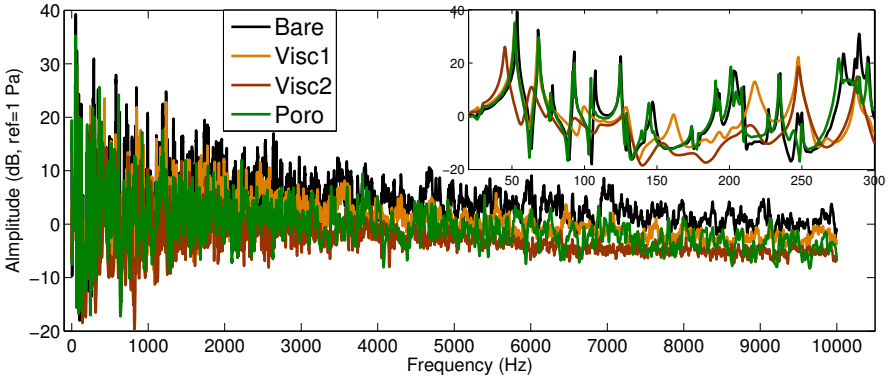

(b)

Figure 5.13: Average squared subsystem responses (corrected) of *Bare*, *Visc1* and *Visc2*: (a) Normalized plate velocity, (b) Normalized cavity pressure

input force. The average squared subsystem responses are given by

$$\overline{V}_i^2(f) = \frac{1}{N}\sum_{i=1}^{N}\left|\frac{V_i}{F}\right|^2,$$
$$\overline{P}_i^2(f) = \frac{1}{N}\sum_{i=1}^{N}\left|\frac{p_i}{F}\right|^2 \tag{5.9}$$

where F is the exerted force, and the subscript i indicates the number of measurement points. Fig. 5.12 compares the original subsystem responses to the corrected ones for *Bare* case. The effect of the impedance head is clear for both subsystem responses at high frequencies. Fig. 5.13 shows the subsystem responses (corrected) of each test case. With measured responses, subsystem energies can be determined in 1/3 octave band with Eq. 2.6.

5.2.4 Subsystem damping loss factor

The damping loss factors are experimentally determined for all subsystem configurations. The results for the treated subsystems (*Visc1*, *Visc2*, *Poro*) are used to evaluate the numerical predictions by the MSE and MSKE methods.

5.2.4.1 High-resolution modal analysis method

The plate of each test case (*Bare*, *Visc1*, *Visc2*) was driven by an impact hammer, and responses were measured with an accelerometer at several locations. The modal damping loss factors were then estimated from the impulse response using the high-resolution modal analysis method based on the ESPRIT algorithm [36]. Within the method, the impulse response $s(t)$ at a given point is considered to be a sum of decaying sinusoidal waves $x(t)$ and noise $\beta(t)$ as follows

$$s(t) = x(t) + \beta(t) = \left[\sum_{k=1}^{K} a_k e^{-\alpha_k t} e^{j(2j\pi f_k t + \varphi_k)}\right] + \beta(t) = \sum_{k=1}^{K} b_k z_k^t + \beta(t) \tag{5.10}$$

where K, a_k, α_k are the number of complex exponentials, modal amplitudes and phases at the point of

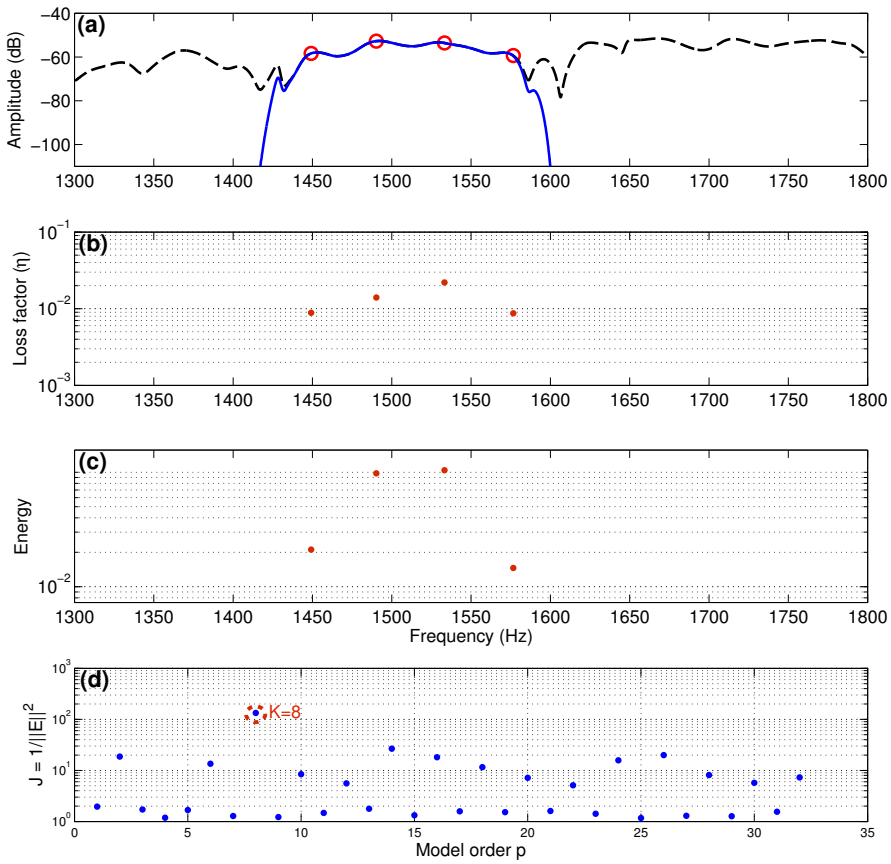

Figure 5.14: Bank-filtering analysis of an impulse response of *Visc1*: (a) Dashed: Fourier spectrum of the impulse response, Solid: amplitude response of a narrow band filter, ◯: resonant modes estimated by the high-resolution modal analysis, (b) Associated damping loss factor (the number of complex exponentials $K = 8$ is estimated with ESTER criterion), (c) Energy of each component, (d) ESTER criterion on the response signal. The number of the complex exponentials $K = 8$ (four modes) is detected.

interest respectively. f_k, α_k are the modal frequencies in Hz and the modal damping factors in s$^-1$ respectively. The modal damping factor is related to the modal decay time τ_k in second and the modal loss factor η_k as follows

$$\alpha_k = \frac{1}{\tau_k} = \frac{\eta_k \omega_k}{2}, \quad \eta_k = \frac{\delta f_{k,-3dB}}{f_k} = \frac{\alpha_k}{\pi f_k} \tag{5.11}$$

where $\omega_k, \delta f_{k,-3dB}$ are the modal angular frequency (in rad.s$^-1$) and the half-power modal bandwidth. The modal parameters (frequencies, damping factors and complex amplitudes) are estimated by projecting the impulse signal onto sinusoids and supplementary subspaces. The methods is based on the ESPRIT algorithm which takes account of the rotational invariance property of the signal subspace [36]. The dimensions of both subspaces must be chosen a priori and the quality of the estimation depends significantly on a proper choice for these parameters [36]. A choice of the modal subspace dimension is the number of complex exponentials (K) that is twice the number of real decaying sinusoids i.e. resonant modes. The ESTER (ESTimation ERror) technique [7] is used to determined the number. Fig. 5.14 shows a bank-filtering analysis of an impulse response on *Visc1* where resonant modes and associated modal damping loss factors are estimated by the high-resolution modal analysis in a narrow subband. The method can successfully separate twin modes of the system response (caused by the high modal overlap) and determine the modal damping, which makes itself applicable to mid-to-high frequency analysis.

5.2.4.2 Plate damping

Fig. 5.15 compares the modal damping loss factors of *Visc1* between numerical and experimental estima-

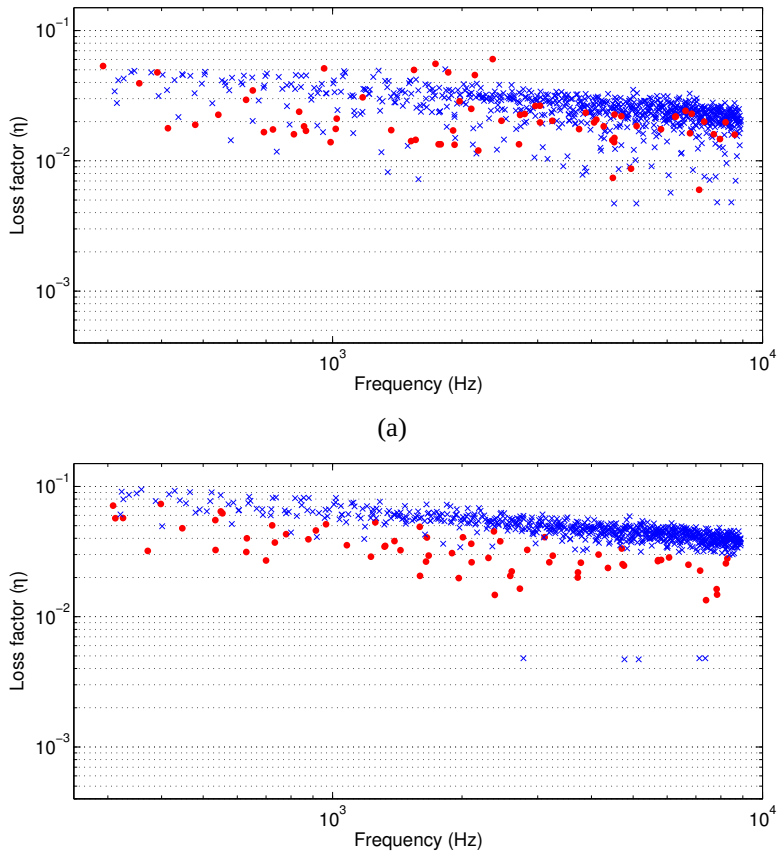

Figure 5.15: The modal damping loss factors of the treated plate (•: experimental, ×: MSE): (a) *Visc1*, (b) *Visc2*

tions. The MSE estimations are seen comparable with the experimental ones throughout the frequency

range. It is clearly seen in both results that the damping levels can vary greatly between resonant modes.

Fig. 5.15 compares the modal damping loss factors of *Visc2* between numerical and experimental estimations. The MSE computation results are approximately 30 % higher than those of *Visc2*. The numerical results have been clearly overestimated compared to the experimental ones, particularly at high frequencies. As it has been discussed in Section 3.3.2.2, however, the experimental technique based on the ESPRIT algorithm can easily detect weakly damped modes. It explains why the MSE method has given relatively higher values than the experimental results and the discrepencies increase with frequency.

5.2.4.3 Cavity damping

The cavity is driven by a loudspeaker with white noise at three positions (two corners and the center) at the cavity bottom, and the pressure decays are measured as the sound source is turned off. The cavity responses

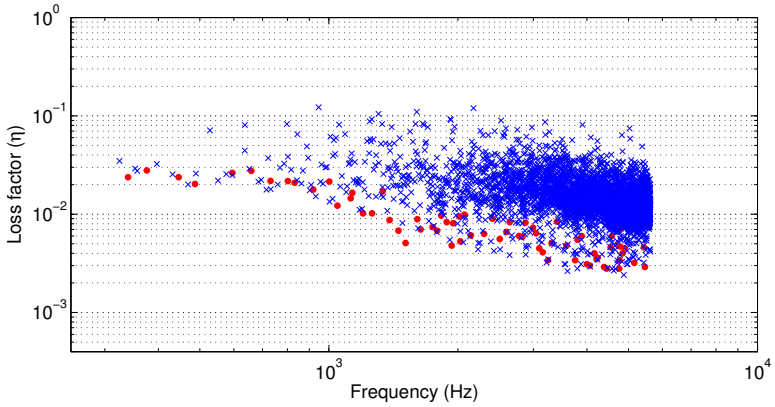

Figure 5.16: The modal damping loss factors of *Poro* (●: experimental, ×: MSKE)

are measured at several locations per source position with four rotating microphones inside the cavity. The top opening of the cavity is closed with a 5 cm concrete slab so that all surfaces are rigid. In that way, the energy transmission to the plate is eliminated. Note that the high-resolution modal analysis method of the ESPRIT algorithm are used to determine both *Empty-cavity* and *Poro* damping.

Fig. 5.16 compares the modal damping of *Poro* between numerical and experimental estimations. Below 500 Hz, two results are in good agreement. At mid-high frequencies, the MSKE result varies significantly between modes where low values agree well with the experimental ones. Such result comes from fact that the ESPRIT algorithm is not effective detecting heavily damp modes.

5.3 Subsystem response

5.3.1 Subsystem energy

Fig. 5.17 shows measured subsystem energies of all test cases (*Bare*, *Visc1*, *Visc2*, *Poro*) in 1/3 octave band. Note that *Poro* case is presented up to the 5 kHz band for comparison with its numerical counterpart. The

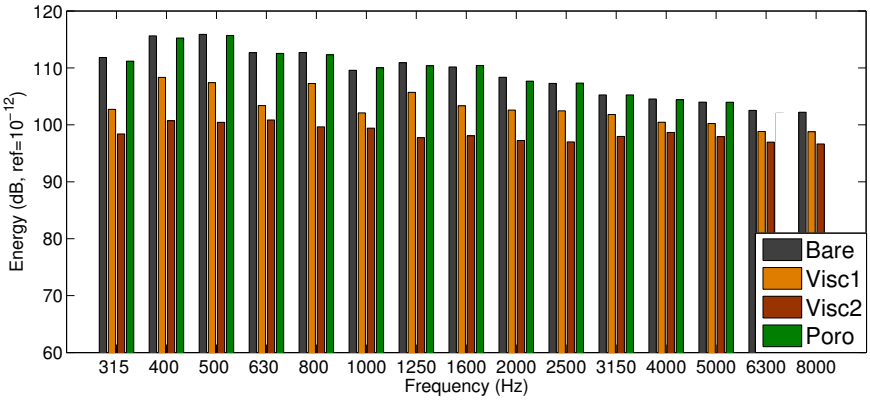

(a)

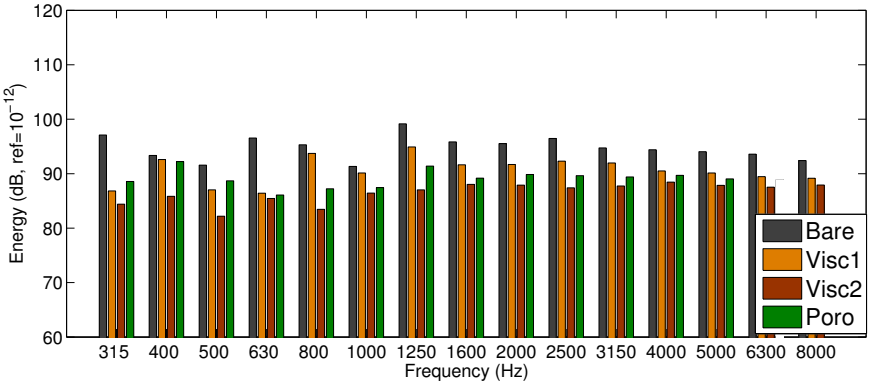

(b)

Figure 5.17: Experimentally obtained subsystem energy levels of all test cases in 1/3 octave band. (1) Plate subsystem energies, (2) Cavity subsystem energies

plate energies between the cases are seen to have the same tenancy as the numerical results (see Fig. 4.15) although the numerical calculations have been overestimated by an average 4 dB at all frequencies. The differences between plate energies of *Bare* and *Visc1&2* in the experimental results are rather small compared to those in numerical ones. Cavity energies have been also overestimated with discrepancies approximately 5 dB. It can be seen that more cavity energies of *Visc2* case are dissipated than those of *Poro* at all frequencies. This implicates that heavy damping on a structural subsystem alone can yield high energy dissipation simultaneously in both structural and acoustic subsystems under a structure-borne noise source.

5.3.2 Subsystem energy ratio

Fig. 5.18 shows a comparison between numerical and experimental energy ratios for *Bare* case. Note that SmEdA model is computed with the frequency-band averaged (global) damping loss factors of each subsystem (see Fig. 2.6) that are experimentally determined since no individual modal damping levels are available by numerical means. The results are comparable except at low frequencies. Fig. 5.19 plots the

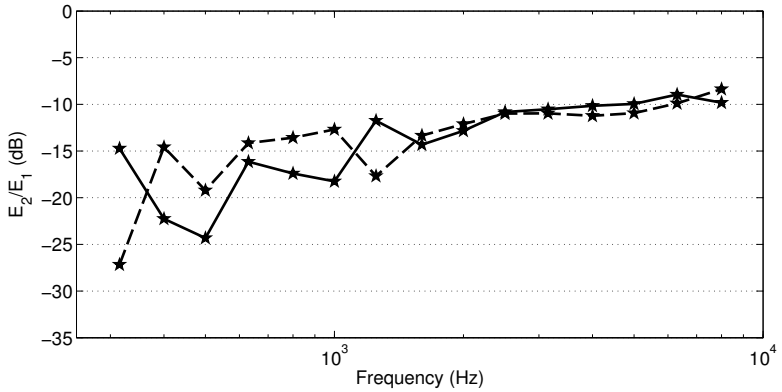

Figure 5.18: Subsystem energy ratio of *Bare* in 1/3 octave band (Solid: measured, Dashed: SmEdA prediction using the experimental frequency-band averaged damping loss factors given in Fig. 2.6)

subsystem energy ratio of each test case in 1/3 octave band. These experimental results display exactly the same tendency between test cases as the numerical predictions presented in Fig. 4.17: only the cavity

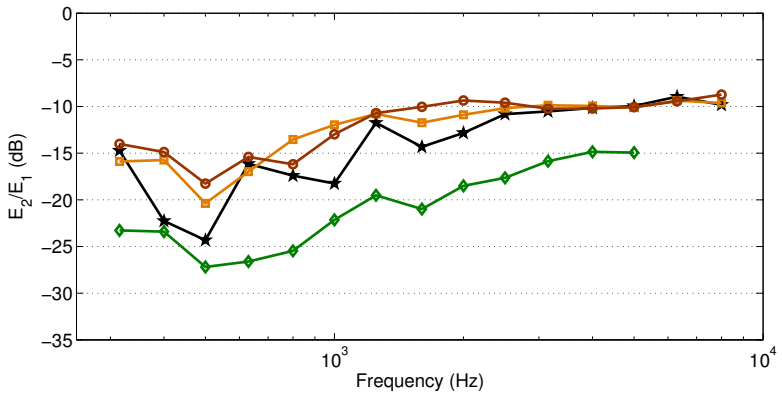

Figure 5.19: Measured subsystem energy ratio in 1/3 octave band ($\star$: *Bare*, $\square$: *Visc1*, $\bigcirc$: *Visc2* and $\diamondsuit$: *Poro*)

treatment case is considerably lower than the others. The SmEdA predictions have well captured such phenomenon.

Fig. 5.20 directly compares numerical and experimental energy ratios for *Poro* case. Two results are in good agreement above 1 kHz. However, the SmEdA result has been overestimated by an average 5 dB between 500 Hz and 1 kHz. A few factors can be postulated to explain this result. Cavity energies have been clearly overestimated compared to the experimental result. However, the MSKE result can not attribute to that outcome since the energy ratio is in fact comparable at other frequency bands. Then it can be said that the experimental cavity energies have been underestimated. The cavity pressure has been measured in a

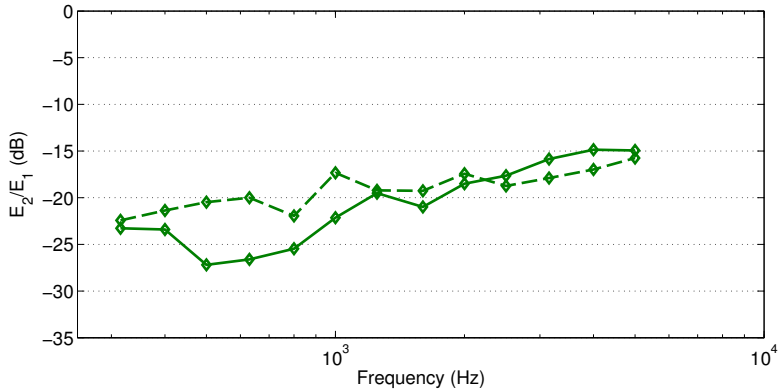

Figure 5.20: Subsystem energy ratio of *Poro* in 1/3 octave band (Solid: measured, Dashed: SmEdA prediction using the modal damping by MSKE

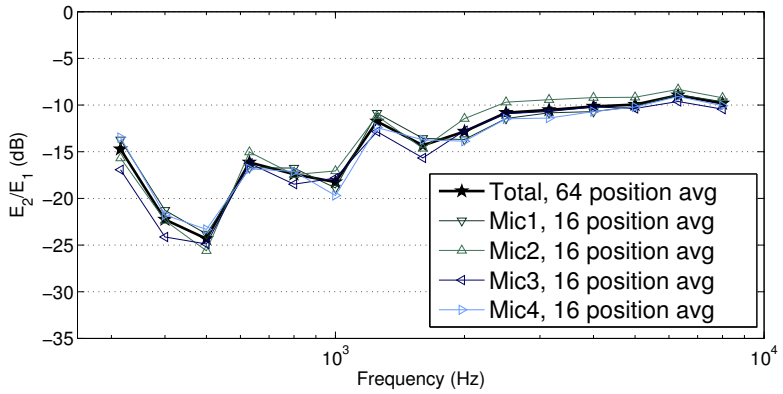

Figure 5.21: Subsystem energy ratio of *Bare* with respect to the measured cavity pressure at different microphone positions

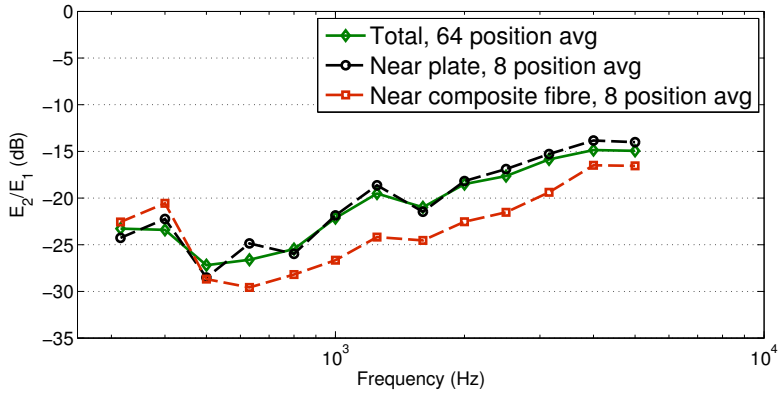

Figure 5.22: Subsystem energy ratio of *Poro* with respect to the measured cavity pressure near the plate and the composite fibre

systematical way that the microphone movement is limited to a certain extent. The microphones have not reached all the boundaries and the corners where the sound pressure is normally a few dB higher than the measured sound field. If certain cavity modes between 500 Hz and 1 kHz are amplified at those locations, the discrepancies can be well reduced.

In order to support such hypothesis, it can be observed how the experimental results (ratio) can be mod-

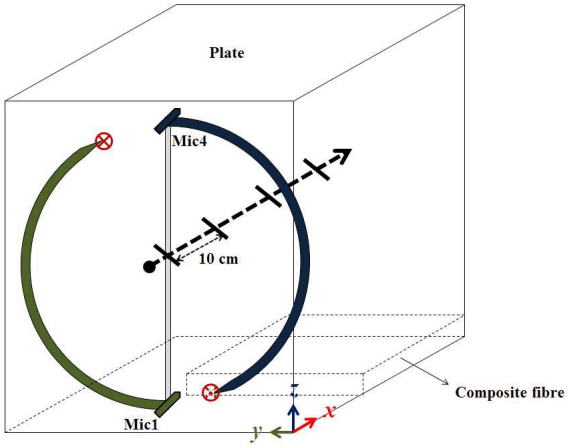

Figure 5.23: Microphone 1 and 4 to capture the pressure near the plate and the composite fibre. Total 8 positions are taken for each side.

ified depending on the pressure measured at different positions inside the cavity. Fig. 5.21 presents energy ratios of *Bare* case with respect to the microphone position. Each ratio curve has been calculated from the average pressure of each microphone (Mic1∼Mic4) over 16 positions (see Fig. 5.3). No substantial differences are seen between each microphone averages, which implicates relatively homogeneous pressure field within the reach of the microphones when an absorbing material is not present. Such results between microphone averages are consistent for all the other cases. However, *Poro* case can be considerably modified if the pressure near the composite fibre is mainly considered. Fig. 5.22 compares energy ratios for *Poro* case with respect to the measured cavity pressure in close proximity to the plate and to the composite fibre. It can be seen that the result obtained from the positions near the vibrating plate has small differences compared to the results from each microphone average of 16 positions. On the other hand, the curve computed from the pressure near the composite fibre is an average 3 dB lower than the rest, demonstrating a lower sound pressure near the composite fibre above 500 Hz.

5.3.3 Interval of the energy ratio

As subsystem modal damping levels inherently vary in a given frequency band, such variation can be exploited in reasonable manner for the numerical prediction to allow a range of the subsystem energy ratio. From the estimated modal damping loss factors by MSE and MSKE (given in Fig. 5.15a, 5.15b and 5.16) a lower bound of the predicted energy ratio can be determined by considering the highest values of both subsystems in each frequency band (a global value replaces η_p^1, η_q^2 in Eq. 2.21 for a given band). Subsequently, a higher bound can be set with the lowest damping loss factors.

Fig 5.24 presents measured ratios of *Visc1&2* cases in comparison with SmEdA computations that give an interval of the ratio determined with the described process. Measured ratios of *Visc* cases comply within the numerical intervals at mid-high frequencies. Since the plate damping has less influence on the energy ratio than the cavity damping, the sizable intervals in each case are largely due to the cavity damping variations. The cavity damping of *Poro* (see Fig. 5.16) has significant variation between modes: above 1 kHz, the difference can be more than 20 times between the lowest and the highest in a given frequency

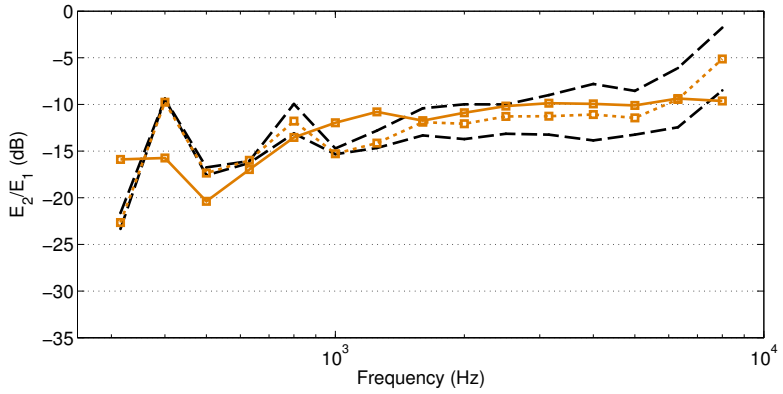

(a)

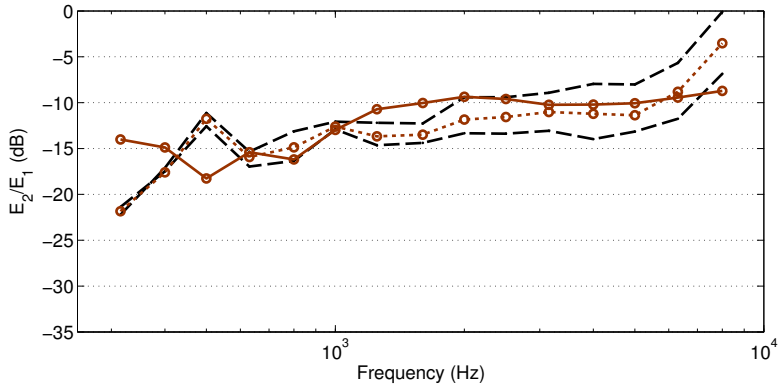

(b)

Figure 5.24: An interval of the subsystem energy ratio in 1/3 octave band (Dashed: upper/lower bounds set by SmEdA prediction using the highest/lowest numerical modal damping values in each frequency band, Solid: measured, Dotted: SmEdA prediction using all modal damping loss factors): (a) *Visc1*, (b) *Visc2*

band. Such difference in modal damping gives a substantially large interval of the energy ratio (an average 15 dB above 1 kHz), which in fact provides no practicality in terms of prediction.

5.4 Conclusion

The SmEdA calculation result of each test case has been compared with experimental results. Each test case has been exerted with a localized single point force that was measured with an impedance head. All measured quantities, normalized with the driving force, have been found tempered by the effect of an added mass of the impedance head. Such effect is non-negligible at high frequencies. To compensate this error, the mass correction factor has been taken into account. Nonetheless, the corrected input mobility is still below the theoretical asymptotic value at high frequencies, indicating a prevailing error in the measured acceleration. However, no further study has been conducted to assess this problem. Such error has lead to discrepancies in the injected power between experimental and numerical results. The prediction results are acceptable below 3 kHz. At high frequencies, on the other hand, experimental values decrease due to the prevailing error in the measured input mobility.

The damping loss factors of the treated subsystems have been compared to the experimental results. The

MSE method used to estimate the plate damping has produced comparable results. However, the damping levels by two viscoelastic damping pads are higher than experimental results. This comes from the fact that the experimental technique (ESPRIT algorithm) is more effective for estimating lightly damped modes.

The cavity damping by the MSKE method has shown comparable with the experimental result. The values vary substantially between modes, however, two results are in good agreement at low frequencies. At mid-high frequencies, low modal values are comparable with the experimental ones.

The predicted subsystem energies of the SmEdA test cases have been compared to the experimental results. More cavity energies have been dissipated by treating the plate than directly treating the cavity. This indicates that a structural damping treatment alone can achieve energy reduction in both subsystems if and only if a noise source is structureborne. On the other hand, it has been shown that no substantial differences in the subsystem energy ratios have occurred between damped and undamped cases if the damping is applied solely on a source subsystem. The energy ratio is sensitive to the damping of a receiving subsystem at mid-high frequencies, and such phenomenon has been well predicted by the SmEdA method.

The SmEdA method implementing the MSE and MSKE methods has demonstrated its feasibilities on the plate-cavity system when dissipative materials are introduced. The extended method allows to predict the subsystem energy transmission of a structure-fluid system in entirely numerical manner. Its prediction result has been shown strongly dependent on the subsystem damping loss factor. The method can, however, compensate such issue by considering the variation in the subsystem modal damping which in turn produces a prediction interval for the subsystem energy ratio.

CHAPTER 6

Conclusions and Perspectives

6.1 Conclusions

This Ph.D research has been carried out under the project CLIC (City Lightweight Innovative Cab). The project aims at reducing the body mass of the existing truck cabin yet maintaining the initial acoustic performance. A proper vibroacoustic modeling tool is required to study the dynamic behavior of the truck cabin structure. The focus has been brought to a structure-fluid problem with respect to the damping effect induced by trim components i.e. cabin trimmed body surfaces and cabin acoustic space. Since the analysis is required particularly on the mid-frequency domain, widely used FEM and SEA are not suited to the problem. Therefore, the Statistical modal Energy distribution Analysis (SmEdA) method has been adopted as a study platform. The method is not restricted to the subsystem modal energy equipartition of the classical SEA formulation so that it can be applied to a system with low modal overlap i.e. mid-frequencies. The main task is to extend the original formulation to take account of the influence of the damping effect introduced by dissipative materials. The work has been carried out on a simplified plate-cavity problem with respect to dissipative materials where the extended SmEdA method has been tested and verified. The dissipative materials, namely viscoelastic and porous, have been applied to the coupled system.

For the plate damped with the viscoelastic damping pad, the equivalent single layer approach has been implemented. The method has been demonstrated effective when determining the system response with the plate examples. Frequency dependent equivalent parameters can be effectively deduced with *MOVISAND* software that implements the equivalent single layer method. A subsequent task is to determine the internal damping of a damped plate. The MSE method has been implemented to estimate the modal damping loss factor. It has a major practical appeal for which the underlying real mode assumption leads to simplified system matrices hence reduced computational cost. The method has shown satisfactory results.

To model the composite fibre in the cavity, the equivalent fluid approach has been adopted. The method yields two major benefits: (1) it simplifies a model size of Biot hence substantially reduces computational cost, (2) without manufacturer's aid, all necessary model parameters are directly obtainable with simple impedance tube measurements. Since no solid frame motion is implicated, the model is only valid under airborne excitation. Therefore, a placement of the composite fibre has been restricted to one of the rigid cavity surfaces. Subsequently, the cavity damping loss factor has been determined with the MSKE method. The results have been comparable to the experimental data.

In order to evaluate the numerical damping estimation, the high-resolution modal analysis method has been used. Although the method can be applied for a wide frequency range where modal density is high, it still encounters typical difficulties that time-domain free-decay methods have: a difficulty fitting a straight line to the log of the decay-rate curve at high frequencies where modal overlap exceed unity, and the loss factors may vary with model parameters and measurement points [51]. Hence the method is best suited for lightly damped structures.

The SmEdA method has been demonstrated its capability in modeling a structure-fluid problem for the mid-frequency domain, a system of low modal overlap, which can be otherwise overestimated by the classical SEA formulation. The influence of the damping effect has been clearly presented by the SmEdA modal coupling factors. More subsystem resonant modes are coupled as the damping increases the subsystem modal overlap. In the damped cases, at least one mode of the subsystem has been coupled to all modes of the other subsystem, approaching near equipartition. However, this simply indicates that energies are well distributed among modes since the amount of energy exchanged by mode couples, in fact, has been clearly reduced by the dissipative materials.

It has been seen that dissipative materials used in this research have introduced a large amount of energy dissipation within the subsystems at all frequencies. Subsystem energy levels, determined both experimentally and numerically, have indicated that heavy damping on a structural subsystem alone can yield energy dissipation simultaneously in both structural and acoustical subsystems under a structural excitation. On the contrary, the subsystem energy ratio has no substantial change at mid-high frequencies when a source subsystem is treated. The ratio can be diminished by treating a receiving subsystem. Such phenomenon has been well predicted with the SmEdA method. A change of the energy ratio has been found sensitive to the damping of a receiving subsystem, however, the change has not been explicitly quantified with respect to the change of the damping. Under the influence of the dissipative materials, an accurate estimate of the subsystem internal damping has shown a direct impact on the SmEdA computation result. Such factor, however, can be compensated by facilitating the variation of the modal damping in order to determine an interval of the subsystem energy ratio.

Implemented equivalent modeling approaches together with the modal damping estimation methods (MSE and MSKE) can offer a simplified modeling process and a reduced computational cost. They have clear advantages suitable for a wide range of industrial applications, particularly large scale structures. Since industrial applications, automotive and aerospace in particular, are mostly complex coupled structures, one can strongly benefit from the use of the FEM to model uncoupled subsystems and from the detailed system descriptions given by the extended SmEdA method: modal damping, modal coupling and modal energy level. In addition, an ensemble description of the system i.e. the classical SEA terms can

be easily obtained from SmEdA parameters if necessary. Other strong advantage is that the method implicates relatively simple experimental verification since the injected power is a localized excitation whose frequency spectrum can be either broad- or narrow- band. This is highly beneficial compared to the PIM in the SEA formulation when it comes to measurements in situ since unexpected variables in environment often impedes multiple power injections. One can also facilitate the variation of the subsystem damping level in order to give an interval of the subsystem energy ratio in a frequency band analysis. Therefore, a coupled system under the influence of damping materials can be characterized in entirely numerical manner as long as the material properties are available.

6.2 Perspectives

This research has extended the SmEdA method to include the damping effect of the dissipative materials in a structure-fluid system. The extended method has been tested and verified on the plate-cavity problem. The next step of the project CLIC is to apply the proposed method to a full scale model of *Renault Midlum* truck cabin. The fully trimmed truck model consists of several viscoelastic damping pads and membranes of the composite fibre distributed over the floor and the rear surfaces. The post-doctoral research has been initiated to study the energy transmission between trimmed cabin surfaces and cabin air space. The extended SmEdA model implementing the MSE method has been applied to determine energies of the cabin floor trimmed with the viscoelastic damping pads and of the cabin air space. The impending task is to apply the MSKE method to determine energies of the cabin rear surface trimmed with the composite fibre. The SmEdA prediction of the fully trimmed truck will be then experimentally evaluated. The injected power is stationary and impulse sources that are mainly applied from the bottom of the cabin.

Experimentally estimated subsystem damping is an absolute reference to evaluate the numerical prediction. Since the high-resolution modal analysis method used in this research has shown some limitations, other experimental method can be considered. The power input (injection) method [12] based on structural energy losses has no theoretical limitation on broad frequency applications and it has been proven to have advantages over commonly used experimental methods such as frequency-domain half-power bandwidth method or time-domain decay curve fitting method [51]. Recent studies have applied the method to heavily damped structures and to an extended frequency range [19] [16] [57] [72].

A partial treatment (patch arrangement) of the damping application has been a predominant format to curb noise problems in highly cost-driven industrial applications. In addition, mass lightening is extremely important as of the main objective in this project. Therefore, the current SmEdA model can be extended to explicitly accommodate such factor: a change of the SmEdA modal coupling parameters and subsystem energies may be quantified depending on a surface area, shape, total mass and location of the dissipative treatment applied to the base structure. A parametric study can be carried out to optimize a patch arrangement in order to maximize the system modal damping while minimizing a total weight.

For the modeling technique of porous materials proposed in this research, a placement of the material has been restricted to a rigid cavity surface under the equivalent fluid assumption. Many practical engineering structures, in fact, consist of multiple layers of damping and/or absorbing materials directly fixed to vibrating surfaces. A further research can be carried out to develop a modeling technique that allows porous

materials directly attached to a vibrating surface. Simplicity and computational cost must be considered which can separate itself from existing models such as the mixed formulation [5] [4] and equivalent limp model [11] [44] [27]. Subsequently, its model parameters should be easily integrated into a FE model of an uncoupled fluid subsystem for the SmEdA formulation.

Bibliography

[1] B. Alaami. Waves in prismatic guides of arbitrary cross section. *Journal of Applied Mechanics*, pages 1067–1071, 1973.

[2] N. Alam and N.T. Asnani. Vibration and damping analysis of multilayered rectangular plates with constrained viscoelastic layers. *Journal of Sound and Vibration*, 97:597–614, 1984.

[3] J. F. Allard. *Propagation of Sound in Porous Media: Modelling Sound Absorbing Materials*. Elsevier Applied Science, London, 1993.

[4] N. Atalla, M. A. Hamdi, and R. Panneton. Enhanced weak integral formulation for the mixed (u, p) poroelastic equations. *Journal of Sound and Vibration*, 109(6):3065, 2001.

[5] N. Atalla, P. Raymond, and D. Patricia. A mixed displacement-pressure formulation for poroelastic materials. *Journal of Sound and Vibration*, 104(3):1444, 1998.

[6] K. Attenborough. Acoustical characteristics of rigid fibrous absorbents and granular materials. *Journal of the Acoustical Society of America*, 73(3):785–799, 1983.

[7] R. Badeau, B. David, and R. Richard. A new perturbation analysis for signal enumeration in rotational invariance techniques. *IEEE Transactions on Signal Processing*, 54(2):450–458, 2006.

[8] K. J. Bathe and E. L. Wilson. *Numerical methods in finite element analysis*. Prentice-Hall, 1976.

[9] A. Baz and J. Ro. Optimum design and control of active constrained layer damping. *Journal of Vibration and Acoustics*, 117:135–144, 1995.

[10] B.X. Bécot and F. Sgard. On the use of poroelastic materials for the control of the sound radiated by a cavity backed plate. *Journal of the Acoustical Society of America*, 120(4), 2006.

[11] L. L. Beranek and L. Istvan. *Noise and vibration control engineering: principles and applications*. John Wiley and Sons Inc, New York, USA, 1992.

[12] D. A. Bies and S Hamid. In situ determination of loss and coupling loss factors by the power injection method. *Journal of Sound and Vibration*, 70:187–204, 1980.

[13] M. A. Biot. Theory of deformation of a porous viscoelastic anisotropic solid. *Journal of Applied Physics*, 27, 1956.

[14] M. A. Biot. Generalized theory of acoustic propagation in porous dissipative media. *Journal of the Acoustical Society of America*, 34, 1962.

[15] J. M.W. Brownjohn, G.H. Steele, P. Cawley, and R.D. Adams. Errors in mechanical impedance data obtained with impedance heads. *Journal of Sound and Vibration*, 73(3):461–468, 1980.

[16] Bloss B. C. and M.D. Rao. Estimation of frequency-averaged loss factors by the power injection and the impulse response decay methods. *Journal of the Acoustical Society of America*, 117(5):240–249, 2005.

[17] C. J. Cameron, P. Wennhage, and P. Goransson. Prediction of nvh behavior of trimmed body components in the frequency range 100-500 hz. *Applied Acoustics*, 71:708–721, 2010.

[18] B. Campolina, N. Dauchez, N. Atalla, and Doutres. O. Effect of porous material compression on the sound transmission of a covered single leaf panel. *Applied Acoustics*, 73:791–797, 2012.

[19] M. Carfagni and M Pierini. Determining the loss factor by the power input method (pim), part 2: Experimental investigation with impact hammer excitation. *Journal of Vibration and Acoustics*, 121:422–428, 1999.

[20] A. Castel, A. Loredo, A. El Hafidi, and B. Martin. Complex power distribution analysis in plates covered with passive constrained layer damping patches. *Journal of Sound and Vibration*, 331:2485–2498, 2012.

[21] K. A. Castillo. *Simulation numerique d'un reverberateur a plaque*. PhD thesis, L'Ecole Polytechnique, 2009.

[22] A. Charpentier, T. Miyahara, Y. Hamada, and I. Ohsugi. Using the hybrid fe-sea method to predict warning system in a trimmed full vechicle. In *Proceeding of Journal of Society of Automotive Engineers of Japan*, Yokohama, Japan, 2009.

[23] A. Charpentier, S. Prasanth, and F. Kazuki. Efficient model of structure-borne noise in a fully trimmed vechicle from 200hz to 1khz. In *Proceeding of InterNoise*, Shanghai, China, October 2008.

[24] S. M. Chen, D. F. Wang, and J. M. Zan. Interior noise prediction of the automobile based on hybrid fe-sea method. *Mathematical Problems in Engineering*, 2011, 2011.

[25] C. Cicirello and R. S. Langley. The vibro-acoustic analysis of built-up systems using a hybrid method with parametric and non-parametric uncertainties. *Journal of Sound and Vibration*, 332(9):2165–2178, 2012.

[26] A. Craggs. Coupling of finite element acoustic absorption models. *Journal of Sound and Vibration*, 66(4):605–613, 1979.

[27] O. Dazel, B. Brouard, C. Depollier, and S. Griffiths. An alternative biots displacement formulation for porous materials. *Journal of the Acoustical Society of America*, (121):3509–3516, 2007.

[28] O. Dazel, B. Brouard, W. Lauriks, P. Goransson, and N. Dauchez. *Master 2 Acoustique et Mecanique de Universite du Maine*. Universite du Maine, France, 2010.

[29] K. De Langhe and P. Sas. Statistical analysis of the power injection method. *Journal of the Acoustical Society of America*, 100(1), 1996.

[30] M.E. Delany and E.N. Bazley. Acoustical properties of fibrous absorbent materials. *Applied Acoustics*, 3:105–116, 1970.

[31] W. Desmet. *A wave based prediction technique for coupled vibro-acoustic analysis*. PhD thesis, KULeuven, division PMA, 1998.

[32] W. Desmet., B. Hal, and P. Sas. A computationally efficient prediction technique for the steady-state dynamic analysis of coupled vibro-acoustic systems. *Advances in Engineering Software*, 33:527–540, 2002.

[33] W. Desmet, B. Pluymers, and O. Atak. *"MID-FREQUENCY" CAE Methodologies for Mid-Frequency Analysis in Vibration and Acoustics*. Katholieke Universiteit Leuven - Faculty of Engineering, Heverlee, Belgium, 2012.

[34] O. Doutres, N. Dauchez, J.M. Génevaux, and O Dazel. Validity of the limp model for porous materials: A criterion based on the biot theory. *Journal of the Acoustical Society of America*, 122(4), 2007.

[35] A. Duval, J. Baratier, and C. Morgenstern. Trim fem simulation of a dash and floor insulator cut out modules with structureborne and airborne excitations. *Journal of the Acoustical Society of America*, 123:3532, 2008.

[36] K. Ege, X. Boutillon, and B. David. High-resolution modal analysis. *Journal of Sound and Vibration*, 325:852–869, 2009.

[37] F. Fahy and P. Gardonio. *Sound and Structural Vibration, Radiation, Transmission and Response*. Elsevier, Oxford, UK, 2007.

[38] F. Fahy and J. Walker. *Advanced applications in Acoustics, Noise & Vibration*. Spon Press, NY, USA, 2004.

[39] J. D. Ferry. *Viscoelastic Properties of Polymers*. Wiley, New Yotk, NY, USA, 1980.

[40] T. H. Fronk, K.C. Womak, and K.D. Ellis. Finite element modeling of damping in constrained layer composite structures induced by inplane loads using adina. *Computers & Strucrures*, 56(2/3):357–363, 1995.

[41] J.-L. Guyader and C. Cacciolati. Viscoelastic properties of single layer plate material equivalent to multi-layer composite plate. In *Proceedings of Inter-Noise*, Istanbul, Turkey, August 2007.

[42] J.-L. Guyader and C. Lesueur. Acoustic transmission through orthotropic multilayered plates, part i: plate vibration modes. *Journal of Sound and Vibration*, 58(1):51–58, 1978.

[43] B. Hakansson and P. Carlsson. Biased errors in mechanical impedance data obtained with impedance heads. *Journal of Sound and Vibration*, 113(1):173–183, 1987.

[44] K. U. Ingard. *Notes on Sound Absorption Technology*. Noise Control Foundation, New York, 1994.

[45] E. Ioannides and P. Grootenhuis. A finite element analysis of the harmonic response of damped three-layer plates. *Journal of Sound and Vibration*, 67:203–218, 1979.

[46] C.D. Johnson and D.A. Kienholz. Finite element prediction of damping in structures with constrained viscoelastic layers. *The American Institute of Aeronautics and Astronautics*, 20(9):1284–1290, 1982.

[47] S. Jonckheere, D. Vandepitte, and W. Desmet. A hybrid finite element - wave based method for coupled acoustic-poroelastic applications. In *Proceeding of Symposium on the Acoustics of Poro-Elastic Materials*, Ferrara, Italy, December 2011.

[48] D. Karnopp. Coupled vibratory-system analysis, using the dual formulation. *Journal of the Acoustical Society of America*, 40:380–384, 1966.

[49] E. M. Kerwin. Damping of flexural waves by a constrained viscoelastic layer. *Journal of the Acoustical Society of America*, 31(7), 1959.

[50] H. Koruk and K.Y. Sanliturk. Assesment of the complex eigenvalue and the modal strain energy methods for damping predictions. In *Proceedings of the 18th International Congress on Sound and Vibration*, Rio de Janeiro, Brazil, July 2011.

[51] W. Liu. *Experimental and analytical estimation of damping in beams and plates with damping treatments*. PhD thesis, University of Kansas, Kansas, KS, USA, 2008.

[52] K.H. Lo, R.M. Christensen, and E.M. Wu. A high-order theory of plate deformation-part 1: homogeneous plates. *Journal of Applied Mechanics*, 44(4):663–668, 1977.

[53] R. H. Lyon and R. G. Dejong. *Theory and Application of Statistical Energy Analysis*. Butterworth-Heineman, 1995.

[54] B.A. Ma and J.-F. He. A finite element analysis of viscoelastically damped sandwich plates. *Journal of Sound and Vibration*, 1523:107–123, 1992.

[55] P.R. Mantena, R.F. Gibson, and S.J. Hwang. Optimal constrained viscoelastic tape lengths for maximizing damping in laminated composites. *Journal of the Acoustical Society of America*, 29:1678–1685, 1991.

[56] J. L. Marcelin, S. Shakhesi, and F. Pourroy. Optimal constrained layer damping of beams: experimental numerical studies. *Shock and Vibration*, 2:445–4 50, 1995.

[57] B. Maxime. *Acquiring Statistical Energy Analysis Damping Loss Factor for Complex Structures with Low to High Damping Characteristics*. PhD thesis, University of Sherbrooke, Quebec, Canada, 2007.

[58] L. Maxit. *Extension et reformulation du modele SEA par la prise en compte de la repartition des energies modales*. PhD thesis, Institut National des Sciences Appliquees de Lyon, Lyon, France, 2000.

[59] L. Maxit, K. Ege, N. Totaro, and J.-L. Guyader. Non resonant transmission modelling with statistical modal energy distribution analysis. *Journal of Sound and Vibration*, 333:499–519, 2014.

[60] L. Maxit and J.-L. Guyader. Estimation of sea coupling loss factors using a dual modal formulation and fem modal infromation, part i: Theory. *Journal of Sound and Vibration*, 239(5):907–930, 2001.

[61] L. Maxit and J.-L. Guyader. Estimation of sea coupling loss factors using a dual modal formulation and fem modal infromation, part ii: Numerical application. *Journal of Sound and Vibration*, 239(5):931–948, 2001.

[62] L. Maxit and J.-L. Guyader. Extension of sea model to subsystems with non-uniform modal energy distribution. *Journal of Sound and Vibration*, 265(2):337–358, 2003.

[63] R. J. McQuillin and E. M. Kerwin. Damping of flexural waves by patches of treatment. *Journal of the Acoustical Society of America*, 1961.

[64] D. J. Mead and S. Markus. The forced vibration of a three-layer, damped sandwich beam with arbitrary boundary conditions. *Journal of Sound and Vibration*, 10(2):163–175, 1968.

[65] M. Melon. *Caracterisation de Materiaux Poreux par Ultrasons de Basses Frequences (20-500 kHz)*. PhD thesis, Univercity Du Maine, Le Mans, France, 1996.

[66] Y. Miki. Acoustical properties of porous materials - generalizations of empirical models. *Journal of the Acoustical Society of America*, 11(1):25–28, 1990.

[67] D Rao. Mohan. Recent applications of viscoelastic damping for noise control in automobiles and commercial airplanes. *Journal of Sound and Vibration*, 262(3):457–474, 2003.

[68] C. T. Musser, J. E. Manning, and G. C. Peng. Predicting vehicle interior sound with statistical energy analysis. *Sound & Vibration*, 46(12):8, 2012.

[69] R. Panneton and N. Atalla. An efficient scheme for solving the three dimensional poroelasticity problem in acoustics. *Journal Acoustic Society of America*, (101):3287–3298, 1998.

[70] R. Panneton and X. Olny. Analytical solutions for the characterization of the tortuosity and viscous characteristic length of porous media. *Journal of the Acoustical Society of America*, 110(2683), 2002.

[71] G. Parthasarathy, C.V.R. Reddy, and N. Ganesa. Partial coverage of rectangular plates by unconstrained layer damping treatments. *Journal of Sound and Vibration*, 102(2):203–216, 1985.

[72] J. Plunt. Predictability of mid- and high frequency dynamic properties of industrial product. In *Proceedings of 8th International Conference on Recent Advances in Structural Dynamics*, Southampton, UK, July 2003.

[73] B. Pluymers, D. Vandepitte, and W. Desmet. Trefftz-based methods for time-harmonic acoustics. *Archives of Computational Methods in Engineering*, 14(4):343–381, 2007.

[74] J.N. Reddy. A simple higher-order theory for laminated composite plates. *Journal of Applied Mechanics*, 51(4):745–752, 1984.

[75] K. Renji. Experimental modal densities of honeycomb sandwich panels at high frequencies. *Journal of the Acoustical Society of America*, 237(1):67–79, 2000.

[76] Y.V.K. Sadasiva Rao and B.C. Nakra. Vibrations of unsymmetrical sandwich beams and plates with viscoelastic cores. *Journal of Sound and Vibration*, 34:309–326, 1974.

[77] T. D. Scharton and R. H. Lyon. Power flow and energy sharing in random vibration. *Journal of the Acoustical Society of America*, 43:1332–1343, 1968.

[78] P.J. Shorter and R.S. Langley. Vibro-acoustic analysis of complex systems. *Journal of Sound and Vibration*, 288(3):669–699, 2005.

[79] R. Stelzer, L. Maxit, J.-L. Guyader, and N. Totaro. Non resonant contribution and energy distributions using statistical modal energy distribution analysis (smeda). In *Proceedings of International Conference on Noise and Vibration Engineering*, Leuven, Belgium, 2010.

[80] N. Totaro, C. Dodard, and J.-L. Guyader. Sea coupling loss factors of complex vibro-acoustic systems. In *Journal of Vibration and Acoustics*, volume 131, 2009.

[81] N. Totaro and J.-L. Guyader. Extension of the statistical modal energy distribution analysis for estimating energy density in coupled subsystems. *Journal of Sound and Vibration*, 331:3114–3129, 2012.

[82] N. Totaro, L. Maxit, and J.-L. Guyader. Post-traitement et analyse energetiques de resultats elments finis. In *Proceeding of 10eme Congres Français d'Acoustique*, Lyon, France, 2010.

[83] J. Tran-Van, X. Olny, F.C. Sgard, and Y. Gervais. Global inverse methods for determine the acoustical parameters of anisotropicporous materials. In *Proceedings of 17th International Congress on Acoustics*, 2001.

[84] E. Ungar and E. M. Kerwin. Loss factors of viscoelastic systems in term of energy concepts. *Journal of the Acoustical Society of America*, 34(7):954–957, 1962.

[85] H. Utsuno, T. Tanaka, and T. Fujikawa. Transfer function method for measuring characteristic impedance and propagation constant of porous materials. *Journal of the Acoustical Society of America*, 86(2), 1989.

[86] I. Vaz, K. Washburn, and L. DeVries. Improvement of an sea mode of cab interior sound levels through use of a hybrid fe-sea method. In *Proceedings of SAE 2011 Noise and Vibration Conference and Exhibition*, Grand Rapids, MI, USA, 2011.

[87] M. L. Williams, R.F. Landel, and J.D. Ferry. The temperature dependence of relaxation mechanisms in amorphous polymers and other glass-forming liquids. *Journal of the American Chemical Society*, 77(14):3701–3707, 1955.

[88] T. Yamaguchi, Y. Kurosawa, and H. Enomoto. Damped vibration analysis using finite element method with approximated modal damping for automotive double walls with a porous material. *Journal of Sound and Vibration*, 325:436–450, 2009.

[89] M. J. Yan and E. H. Dowell. Governing equations for vibrating constrained-layer damping sandwich plates and beams. *Journal of Applied Mechanics*, 39:1041–1046, 1972.

[90] S.L. Yaniv. Impedance tube measurement of the propagation constant and characteristic impedance of porous materials. *Journal of the Acoustical Society of America*, 54:1138–1142, 1973.

[91] F. F. Yap and J. Woodhouse. Investigation of damping effect on statistical energy analysis of coupled structures. *Journal of Sound and Vibration*, 197(3):351–371, 1996.

[92] A. Zambrano, J.A. Inaudi, and J.M. Kelly. Modal coupling and accuracy of modal strain energy method. *Journal of Engineering Mechanics*, 122(7):603–612, 1996.

[93] H. Zheng, G.S.H. Pau, and Y.Y. Wang. A comparative study on optimization of constrained layer damping treatment for structural vibration control. *Thin-Walled Structures*, 44:886–896, 2006.

[94] C. Zwikker and C. W. Kosten. *Sound Absorbing Materials*. Elsevier Press, Amsterdam, 1949.